STUDY OF CATHODE INTERFACIAL LAYER FOR HIGHLY EFFICIENT INVERTED ORGANIC SOLAR CELLS

LIN ZHENHUA

NATIONAL UNIVERSITY OF SINGAPORE

2013

Declaration

I hereby declare that the thesis is my original work and it has been written by me in its entirely.

I have duly acknowledged all the sources of information which have been used in the thesis.

This thesis has also not been submitted for any degree in any university previously.

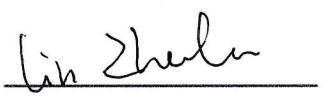

Lin Zhenhua

28 July 2013

Acknowledgements

This dissertation would not have been possible without the support and encouragement from so many people in so many ways. I would like to express my heartfelt gratitude and appreciation to the following people for their invaluable guidance and assistance.

My deepest gratitude goes first and foremost to Prof. Zhu Chunxiang, my supervisor, for his constant encouragement and guidance in my both research work and life. I will always remember the way he trained me to find out a problem, understand it and solve it in the research, and I will never forget the wisdom and experience of life he taught me. I am very fortunate and proud to be one of his students.

I would like to express my sincere thanks to Dr. Jiang Changyun, my co-supervisor, for his invaluable advice and persistent assistance to my research. He has been closely associated with a significant part of my research and his knowledge and mastery in photovoltaic devices have been truly inspirational.

I would also like to express my gratitude towards Prof. E. T. Kang, Prof. Choi Wee Kiong and Dr. Zhang Jie. They supplied me the sufficient facilities to finish the experimental part in my research work. I am very grateful for their help.

My appreciation also goes to Dr. Zhang Chunfu, Mr. Chang Jingjing and Ms. Zhu Mei. They not only give me suggestions and support to my research but also provide me encouragement to overcome the difficulties in life. Most importantly, the friendship and comradeship we have built through the years are going to last a life

long. I would like to extend my appreciation to Dr. Liu Gang, Dr. Liu Yiliang, Mr. Xu Liqun, Mr. Cai Tao, Ms. Yang Wenjing, Mr. Kam Zhi Ming and all SNDL graduate students and technical staffs for their support and friendship.

I am grateful to my classmates and labmates. The time we spent together in lecture theatres, tutorial rooms, laboratories and canteens is going to be a memorable chapter in my life.

I would like to thank National University of Singapore and Ministry of Education, Singapore, for the generous financial support and scholarship.

I would like to give my recognition to Institute of Materials Research and Engineering for the lab facility support.

Last but not the least, I am indebted to my parents, my brother, my sister-in-law and my little cute niece for their unconditional love and endless support.

Lin Zhenhua

July 2013 in Singapore

Table of Contents

Summary

Inverted organic solar cells (OSCs) have attracted much attention due to their approved stability and compatibility with roll-to-roll processes since their initial studies. The nature of electrical contact between the active layer and cathode in inverted OSCs has significant effects on the device performance, thus modification of those interfaces by inserting appreciate interfacial layers can optimize the contact properties to improve the device performance. The purpose of this work is to investigate the mechanism of the metal oxide interlayers and develop novel interfacial layer materials to modify the interface for highly efficient OSCs. In this thesis, three types of cathode interfacial layers, atomic layer deposited (ALD) and solution processed metal oxides (zinc oxide (ZnO) and titanium oxide (TiO_x)), and polyelectrolyte (polyethyleneimine: poly(styrene sulfonate) sodium salt (PEI:PSS)), have been studied for inverted OSCs.

ALD-grown ZnO and TiO_x films are dense, stable and robust with the capability of conformal coating on nanostructural surfaces, showing a promising interfacial layers for OSCs. The low temperature ALD deposited metal-oxide thin films as the electron selective interlayer were conformally coated on the well-ordered periodic nano-groove structures to form the periodically nanostructured ITO-cathode/active-layer interfaces. By using ALD coating, it was found that the ITO patterns were maintained upon adding the metal oxide layer, thus avoiding the "flattening effect" which usually happens when spin coating poly(3,4-ethyl-enedioxythiophene) (PEDOT) layer on the ITO patterns. Meanwhile, the thickness of the interfacial layer between the ITO surface and the active layer was even and

precisely controlled, thus eliminating the influence of the thickness variation of the interfacial layer. As a result, the device performance especially the photocurrent has been significantly increased due to the enhanced charge collections and light absorption arising from the light trapping and also morphology improvement in the active layer.

Solution-processed metal oxides (ZnO and TiO_x) as cathode interfacial layer were developed, since the long-time consumption and non-cost effective ALD deposition process is not desirable for the cost-effective fabrication process for OSCs. Firstly, effects of different post-treatments (thermal, humidity, and vacuum) of aqueous solution processed ZnO buffer layer were investigated on the device performance of inverted OSCs in terms of surface structure and properties. It was found that the thermal and vacuum post-treatments not only reduced the film surface defect sites but also increased the film crystallinity compared to the reference film. Secondly, the device photo-stability of devices based on ZnO, TiO_x interlayers, and ZnO/TiO_x, TiO_x/ZnO bilayers has also been studied, since photo-induced degradation is a big obstacle for the commercialization of OSCs. It was found that devices based on TiO_x/ZnO bilayer obtained better device performance, and devices based on ZnO/TiO_x bilayer contained better photo-stability.

Polyelectrolyte complex, PEI:PSS, as the cathode interfacial layer was used for highly efficient inverted OSCs. It was found that the PEI:PSS cathode interfacial layer can induce an ohmic contact with the fullerene active layer and increase the built-in fields through significant reduction of the work function of ITO. Using blend of poly(3-hexylthiophene) (P3HT) and phenyl-C61-butyric acid methyl ester ($PC_{61}BM$) as the active layer, the OSC devices incorporating PEI:PSS as the cathode interfacial layer showed much increased power conversion efficiency (PCE) than

devices with ZnO or bare PEI interfacial layer. The combination of PEI:PSS with TiO_x bilayer exhibited excellent device performance by reducing the energy barrier for electron injection and transport and reducing the trap-assisted recombination. The S-shape in the current density – voltage (J – V) curves of devices based on TiO_x layers has been eliminated due to the reduced electron injection barrier. Meanwhile, it was found that device air stability based on PEI:PSS interfacial layer was better than devices based on ZnO layer. From the solution processability, air stability, and device performance, the polyelectrolyte, PEI:PSS, should be the best choice for interlayer in inverted solar cells.

List of Tables

List of Figures

List of Symbols and Abbreviations

α	Absorption coefficient
ε_0	Permittivity of free space
ε_r	Dielectric constant
λ	Wavelength
τ	Life time
A	Accepter
Al	Aluminum
AFM	Atomic force microscopy
Ag	Silver
ALD	Atomic layer deposition
AM	Air mass
Au	Gold
BHJ	Bulk heterojunction
C	Capacitance
C_{60}- SAM	Fullerene-based self-assembly monolayer
Ca	Calcium
Cr	Chromium
Cs_2CO_3	Caesium carbonate
Cs_2O	Caesium oxide
D	Diffusion coefficient
D	Donor
DCB	Dichlorobenzene
DEZ	Diethylzinc
E_{off}	Offset energy
ESL	Electron selective layer
FESEM	Field emission scanning electron spectroscopy
FF	Fill factor
FPQ-Br	Poly[9,9'-bis[6"-(N,N,Ntrimethylammonium)hexyl]fluorene-co-alt-phenylene]
H_2O	Water
HOMO	Highest occupied molecular orbital
I_o	Saturation current
IPA	Iso-propanol
IPCE	Incident photon-to-current efficiency
I_{ph}	Photocurrent
ITO	Indium tin oxide
J_{sc}	Short circuit current density
k_B	Boltzmann constant
L	Diffusion length
LUMO	Lowest unoccupied molecular orbital
MDMO-PPV	poly[2-methoxy-5(3',7'-dimethyloctyloxy)-1,4-phenylenevinylene
MoO_3	Molybdenum trioxide

n	Ideality factor
N_2	Nitrogen
Nc-ZnO	Nano crystalline collide zinc oxide
OSC	Organic solar cell
P3HT	Poly(3-hexylthiophene)
PAA	Polyallylamine
PCBM or $PC_{61}BM$	Phenyl-C61-butyric acid methyl ester
$PC_{71}BM$	Phenyl-C71-butyric acid methyl ester
PCDTBT	Poly[[9-(1-octylnonyl)-9H-carbazole-2,7-diyl]-2,5-thiophenediyl-2,1,3-benzothiadiazole-4,7-diyl-2,5-thiophenediyl]
PCE	Power conversion efficiency
PEDOT:PSS	Poly(3,4-ethyl-enedioxythiophene): poly(styrenesulfonate)
PEI	Polyethyleneimine
PEO	Poly(ethylene oxide)
PFN	Poly[(9,9-bis(3'-(N,N-dimethylamino)propyl)-2,7-fluorene)-alt-2,7-(9,9-dioctyfluorene)]
PL	Photoluminescence
P_{in}	Incident light power density
PTB7	Poly[[4,8-bis[(2-ethylhexyl)oxy]benzo[1,2-b:4,5-b']dithiophene-2,6-diyl][3-fluoro-2[(2 ethylhexyl)carbonyl]thieno[3,4-b]thiophenediyl]]
PV	Photovoltaic
q	Electron charge
R_s	Series resistance
R_{sh}	Shunt resistance
T	Temperature
$TiCl_4$	Titanium tetrachloride
TiO_2	Titanium dioxide
TiOx	Titanium oxide
UPS	Ultraviolet photoelectron spectroscopy
V_2O_5	Vanadium oxide
V_{bi}	Built-in potential
V_{oc}	Open circuit voltage
XPS	X-ray photoelectron spectroscopy
XRD	X-ray diffraction
ZnO	Zinc oxide

List of Publications

Journal Articles

1. **Z. Lin**, C. Jiang, C. Zhu and J. Zhang, “Development of Inverted Organic Solar Cells with TiO2 Interface Layer by Using Low-Temperature Atomic Layer Deposition”, ACS Applied Materials and Interfaces, 5, 713 – 718, 2013.

2. **Z. Lin**, J. Chang, Z. M. Kam, C. Jiang, J. Zhang, J. Wu and C. Zhu, “Enhanced Inverted Organic Solar Cell Performance by Post-treatments of Aqueous Solution-based ZnO Buffer Layers ”, in preparation.

3. **Z. Lin**, M. Zhu, J. Chang, C. Jiang, J. Zhang, J. Wu, W. K. Choi and C. Zhu, “Orderly nano-patterned ITO electrode combined with atomic layer deposited metal oxide interlayer for inverted organic solar cells”, in preparation.

4. **Z. Lin**, J. Chang, C. Jiang, J. Zhang, J. Wu and C. Zhu, ”Highly Efficient Inverted Organic Solar Cells with PEI:PSS as the Interfacial Layer”, in preparation.

5. J. Chang, **Z. Lin**, C. Zhu, C. Chi, J. Zhang and J. Wu, “Solution-Processed LiF-doped ZnO Films for High Performance Low Temperature Field Effect Transistors and Inverted Solar Cells”, ACS Applied Materials and Interfaces, **DOI:** 10.1021/am4014488, 2013.

6. S. Liu, **Z. Lin**, Q. Zhao, Y. Ma, H. Shi, M. Yi, Q. Ling, Q. Fan, C. Zhu, E. T. Kang and W. Huang, “Flash-Memory Effect for Polyfluorenes with On-Chain Iridium(III) Complex”, Advanced Functional Materials, 21, 979 – 985, 2011.

7. P. Wang, S. Liu, **Z. Lin**, X. Dong, Q. Zhao, W. Lin, M. Yi, S. Ye, C. Zhu and W. Huang, “Design and Synthesis of Conjugated Polymers Containing Pt(II) Complexes in the Side-Chain and Their Application in Polymer Memory Devices”, Journal of Materials Chemistry, 22, 9576 – 9583, 2012.

8. C. Zhang, H. You, **Z. Lin** and Y. Hao, “Inverted Organic Photovoltaic Cells with Solution-Processed Zinc Oxide as Electron Collecting Layer”, Japanese Journal of Applied Physics, 50, 082302, 2011.

9. C. Zhang, Y. Hao, S. Tong, **Z. Lin**, Q. Feng, E.-T. Kang and C. Zhu, “Effects of Cathodes Confinement on the Performance of Polymer/Fullerene Photovoltaic Cells in the Thermal Treatment”, IEEE Transactions on Electron Devices, 58, 835 - 842, 2011.

10. C. Zhang, J. Zhang, Y. Hao, **Z. Lin** and C. Zhu, “A Simple and Efficient Solar Cell Parameter Extraction Method form a Single Current-Voltage Curve”, Journal of Applied Physics, Vol. 110, pp. 064504, 2011.

Conference Papers

1. **Z. Lin**, C. Zhang, E. T. Kang and C. Zhu, “Characterization of Annealing Effects of P3HT:PCBM Solar Cells with E-beam Deposited Cathodes by Simple Equivalent Circuit Parameter Extraction Method”, IEEE International Conference on Solid-State and Integrated Circuit Technology 2010.

2. C. Zhang, **Z. Lin**, E. T. Kang and C. Zhu, “Mechanism Investigation and Structure Design of Organic Solar Cells for Improved Energy Conversion Efficiency”, ”, IEEE International Conference on Solid-State and Integrated Circuit Technology 2010.

Chapter 1

Introduction

With the continuously increasing global energy demand, energy crisis and environmental issues have been highly concerned by the entire world. Until today, most of the energy production still comes from fossil fuels (coal, oil and neutral gas) [1.1]. However, the utilization of the fossil fuels is not environmental friendly due to the generation of carbon dioxide which has a detrimental long term effect on the neutral balance and induces greenhouse effect [1.2]. Meanwhile, the fossil fuels are not regenerative energy and will expire one day. Thus, renewable and clean energy is urgently needed.

In the past few decades, solar energy has received a great deal of interests due to its abundant, regenerative and clean properties. The total solar energy absorbed by Earth's surface is approximately 3,850,000 exajoules (EJ) per year which is much higher than the yearly human primary energy consumption (510 EJ in 2009). It has been widely recognized that solar energy is the promising candidate of the renewable and clean energy. In 2011, the International Energy Agency said that "*the development of affordable, inexhaustible and clean solar energy technologies will have huge longer-term benefits. It will increase countries' energy security through reliance on an indigenous, inexhaustible and mostly import-independent resource, enhance sustainability, reduce pollution, lower the cost of mitigating climate change, and keep fossil fuel prices lower than otherwise. These advantages are global. Hence the additional costs of the incentives for early development should be considered learning investments; they must be spent and need to be widely shared*" [1.3].

Photovoltaic (PV) technology has been considered as the essential method to utilize the solar energy. Solar cells are solid state electrical devices which act as energy converters and convert the solar energy to electrical energy directly from the sunlight by the photovoltaic effect, which provides us a great opportunity to utilize the solar energy source. Typically, there are two types of photovoltaic devices: inorganic solar cells (silicon solar cells) and organic solar cells (OSCs). Inorganic solar cells (silicon solar cells) have already provided highly efficient performance. However, their fabrication process is much more expensive compared with OSCs. OSCs have their unique advantages such as capability of low-cost, large area fabrication process, and light weight compared with inorganic solar cells, which makes them as the promising photovoltaic technology to tackle the energy and environmental issues.

1.1 A brief overview of organic solar cells

1.1.1 Background and historical development of OSCs

Organic solar cells have attracted much attention in recent years due to their potential for energy-efficient, low-cost, large-area and high-volume processability.

The first study of OSCs was reported by Kallman and Pope in 1959. The device had a single layer structure with extremely low power conversion efficiency (PCE) of 2 x 10^{-4} [1.5]. In this single layer structure, an organic semiconductor layer is sandwiched between a low work-function metal (cathode) and high work-function metal (anode), as shown in Fig. 1.1 (a). Even though the single-layer OSCs tend to produce a reasonable open circuit voltage (V_{oc}) of 0.2 V, their photocurrent is typically low because the photo-generated electron and hole in conjugated polymers

have a strong tendency to recombine with each other. Due to this inherent limitation, the PCE was only improved to 0.36 % from early 1970s to early 1980s [1.6]. Since this type of solar cells only contains one organic semiconductor material in the active layer, they are also known as homojunction solar cells.

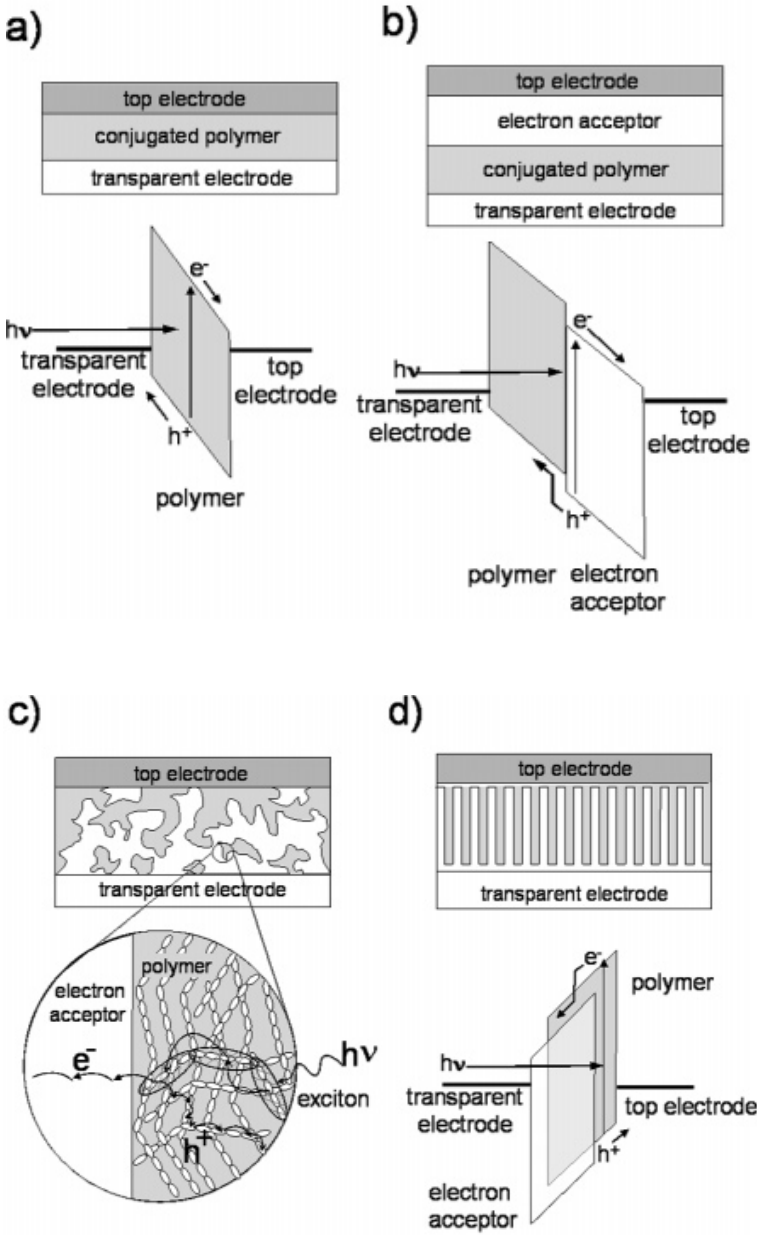

Figure 1.1 Four device architectures of conjugated polymer-based photovoltaic cells: (a) single-layer OSC; (b) bilayer OSC; (c) disordered bulk heterojunction; (d) ordered bulk heterojunction [1.4].

The next generation of OSCs is the bilayer solar cell which is a major breakthrough firstly demonstrated by Tang in 1986 [1.7]. In the bilayer structure, an interface is formed between two different layers, the electron donor (D) and electron acceptor (A). These two layers of materials have difference in electron affinity and ionization energy. Therefore, electrostatic forces are generated at the interface. The layer with higher electron affinity and ionization potential is the electron accepter and the other one is the electron donor. Based on two organic materials, perylene tetracarboxylic derivative and copper phthalocyanine (CuPc), a PCE of 0.95 % was achieved due to the improved exciton dissociation at the D/A interface [1.7]. The process of charge transfer led to spatial separation of electron and hole, which prevents the direct electron and hole recombination. However, there are still some drawbacks. Since excitons need to be generated near the interface for dissociation to occur before recombination, it requires the exciton diffusion length typically less than absorption length of the material. Meanwhile, since most of the organic materials are p-type, it was a great challenge to select a well matched n-type organic material as the electron acceptor. In 1992, ultrafast photo-induced transfer at the interface between a conjugated polymer and the Buckminster fullerene C_{60} was found [1.8]. Further improvement was made in 1995, soluble fullerene derivative, phenyl-C61-butyric acid methyl ester (PCBM) was chemically synthesized, which has been the most popular acceptor used in organic solar cells [1.9].

Another revolutionary development in OSCs came with the introduction of bulk heterojunction (BHJ) invented by Yu *et al.* in 1995 [1.10]. In a BHJ solar cell, the donor and accepter materials are blended together, which forms the interpenetrating and bi-continuous network in the active region of OSCs. In the ideal condition of BHJ as shown in Fig. 1.1(c), this structure cannot only ensure the high

efficient excition dissociation but also guarantee the carrier transport. Because of these merits, BHJ structure has been intensively studied in the past decades and the performance of OSCs has been steadily improved by optimizing fabrication processes and materials. The first successful attempt occurred in 2001, a PCE of 2.5 % based on poly[2-methoxy-5(3',7'-dimethyloctyloxy)-1,4-phenylenevinylene (MDMO-PPV) and PCBM was achieved by changing the solvent from toluene to chlorobenzene, which results in a smoother surface morphology and a better donor and accepter percolation due to the reduced active layer domain size [1.11]. After that, post-annealing process was investigated in the fabrication process in 2003 [1.12], which allows re-organization of the poly(3-hexylthiophene) (P3HT) chains and thus improves P3HT crystallinity, resulting in a high PCE of 3.5 %. Following that, in 2005, slow solvent evaporation rate was found to enhance the hole mobility and balance the charge transport by increasing the donor crystallinity, which led to an extremely high fill factor (FF) and a high efficiency of 4.4% [1.13]. The efficiency was further improved up to 5.5% via processing additive addition in 2006 by Peet *et al.* [1.14]. The addition of processing additive enhances the active layer phase separation, thus increases the photo-responsivity and hole mobility.

1.1.2 Motivation of inverted OSCs

Most investigated so far OSCs have the following structure in common: substrate/transparent anode/hole transport layer/active layer/cathode, usually referred as the conventional structure as shown in Fig. 1.2 (a). In this device structure, a low work-function metal, such as aluminum (Al) and calcium (Ca), is deposited on top of active layer as the electron-collector cathode and indium-tin-oxide (ITO) usually

works as the transparent anode. However, the low work-function metal in this architecture can be easily oxidized in air ambient. Meanwhile, an acidic poly(3,4-ethyl-enedioxythiophene): poly(styrenesulfonate) (PEDOT:PSS) hole transport layer is used in the conventional structure. Since PEDOT:PSS is acidic in nature, it can cause the etching of ITO electrode, resulting in interface instability through indium diffusion into the active layer. Both the low work-function metal and acidic PEDOT:PSS layer degrade device performance easily in air, leading to poor stability [1.15-1.17].

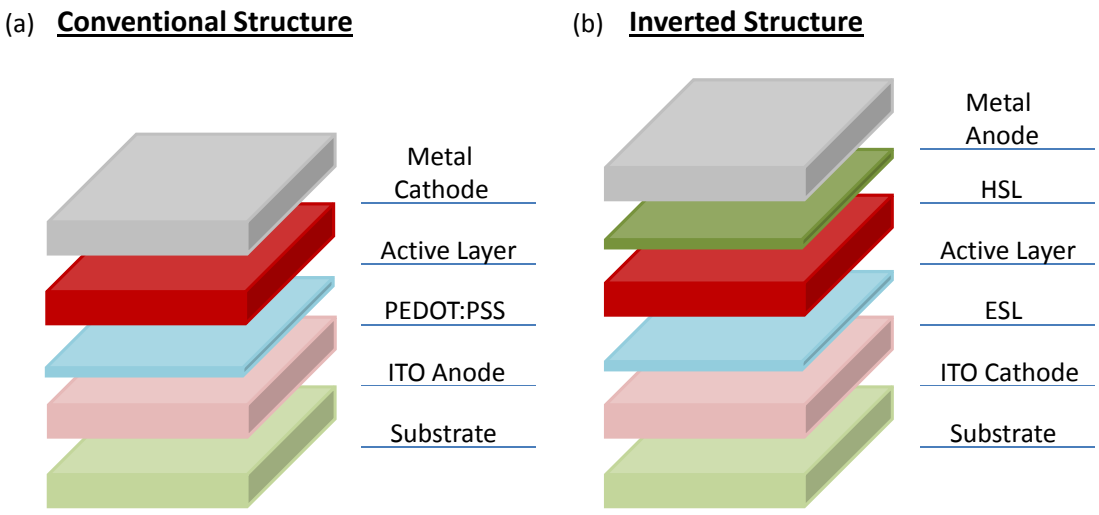

Figure 1.2 OSC device architecture studied: (a) conventional structure and (b) inverted structure. ESL and HSL indicate electron selective layer and hole selective layer respectively.

One attempt to improve the air stability of OSCs is to use inverted structure which has attracted much attention due to their approved stability and compatibility with roll-to-roll processes since their initial studies [1.18-1.20]. An inverted OSC has the following structure: substrate/cathode/electron selective layer/active layer/hole selective layer/anode, where both the low work-function metal cathode and PEDOT:PSS layer can be avoided, as shown in Fig. 1.2 (b).

In the inverted structure, a high work-function metal, such as silver (Ag) and gold (Au), is deposited on top of the device and exposed to the air. The ITO electrode can still be used in the inverted structure but works as electron-collector cathode. The ITO work-function is 4.7 to 5.1 eV, lying between the typical highest occupied molecular orbital (HOMO) and lowest unoccupied molecular orbital (LUMO) of common active layers (such as P3HT:PCBM), which makes it possible to collect either holes or electrons depending mainly on the property of interfacial layer coated on top of the ITO surface. In the inverted structure, a cathode interfacial layer which can lower the work-function of ITO surface is applied. This cathode interfacial layer plays an important role in inverted OSCs, which will be intensively and comprehensively studied in this thesis.

1.2 Background of cathode interfacial layer in inverted OSCs

1.2.1 Roles of cathode interfacial layer

The nature of electrical contact between the active layer and cathode in inverted OSCs has significant effects on the device performance, thus modification of those interfaces by inserting appreciate interfacial layers can optimize the contact properties to improve the device performance. There are several important roles served by the interfacial layers.

Firstly, the interfacial layer can tune the energy level alignment at the electrode/active layer to enhance charge extraction. In most of the inverted OSCs, the high work-function of the bottom ITO cathode hampers the formation of an ohmic contact with the LUMO level of the fullerene to facilitate photo-generated charge

carrier collection. A proper interfacial layer can modify the electrode surface and promote ohmic contact due to the interfacial effects, such as charge transfer, dipole formation and interface states formation [1.46].

Secondly, interfacial layers can define the polarity of the electrode and improve the charge selectivity. Since interfacial layers can be used to tune electrode work-functions, they can improve the charge carrier selectivity by matching the Fermi level to either the positive integer charge-transfer state of the donor or negative integer charge-transfer state of the accepter for hole or electron collection, respectively. Thus, the interfacial layer with a deep lying HOMO can block the flow of holes, and that with a low lying LUMO can block the flow of electrons. Besides, interfacial layers with bandgaps larger than those of the donor and accepter can block excitons reaching to the electrode (exciton blocking layer).

Thirdly, interfacial layers can modify the surface morphology of the active layer. Tuning the surface energy and surface chemistry via self-assembly monolayer (SAM) based interfacial layers provides powerful meaning to manipulate the vertical and lateral phase separation of the BHJ film [1.47]. The effect of substrate surface energy on the vertical separation of active layer has been investigated using the P3HT:PCBM system. It was found that P3HT is enriched at the top of the active layer while PCBM enriched at the bottom of the active layer because P3HT has a slightly lower surface energy (26.9 mN m^{-2}) than that of PCBM (37.8 mN m^{-2}) [1.48], which is favourable for inverted structure.

Fourthly, interfacial layers can be used as optical spacers and introduce plasmonic effects to modulate light absorption in the active layer. Though high energy and narrow spectral range of absorption band result in inefficient absorption

efficiency and thicker active layer to enhance the light absorption, the low carrier mobilities limit the active layer thickness to be ~ 100 nm. To solve such dilemma, light trapping or optical-field arrangement strategy is used, which decreases the recombination loss by interface or morphology engineering. Optical spacers [1.49] and plasmonic nanostructures [1.50] are useful light trapping strategies and can be achieved by interface engineering.

Finally, interfacial layer can improve the interface stability between the active layer and electrodes. Stability is an important aspect which needs improvement for OSCs compared with inorganic solar cells. Interfacial layers can protect the electrode metal from penetrating into the active layer and prevent the moisture and oxygen diffusion. Air-stable OSCs with atomic layer deposited (ALD) titanium dioxide (TiO_2) modified interlayers have been successfully demonstrated [1.51]. The OSC devices had very little degradation after being stored in air for 100 days without encapsulation.

1.2.2 Cathode interfacial materials in inverted OSCs

One key challenge in making efficient inverted OSCs lies in the cathode interfacial layers and their properties when contacting cathode and active layer. There are several key parameters which determine a material's utility as cathode interfacial layer. It has to be transparent, provide ohmic contact with the acceptor material, have suitable energy levels to efficiently transport negative carriers (electron transporting) and block positive carriers (hole blocking), and be chemically inert with respect to those layers. The device characteristics of the representative inverted OSCs with different cathode interfacial layers and active layers are summarized in Table 1.1 and

the energy levels of these active materials and commonly used electron and hole selective materials are illuminated in Fig. 1.3.

Alkali metal salt, caesium carbonate (Cs_2CO_3), has been demonstrated as an interfacial modifier to tune the ITO work-function for electron selection in inverted OSCs [1.21]. Cs_2CO_3 interfacial layer can be either thermally evaporated or spin-coated onto ITO cathode. By using spin-coated Cs_2CO_3 as an ITO cathode modifier and vanadium oxide (V_2O_5) as hole selective layer, a PCE of 2.25% was achieved for the inverted P3HT:PCBM OSC [1.22]. The performance of ITO/ Cs_2CO_3/P3HT:PCBM/ V_2O_5/Al device was further improved by annealing spin-coated Cs_2CO_3 at 150 ^oC, and the PCE was increased from 2.3% (non-annealed device) to 4.2% [1.23]. The 150 ^oC annealing process decomposes Cs_2CO_3 into doped caesium oxide (Cs_2O), which reduces ITO work-function from 4.7 eV to 3.06 eV [1.24], resulting in significantly improved electron collection. However, due to the insulating property of Cs_2O, the application of Cs_2CO_3 in OSC is limited.

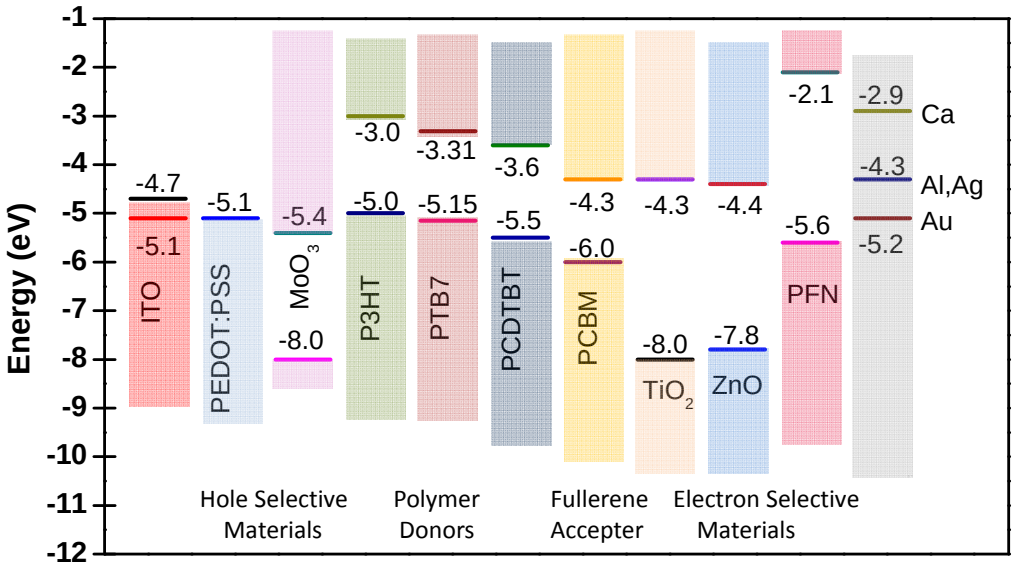

Figure 1.3 Schematic view of energy gaps and energy levels of some components of recent OSCs including transparent electrodes, hole selective materials, polymer donors, fullerene acceptor, electron selective materials and metal electrodes. The solid lines correspond to the work functions of the materials.

Metal oxides, TiO_2 and zinc oxide (ZnO), are widely used as cathode interfacial layer in inverted OSCs. TiO_2 and ZnO are highly n-type metal oxides and their suitable energy levels promote ohmic contact formation with the active layer to accept electrons while block holes. Various methods have been used to fabricate TiO_2 and ZnO layers, including sol-gel or suspension solution processing [1.25-1.26], sputtering [1.27], and atomic layer deposition (ALD) [1.28-1.29]. Significant research efforts have been focused to improving their electrical and morphological properties.

The inverted OSC device with low-temperature sol-gel fabricated TiO_x interfacial layer shows a PCE of 3.1% based on P3HT:PCBM active blend [1.18]. The device performance was further improved (PCE 3.6%) by TiO_x layer to be modified with a polyfluorene-based polymer electrolyte (FPQ-Br) [1.30]. The polymer electrolyte can induce interfacial dipoles to lower the ITO surface work-function, resulting in reduced contact resistance. Some papers have reported light soaking problem of TiO_x based inverted OSCs, attributed to desorption of oxygen species [1.29, 1.31].

ZnO is another candidate to be studied as cathode interfacial layer due to its high electron mobility and high transparency in the visible wavelength range which allow it to be an effective transporter and excellent wave guide [1.32-1.33]. White *et al.* have demonstrated one of the earliest inverted P3HT:PCBM OSCs based on a sol-gel derived ZnO film as electron selective layer [1.34]. Recently, very high efficient inverted OSCs with sol-gel fabricated ZnO layers have been reported with PCEs of 6.6% and 7.3% [1.35]. To further improve the device performance, fullerene-based self-assembly monolayers (C_{60}- SAMs) [1.36-1.37] and corss-linked fullerenes (C-PCBSD) [1.38] have been employed to modify ZnO interfacial layer.

Organic materials have also been demonstrated as cathode interfacial layer in inverted OSCs. Alcohol-/water-soluble polymer-based interfacial materials, such as poly[(9,9-bis(3'-(N,N-dimethylamino)propyl)-2,7-fluorene)-alt-2,7-(9,9-dioctyfluorene)] (PFN) [1.39], poly(ethylene oxide) (PEO) [1.40,1.45], polyallylamine (PAA) [1.41] and polyethyleneimine (PEI) [1.41], have been employed because they can lower down the work function of ITO cathode and facilitate photo-generated charge-carrier collection by forming interfacial dipoles [1.42-1.43]. These polymers are large band-gap insulators so they should not be considered as charge-injection layers but as a surface modifier. Very high performance of inverted OSC device with PFN layer based on poly[[4,8-bis[(2-ethylhexyl)oxy]benzo[1,2-b:4,5-b']dithiophene-2,6-diyl][3-fluoro-2[(2 ethylhexyl) carbonyl]thieno[3,4-b]thiophenediyl]]: phenyl-C71-butyric acid methyl ester (PTB7:$PC_{71}BM$) blend with a PCE of 9.2 % has been reported in a recent study [1.39].

Table 1.1 Summary of device characteristics of representative inverted OSCs employing different interfacial layers.

Cathode Configuration	Active Layer	Anode Configuration	Voc (V)	Jsc (mA/cm^2)	FF	PCE (%)	Ref.
ITO/Cs_2CO_3	P3HT:$PC_{61}BM$	V_2O_5/Al	0.56	8.42	0.62	2.25	1.22
ITO/Cs_2CO_3	P3HT:$PC_{61}BM$	V_2O_5/Al	0.59	11.13	0.64	4.19	1.23
ITO/TiO_x(sol-gel)	P3HT:$PC_{61}BM$	PEDOT:PSS/Au	0.56	9.0	0.62	3.1	1.18
ITO/TiO_x(ALD)	P3HT:$PC_{61}BM$	MoO_3/Ag	0.54	10.16	0.60	3.31	1.29
ITO/TiO_x/FPQ-Br	P3HT:$PC_{61}BM$	MoO_3/Au	0.58	8.9	0.70	3.6	1.30
ITO/ZnO (sol-gel)	P3HT:$PC_{61}BM$	MoO3/Ag	0.61	9.29	0.56	3.30	1.32
ITO/ZnO (sol-gel)	PDTGTPD: $PC_{71}BM$	MoO_3/Ag	0.85	12.6	0.68	7.3	1.35
ITO/ZnO (sol-gel)	PCDTBT: $PC_{71}BM$	MoO_3/Ag	0.88	10.4	0.69	6.3	1.44
ITO/ZnO/C_{60}-SAM	P3HT:$PC_{61}BM$	PEDOT:PSS/Ag	0.63	12.0	0.61	4.5	1.37
ITO/ZnO/C-PCBSD	P3HT:$PC_{61}BM$	PEDOT:PSS/Ag	0.60	12.8	0.58	4.4	1.38
ITO/PFN	PTB7:$PC_{71}BM$	MoO_3/Ag	0.754	17.42	0.70	9.21	1.39
ITO/PEO	APFO-3:PCBM	PEDOT-EL/PH500	0.67	2.3	0.45	0.70	1.45

1.3 Outline of the study

In Chapter 2, the basic working principles of the organic solar cells (OSCs) are introduced first: light absorption, exciton diffusion, exciton dissociation and charge transport. Following that, materials and experimental methods, device characterization will be demonstrated. After that, important parameters in OSCs are introduced and the theory of single-diode model for equivalent circuit parameter extraction is presented. In this chapter, the fundamental knowledge about OSCs is briefed.

In Chapter 3, device performance with ALD deposited TiO_2 and ZnO as the interface layer in inverted solar cells is demonstrated. The effects of ALD temperature, TiO_2 film thickness and light-soaking treatment on cell performance are also investigated. Since low temperature ALD deposited metal oxide film has the capability in achieving uniform, dense and highly conformal films on 2D and 3D surfaces, they are applied and combined with nano-patterned ITO to further improve the device performance.

Due to the high cost fabrication process and long-time consumption of ALD process, aqueous solution processed ZnO and sol-gel processed TiO_x films as the cathode interface layers are introduced. In Chapter 4, firstly, effects of different post-treatments using thermal, humidity, and vacuum on aqueous solution-processed ZnO buffer layers on the film properties and inverted OSC device performance are investigated. It shows that the post-treatments significantly affected device short circuit current, thus device performance. Secondly, the device performance and photo-stability of cells based on different interfacial layers, ZnO, TiO_x, ZnO/TiO_x and TiO_x/ZnO, are also clearly demonstrated. The results show that devices based on

TiO_x/ZnO bilayer can achieve better performance, and those based on ZnO/TiO_x bilayer can obtain better photo-stability.

In Chapter 5, highly efficient inverted OSCs with a new ion pair polymers, branched polyetherimide:poly(styrenesulfonate) (PEI:PSS), as the cathode interfacial layer is demonstrated. The PEI:PSS layer induces an ohmic contact with the LUMO level of the fullerene and increases the built-in fields due to the significantly reduced work function of ITO. The x-ray photoelectron spectroscopy (XPS) and ultraviolet photoelectron spectroscopy (UPS) analysis indicates that the work-function of ITO has a significant decrease after coating with PEI:PSS films. The reduced work-function results from the electrostatic interfacial dipoles. Solution processed TiO_x and combination with PEI:PSS as cathode interfacial layer in inverted OSCs are also investigated. The introduction of TiO_x surface modification agent is mainly to eliminate the light soaking problem and further improve the device performance.

At last, the most important results of this work are summarized and some suggestions for future work are discussed in Chapter 6.

References

[1.1] World energy resources and consumption: http://en.wikipedia.org/wiki/World_energy_resources_and_consumption#cite_note-gcep-9.

[1.2] United Nations Environment Programme (UNEP), Global environment outlook (GEO yearbook 2009), web site: www.unep.org/geo/yearbook/2009.

[1.3] "Solar Energy Perspectives: Executive Summary", International Energy Agency 2011.

[1.4] K. M. Coakley, and M. D. McGehee, Chemistry of Materials 16, 4533 – 4542 (2004).

[1.5] H. Kallmann and M. Pope, Journal of Chemical Physics 30, 585 – 586 (1959).

[1.6] G. A. Chamberlain, Solar Cells 8, 47 – 83 (1983).

[1.7] C. W. Tang, Applied Physics Letters 48, 183 – 185 (1986).

[1.8] N.S. Sariciftci, L. Smilowitz, A. J. Heeger and F. Wudl, Science 258, 1474 – 1476 (1992).

[1.9] J. C. Hummelen, B. W. Knight, F. LePeq, F. Wudl, J. Yao and C. L. Wilkins, Journal of Organic Chemistry 60, 532 – 538 (1995).

[1.10] G. Yu, J. Gao, J. C. Hummelen, F. Wudl and A. J. Heeger, Science 270, 1789 – 1791 (1995).

[1.11] S. E. Shaheen, C. J. Brabec, N. S. Sariciftci, F. Padinger, T. Fromherz and J. C. Hummelen, Applied Physics Letters 78, 841 – 843 (2001).

[1.12] F. Padinger, R.S. Rittberger and N. S. Sariciftci, Advanced Functional Materials 13, 85 – 88 (2003).

[1.13] G. Li, V. Shrotriya, J. Huang, Y. Yao, T. Moriarty, K. Emery and Y. Yang, Nature Materials 4, 864 – 868 (2005).

[1.14] J. Peet, C. Soci, R. C. Coffin, T. Q. Nguyen, A. Mikhailovsky, D. Moses and G. C. Bazan, Applied Physics Letters 89, 252105 (2006).

[1.15] M.P. de Jong, L.J. van Ijzendoom and M. J. A. de Voigt, Applied Physics Letters 77, 2255 – 2257 (2000).

[1.16] G. Greczynski, T. Kugler, M. Keil, W. Osikowicz, M. Fahlman and W.R. Salaneck, J. Electron spectroscopy and Related Phenomena 121, 1 – 17 (2001).

[1.17] A. K. K. Kyaw, X. W. Sun, C. Y. Jiang, G. Q. Lo, D.W. Zhao and D.L. Kwong, Applied Physics Letters 93, 221107 (2008).

[1.18] C. Waldauf, M. Morana, P. Denk, P. Schilinsky, K. Coakley, S. A. Choulis and C. J. Brabec, Applied Physics Letters 89, 233517 (2006).

[1.19] L.-M. Chen, Z. Hong, G. Li, and Y. Yang, Advanced Materials 21, 1434 – 1449 (2009).

[1.20] S. K. Hau, H.-L. Yip and A. K. Y. Jen,Polymer Review 50, 474 – 510 (2010).

[1.21] M. Reinhard, J. Hanisch, Z. Zhang, E. Ahlswede, A. Colsmann and U. Lemmer, Applied Physics Letters 98, 053303 (2011).

[1.22] G. Li, C. W. Chu, V. Shrotriya, J. Huang and Y. Yang, Applied Physics Letters 88, 253503 (2006).

[1.23] H.-H Liao, L.-M. Chen, Z. Xu, G. Li and Y. Yang, Applied Physics Letters 92, 173303 (2008).

[1.24] J. S. Huang, G. Li and Y. Yang, Advanced Materials 20, 415 – 419 (2008).

[1.25] A. K. K. Kyaw, X. W. Sun, C. Y. Jiang, G. Q. Lo, D.W. Zhao and D.L. Kwong, Applied Physics Letters 93, 221107 (2008).

[1.26] J. Y. Kim, S. H. Kim, H.-H. Lee, K. Lee, W. Ma, X. Gong and A. J. Heeger, Advanced Materials 18, 572 – 576 (2006).

[1.27] S. K. Hau, H.-L. Yip, O. Acton, N. S. Baek, H. Ma and A. K. Y. Jen, Journal of Materials Chemistry 18, 5113 – 5119 (2008).

[1.28] N. O. V. Plank, M. E. Welland, J. L. Macmanus-Driscoll and L. Schmidt-Mende, Thin Solid Films 516, 7218 – 7222 (2008).

[1.29] Z. Lin, C. Jiang, C. Zhu and J. Zhang, ACS Applied Materials and Interfaces 5, 713 – 718 (2013).

[1.30] H. Choi, J. S. Park, E. Jeong, G.-H. Kim, B. R. Lee, S. O. Kim, M. H. Song, H. Y. Woo, and J. Y. Kim, Advanced Materials 23, 2759 – 2763 (2011).

[1.31] H. Sun, J. Weickert, H. C. Hesse and L. Schmidt-Mende, Solar Energy Materials and Solar Cells 95, 3450 – 3454 (2011).

[1.32] Z. Liang, Q. Zhang, O. Wiranwetchayan, J. Xi, Z. Yang, K. Park, C. Li and G. Cao, Advanced Functional Materials 22, 2194 – 2201 (2012).

[1.33] M. Wang, Y. Li, H. Huang, E. D. Peterson, W. Nie, W. Zhou, W. Zeng, W. Huang, G. Fang, N. Sun, X. Zhao and D. Carroll, Applied Physics Letters 98, 103305 (2011).

[1.34] M. S. White, D. C. Olson, S. E. Shaheen, N. Kopidakis and D. S. Ginley, Applied Physics Letters 89, 143517 (2006).

[1.35] C.M. Amb, S. Chen, K. R. Graham, J. Subbiah, C. E. Small, F. So and J. R. Reynolds, Journal of the American Chemical Society 133, 10062 – 10065 (2011).

[1.36] S. K. Hau, Y.-J. Cheng, H.-L. Yip, Y. Zhang, H. Ma and A. K. Y. Jen, ACS Applied Materials and Interfaces 2, 1892 – 1902 (2010).

[1.37] S. K. Hau, H.-L. Yip, H. Ma and A. K. Y. Jen, Applied Physics Letters 93, 233304 (2008).

[1.38] C.-H. Hsieh, Y.-J. Cheng, P.-J. Li, C.-H. Chen, M. Dubosc, R.-M. Liang and C.-S. Hsu, Journal of the American Chemical Society 132, 4887 – 4893 (2010).

[1.39] Z. He, C. Zhong, S. Su, M. Xu, H. Wu and Y. Cao, Nature Photonics 6, 591 – 595 (2012).

[1.40] F. L. Zhang, F. Sedar and O. Inganäs, Advanced Materials 19, 1835 - 1838 (2007).

[1.41] H. Kang, S. Hong, J. Lee and K. Lee, Advanced Materials 24, 3005 – 3009 (2012).

[1.42] C. He, C. Zhong, H. Wu, R. Yang, W. Yang, F. Huang, G. Bazan and Y. Cao, Journal of Materials Chemistry 20, 2617 – 2622 (2010).

[1.43] J. H. Seo and T.-Q. Nguyen, Journal of the American Chemical Society 130, 10042 – 10043 (2008).

[1.44] Y. Sun, J. H. Seo, C. J. Takacs, J. Seifter and A. J. Heeger, Advanced Materials 23, 1679 – 1683 (2011).

[1.45] Y. Zhou, F. Li, B. Barrau, W. Tian, O. Inganas and F. Zhang, Solar Energy Materials and Solar Cells 93, 497 – 500 (2009).

[1.46] H. Ishii, K. Sugiyama, E. Ito and K. Seki, Advanced Materials 11, 605 – 625 (1999).

[1.47] X. Bulliard, S.-G. Ihn, S. Yun, Y. Kim, D. Choi, J.-Y. Choi, M. Kim, M. Sim, J.-H. Park, W. Choi and K. Cho, Advanced Functional Materials 20, 4381 – 4387 (2010).

[1.48] D. S. Germack, C. K. Chan, B. H. Hamadani, L. J. Richter, D. A. Fischer, D. J. Gundlach and D. M. DeLongchamp, Applied Physics Letters 94, 233303 (2009).

[1.49] J. Gilot, I. Barbu, M. M. Weink and R. A. J. Janssen, Applied Physics Letters 91, 113520 (2007).

[1.50] K. Tvingstedt, N.-K. Persson, O. Inganas, A. Rahachou and I. V. Zozoulenko, Applied Physics Letters 91, 113514 (2007).

[1.51] S.-Y. Park, H. O. Seo, K.-D. Kim, J. E. Lee, J.-D. Kwon, Y. D. Kim and D. C. Lim, Physica Status Solidi Rapid Research Letters 6, 196 (2012).

Chapter 2

Organic Solar Cell Fundamentals

Compared with inorganic semiconductors such as silicon (Si), organic materials have their unique advantages. First, the material consumption in the production is expected to be low because organic materials usually have high optical light absorption which offers the possibility to fabricate thin film device. Meanwhile, low-cost fabrication technologies, such as various coating methods, can be applied due to the material soluble property. One more attractive advantage is that organic materials have the property of flexibility so it is possible for devices to be fabricated using high-throughput, low-temperature printing techniques in a roll-to-roll process [2.1, 2.2]. It is expected that flexible plastic solar cells will create a completely new market in the field of low-cost devices. In this chapter, the fundamentals of OSCs, including device working principle, materials and experimental methods, device characterization and device parameter extraction, will be introduced.

2.1 Basic device working principles

Organic semiconductor materials generally have a relatively lower dielectric constant ($\varepsilon_{r(P3HT)} \approx 4.4$ and $\varepsilon_{r(PCBM)} \approx 3.9$ [2.3]) compared with inorganic semiconductor Si ($\varepsilon_{r(Si)} \approx 11.68$ [2.4]), which induces a high exciton binding energy (~ 0.5 eV) [2.5]. When light is absorbed, excitons which are electron-hole pairs are generated due to the attractive Columbic potential. Because of the electrical neutrality, excitons themselves cannot contribute to the photocurrent. In order to convert solar

energy into electrical energy, excitons must first be dissociated into free electrons and holes which can be collected by the electrodes. For Si solar cells, the thermal energy at room temperature (k_BT = 0.025 eV) is sufficient to dissociate an exciton into a positive and negative charge carrier. However, for organic semiconductor materials, because the excition binding energy is larger than the thermal energy at room temperature, excitons created by light absorption cannot be dissociated by thermal excitation. The method to solve this problem is to use two types of materials those differ in electron donating and accepting properties. Thus, excitons can be dissociated by the photo-induced charge transfer reaction.

Generally, there are four separate steps for OSCs to finish the energy conversion: (1) light absorption and exciton generation, (2) exciton diffusion, (3) exciton dissociation and free carrier generation, and (4) free carrier transport and collection, as shown in Fig. 2.1.

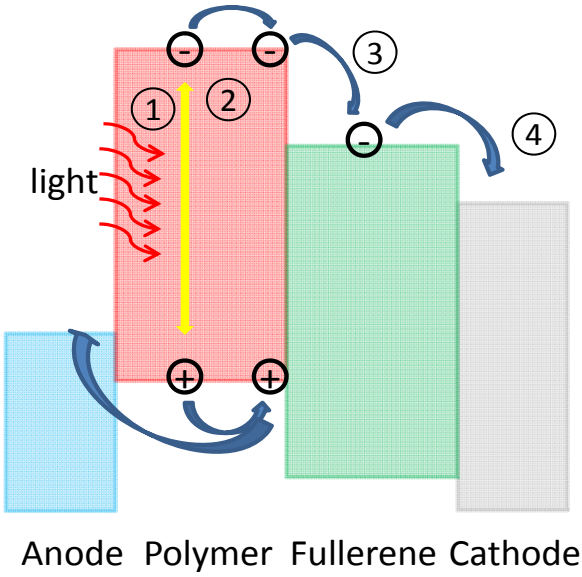

Figure 2.1 Schematic illumination of the working principle of an OSC. Four steps for OSCs to finish the energy conversion: (1) light absorption and exciton generation, (2) exciton diffusion, (3) exciton dissociation and free carrier generation, and (4) free carrier transport and collection.

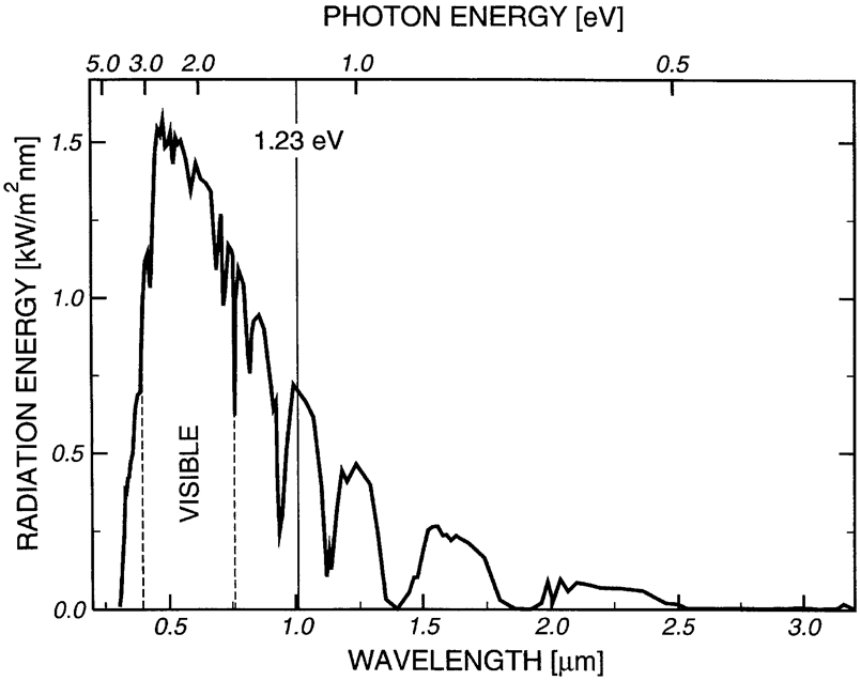

Figure 2.2 Solar energy spectrum (AM of 1.5) in terms of radiation energy vs. photon wavelength [2.6].

Light absorption and exciton generation

High light absorption is desired because it directly determines the device performance. There are three parameters which relate to the material light absorption ability: the light absorption coefficient, the material energy bandgap, and the film thickness. Firstly, for organic semiconductor materials, they already have high light absorption coefficient, 10^5 cm^{-1} in visible range, compared with Si (10^3 ~ 10^4 cm^{-1}) [2.7]. High light absorption allows thin film active layer fabrication resulting in less material usage, which is cost-effective. Secondly, to achieve high broadband light absorption and to better match the solar spectrum, low bandgap semiconductor materials are desired. This is because more than 60 % of the total solar energy lies in the wavelength region above 600 nm, corresponding to the bandgap below 2.0 eV, as shown in Fig. 2.2 [2.6]. Finally, large thickness can also enhance device light

absorption. However, when the film thickness is too large, the charge carrier transport will be limited, so the film thickness should be optimized to balance the dilemma.

Exciton diffusion

Excitons can only effectively dissociate at the donor and accepter (D/A) interface due to the large exciton binding energy, and before they dissociate, they can also decay radiatively or non-radiatviely. Thus, to obtain free carrier charges, after excitons generated from the light absorption, they must reach to the D/A interface before electron and hole recombine. Since excitons are electrically neutral, the exciton motion is dominated by random diffusion. The diffusion length is defined by

$$L = (D_\tau)^{0.5}, \qquad \text{(Eq. 2.1)}$$

where L is the diffusion length, D is the diffusion coefficient and τ is the life time of the exciton. However, duo to the short exciton lift time (generally from pico to nano seconds), the exciton diffusion length is very small [2.8]. Thus a short average distance from one point where an exciton generated to an interface is desired. Fortunately, bulk heterojunction polymer solar cell can properly solve this problem properly due to the interpenetrate network formation in the active layer.

Exciton dissociation and free carrier generation

Exciton dissociation is one of the key steps in photovoltaic devices to transfer solar energy into electrical energy. This process can be efficiently induced by the offset energy at the D/A interface. The energy level alignment requirement for

efficient charge generation is shown in Fig. 2.3. Donor material has a lower ionization potential given by HOMO level, and accepter material has a high electron affinity given by LUMO level. Thus, the offset energy is given by

$$E_{off} = E_{DH} - E_{AL}, \quad \text{(Eq. 2.2)}$$

where E_{off} is the offset energy, E_{DH} is the donor HOMO level, and E_{AL} is the accepter LUMO level. As shown in Fig. 2.3 (a), when the exciton binding energy (E_{ex}) is larger than E_{off}, the charge-transfer reactions will occur,

$$D^* + A \rightarrow D^+ + A^-, \quad \text{(Eq. 2.3)}$$

$$D + A^* \rightarrow D^+ + A^-, \quad \text{(Eq. 2.4)}$$

where D^* and A^* are donor and accepter excited states, and D^+ and A^- are hole and electron polarons in donor and accepter materials. However, when E_{ex} is smaller than E_{off}, as shown in Fig. 2.3 (b), the charge-transfer reactions will be inefficient.

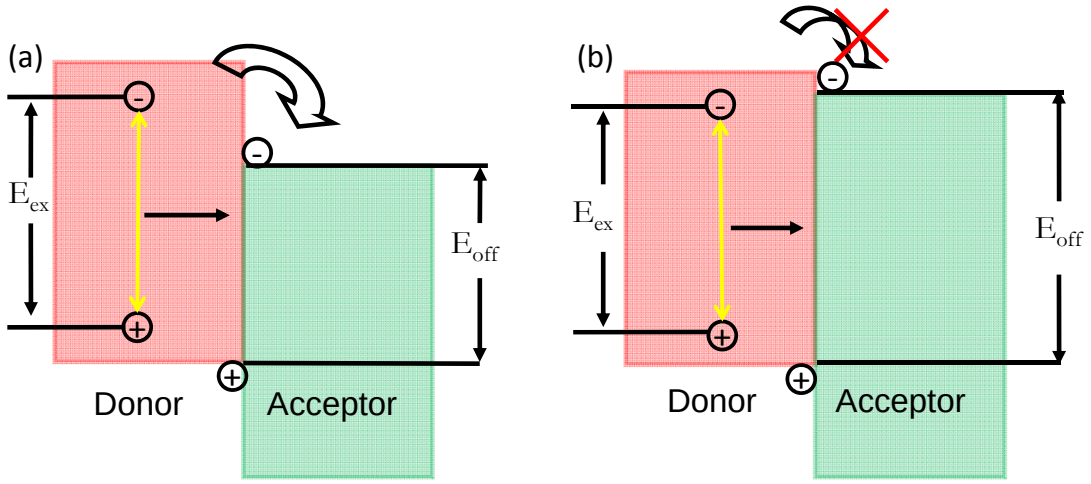

Figure 2.3 Schematic illumination of energy level alignment requirement for (a) efficient and (b) inefficient charge generation.

Free carrier transport and collection

After excitons dissociate into free electrons and holes, electrons will be transported to the anode and holes will be transported to the cathode. This phenomenon is due to the driving force from the filed created by the difference work-function of the two electrodes and the "chemical potential" driving force, thus energy level matching at interface between the electrode and active layer is very important. Ohmic contact will be formed by proper energy alignment, which favours the free carrier collection. Improper energy alignment will introduce schottky barriers at the interface, which causes free carriers accumulation in the near electrode region, resulting in electron-hole recombination and photocurrent loss. One important issue is that the free charge carrier mobility is very low in the organic material compared with that in the inorganic semiconductor material, which requires thin active layer. Fortunately, high absorption coefficient of organic semiconductor materials allows thin active layer needed for effective absorption.

2.2 Materials and experimental methods

In this work, bulk heterojunction structure is applied in our cells since it is the most promising structure due to its properties of effective exciton dissociation and effective carrier transport. In this section, a brief introduction of the materials and experimental methods used in this work will be given.

2.2.1 Materials

There are many organic materials which have been developed and applied in OSCs. Among them, the donor materials we used in this work are regioregular poly(3-hexylthiophene) (P3HT), poly[[4,8-bis[(2-ethylhexyl)oxy]benzo[1,2-b:4,5-b']dithiophene-2,6-diyl][3-fluoro-2[(2 ethylhexyl)carbonyl]thieno[3,4-b]thiophenediyl]] (PTB7) and poly[[9-(1-octylnonyl)-9H-carbazole-2,7-diyl]-2,5-thiophenediyl-2,1,3-benzothiadiazole-4,7-diyl-2,5-thiophenediyl] (PCDTBT). P3HT has reasonable hole mobility of μ_p = 0.1 to 10^{-3} $cm^2V^{-1}s^{-1}$ measured in pure P3HT film [2.9, 2.10]. Reasonable light absorption coefficient and environmental stability also make it to be the most used material. PTB7 has a relatively high hole mobility of about 4.1 × 10^{-4} $cm^2V^{-1}s^{-1}$ [2.11]. Compared with P3HT, the light absorption range has been improved. A high PCE of above 9 % based on PTB7:$PC_{71}BM$ has been achieved in inverted OSCs due to the improved short circuit current and fill factor [2.12]. Compared with P3HT, OSCs based on PCDTBT with a hole mobility of 1.5 × 10^{-4} $cm^2V^{-1}s^{-1}$ can obtain a high open circuit voltage of about 0.9 V [2.13].

For the accepter materials, the soluble fullerene phenyl-C61-butyric acid methyl ester (PCBM) was mostly used. PCBM is a special spherical electron carbon cluster with the electron mobility approximately of 10^{-3} $cm^2V^{-1}s^{-1}$ [2.14].

Regioregular P3HT was purchased from Rieke Metals. $PC_{61}BM$ and $PC_{71}BM$ were obtained from Nano-C. PTB7 and PCDTBT were acquired form 1-material. ZnO powders, titanium iso-propoxide, polyethylenimine (PEI) and poly(styrenesulfonate) sodium salt (PSS) were purchased from Sigma-Aldrich. Material chemical structures are shown in Fig. 2.4**.**

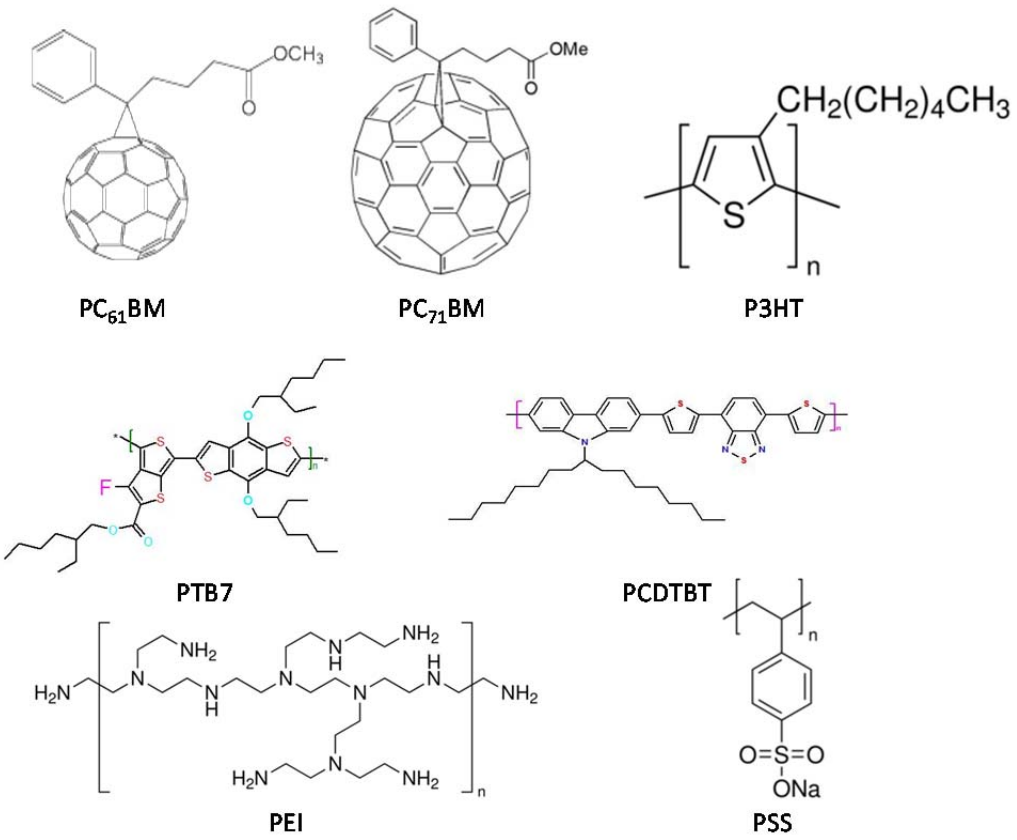

Figure 2.4 Material chemical structures.

2.2.2 Device fabrication process

There are two types of architectures in OSCs and what we used in this study is inverted architecture. Fig. 2.5 shows the layer structure and process flow for the device fabrication. Patterned ITO-coated glass substrates were cleaned by a routine solvent ultrasonic cleaning, sequentially with detergent, de-ionized water, acetone, and iso-propanol (IPA) in an ultrasonic bath for 15 minutes each. After 5 min argon plasma treatment on ITO films, an interfacial layer was deposited on top of the ITO film. Following that, an active layer was deposited on top of the interfacial layer by spin-coating a solution of the active layer blend in nitrogen (N_2) environment. The

active layers were dried for 2 hours with or without pre-annealing treatment. Finally, a MoO_3 layer (6 nm) and a Ag layer (100 nm) were deposited by using vacuum thermal evaporation. A metal shadow mask was used for the Ag deposition to define the device area of 9 mm^2.

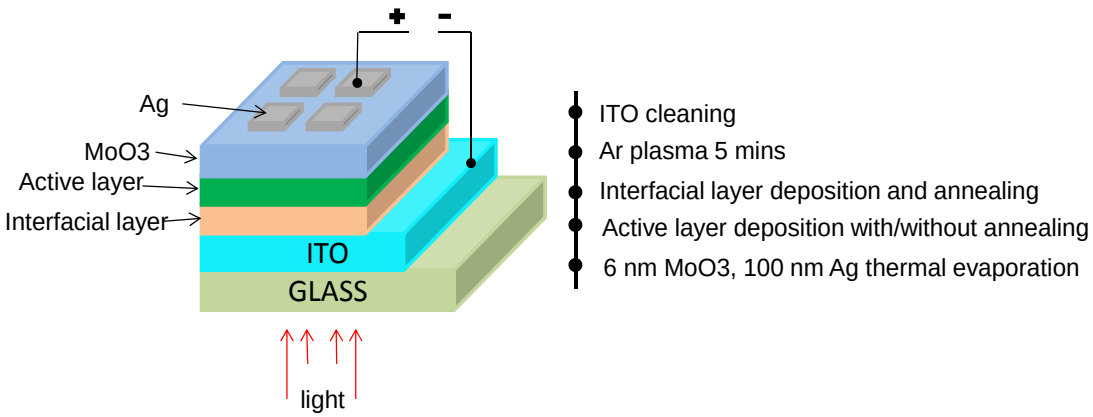

Figure 2.5 Layer structure and process flow for the device fabrication.

2.2.3 Interfacial layer preparation

There are four types of interfacial layers: (1) atomic layer deposited (ALD) ZnO and TiO_2 films; (2) solution processed ZnO and sol-gel TiO_x films; (3) polyelectrolyte PEI:PSS blend film; and (4) solution processed sol-gel TiO_x film coated with PEI:PSS blend film.

Atomic layer deposited (ALD) ZnO and TiO_2 films

For ALD deposited ZnO and TiO_2 films, the precursors used were water (H_2O) and diethylzinc (DEZ), and H_2O and titanium tetrachloride ($TiCl_4$), respectively. The pulse time for each reactant was set to 0.5 s, and nitrogen was used as a purge and

carrier gas with the flow rate of 50 sccm and the purging time was set to 30 s. Deposition temperature used for the growths could be tuned, and the layer thickness was controlled by the growth cycle number.

Solution processed ZnO and sol-gel TiO_x films

ZnO nanopowders were directly dissolved in ammonia solution (0.1 M/ml). The solution was stirred overnight to yield a homogenous, clear, and transparent solution. After the ZnO particles totally dissolved, the ZnO solution was spin-coated on top of ITO substrates at 3000 rpm for 30s and the formed ZnO films were immediately annealed at 150 °C for 10 min. Titanium iso-propoxide was directly dissolved in IPA with a ratio of 1:200. The solution was stirred overnight to yield a homogenous, clear, and transparent solution. After totally dissolved, the TiO_x solution was spin-coated on top of ITO substrates at 4000 rpm for 1min and the formed TiO_x films were immediately annealed at 150 °C for 10 min.

Polyelectrolyte PEI:PSS blend

PEI and PSS with different ratios of 1:0.1, 1:0.3, 1:0.5, 1:0.8 and 1:1 were directly dissolved in de-ionized water, and with a controlled concentration (2 mg/mL). PEI only solution (2mg/ml) was also prepared as the reference. The solution was stirred overnight to yield a homogenous, clear, and transparent solution. After the solutions were prepared, PEI:PSS layers were formed by spin-coating the solution on the top of ITO layers at 4000 rpm for 1 min and immediately annealed at 100 °C for 10 min.

Solution processed sol-gel TiO_x coated with PEI:PSS blend film

The TiO_x solution was spin-coated on top of ITO substrates at 4000 rpm for 1min and the formed TiO_x films were immediately annealed at 150 °C for 10 min. After that, PEI:PSS layers were formed by spin-coating the solution on the top of TiO_x layers at 4000 rpm for 1 min and immediately annealed at 100 °C for 10 min.

2.2.4 Active layer blend solution preparation

There are three types of active layer blend solutions used in this study: P3HT:PC_{61}BM, PTB7:PC_{71}BM and PCDTBT:PC_{71}BM. The solution of P3HT:PC_{61}BM blend with a weight ratio of 1:1 in 1, 2-dicholorobenzen (40mg/ml) was spin-coated at 500 rpm for 130 s in a N_2 filled glove box. The active layers were dried for 2 hours and then pre-annealed at 140°C for 10 minutes. The P3HT:PC_{61}BM active layer thickness is about 180 nm measured by surface step profiler. The solution of PTB7:PC_{71}BM blend with a weight ratio of 1:1.5 in 1, 2-dicholorobenzen (25mg/ml) (with 0.3% diiodooctane) was spin-coated at 1000 rpm for 100 s and the active layers were dried for 2 hours without pre-annealing. The PTB7:PC_{71}BM active layer thickness is about 70 nm. The solution of PCDTBT:PC_{71}BM blend with a weight ratio of 1:4 in cholorobenzen:1, 2-dicholorobenzen (1:3) (7mg/ml) was spin-coated at 1000 rpm for 100 s and the active layers were dried for 2 hours with pre-annealed at 70°C for 10 minutes. The PCDTBT:PC_{71}BM active layer thickness is about 70 nm.

2.3 Characterization methods

Current density – voltage characterization in OSCs

The most important and meaningful characterization of OSCs is the current density – voltage (J – V) measurement in the dark and under illumination since it determines the device performance. The measurement is done by a sweeping voltage and current density is measured for every voltage applied.

The J – V characteristics of the devices were measured using a Keithley 2400 parameter analyzer in the dark and under a simulated light (AM 1.5G) with an intensity of 100 mW/cm^2. The light source was calibrated with a standard silicon photodiode.

Fig. 2.6 (a) shows an example of J – V curve of ITO/TiO_2/P3HT:PCBM/MoO_3/Ag device measured in the dark, and the obvious rectifying characteristic can be observed resulting from the different metal/organic interface injection barriers at the forward and reverse biases.

Fig. 2.6 (b) shows a typical bulk heterojunction solar cell J – V curve of ITO/TiO_2/P3HT:PCBM/MoO_3/Ag device measured under illumination. Several parameters are well defined in the curve:

1) Open circuit voltage, V_{oc}, is the maximum photovoltage that can be obtained in the cell when the current flow in the external circuit is zero.
2) Short circuit current density, J_{sc}, is the current density obtained when the applied voltage is zero.
3) Fill factor, FF, is defined as the ratio of maximum power (blue rectangle in Fig. 2.5) to the product of V_{oc} and J_{sc}.

$$FF = \frac{(JV)max}{V_{oc}J_{sc}} . \quad \text{(Eq. 2.5)}$$

4) Power conversion efficiency (PCE), η, is the ultimate measure of the device efficiency in converting photons to electrons, defined as

$$\eta = \frac{V_{oc}J_{sc}FF}{P_{in}} = \frac{V_{max}J_{max}}{P_{in}} , \quad \text{(Eq. 2.6)}$$

where P_{in} is the incident light power density. Generally, the solar cell device is tested with a solar simulator, where P_{in} is standardized at 1000 W m^{-2} or 100 mW cm^{-2} matching the solar spectral irradiance on the earth's surface at an angle of 48.2° to the zenith, called Air Mass (AM) 1.5 spectrum.

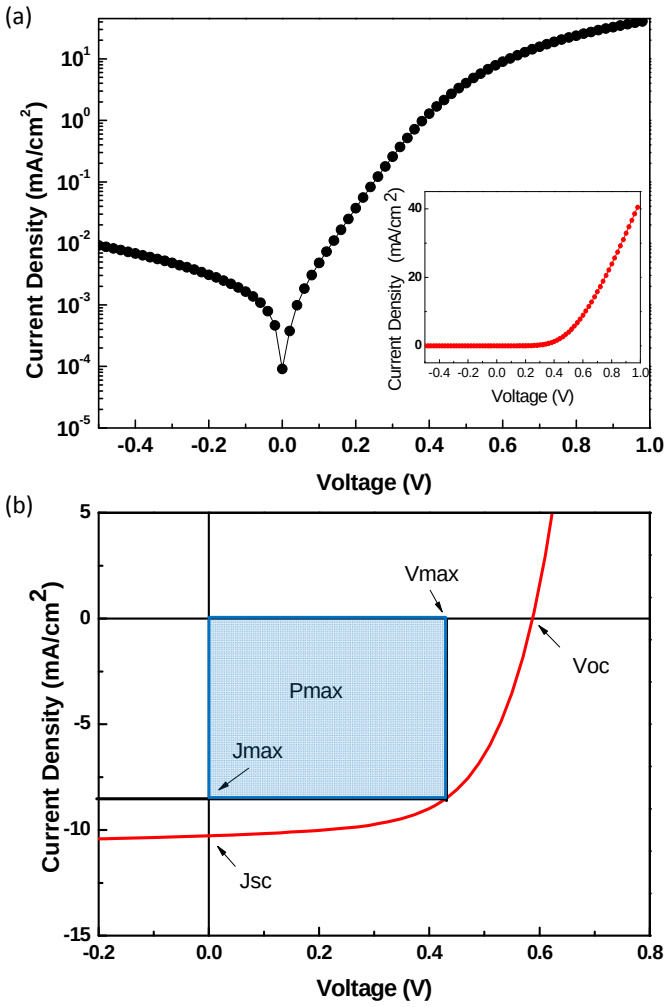

Figure 2.6 A typical $J - V$ curve of ITO/TiO_2/P3HT:PCBM/MoO_3/Ag device (a) in the dark and under illumination (b) for OSCs.

Incident photon-to-current efficiency (IPCE)

IPCE of the devices was measured with a 300 w Xenon Lamp (Oriel 6258) as the light source and a Cornerstone 260 Oriel 74125 monochromator with a resolution of 10 nm. The light intensity was calibrated with a NREL-recommended silicon detector (Oriel 71030NS), and the short circuit current density was determined with an Oriel 70310 optical power meter.

Morphology and thickness characterization

Surface morphology and roughness of the film were observed by field emission scanning electron spectroscopy (FESEM) (JEOL JSM6700F) and tapping-mode Atomic Force Microscopy (TM-AFM) which was performed on a Bruker ICON-PKG atomic force microscopy (AFM). The film thickness of ALD deposited ZnO and TiO_2 on silicon substrates were measured by Ellipsometry.

Optical Spectroscopy

The transmittance and absorptance spectra of films were characterized using an UV-3600 Shimadzu UV-VIS-NIR Spectrophotometer. The reflectance spectra of films were characterized using a UV-3101PC Shimadzu UV-VIS-NIR scanning spectrophotometer.

Photoemission spectroscopy

Physical properties of films were characterized by 2D x-ray diffraction (XRD) (Bruker-AXS D8-GADDS), x-ray photoelectron spectroscopy (XPS) (VG ESCALAB-220i XL) and ultraviolet photoelectron spectroscopy (UPS) (VG ESCALAB-220i XL). The photoluminescence (PL) spectra of films were excited with a He-Cd laser (λ = 325 nm) using an LS 55 fluorescence spectrometer (Perkin Elmer).

Solution PH

The pH values of the PEI:PSS solutions were tested by the AB15 pH meter (Accumet Basic) at the room temperature of 25 °C.

2.4 Equivalent circuit parameter extraction

In order to estimate solar cell performance to simulate, design, fabricate, and quickly control solar cells, an accurate knowledge of their parameters from experimental data is important. The electrical characteristic of a solar cell can be described by the equivalent circuit of the single-diode model, the two-diode model [2.15] and the three-diode model [2.16]. The single-diode model has the simplest form, can well describe the characteristics of various solar devices, and satisfy most of the applications, so the single-diode model is widely used to characterize OSCs [2.17 – 2.19].

The methods to determine the unknown parameters of saturation current I_0, photocurrent I_{ph} , series resistance R_s, shunt resistance R_{sh} and ideality factor n have

been the subject of many studies [2.19 – 2.24]. Some methods use the measurements of illuminated current – density (I –V) characteristics under different illumination levels [2.20] and some utilize dark and illuminated measurements [2.21, 2.22]. However, it should be noticed that the device parameters are widely influenced by the different illumination levels [2.22]. Therefore, it is very important to estimate all the parameters from a single I – V curve measured under the condition of one constant illumination level.

Recently, Ishibashi *et al.* introduced one method to extract all the parameters of a solar cell under one constant illumination level [2.23]. However, their method needs to calculate the differential values of dV / dI from the experimental data, which requires a very smooth I −V curve. Thus, the polynomial approximation or other method to smooth the experimental curve is inevitable. Furthermore, in their method, only a part of the experimental data can be used to extract the parameters because the differential dV / dI will have a very large error when I is close to the short circuit current (I_{sc}). In one previous work from Jain *et al.*, Lambert W function has been used to study the properties of solar cells [2.24]. However, their study is validated only on simulated I −V characteristics instead of the parameter extraction from the experimental data. Another work from Ortiz-Conde *et al.* proposed an efficient method to extract the solar cell parameters from the I −V characteristics based on the Lambert W function [2.19]. Because the explicit analytical expressions directly derived from Eq. 2.7 still remain unsuitable for the purpose of extracting the model parameters, they first calculated the Co-content (CC) function from the exact explicit analytical expressions and then extracted the device parameters by fitting. However, the CC is still a function of I and V, and thus the fitting process is a bi-dimensional fitting progress.

In this section, a simple and efficient method for the extraction of all parameters of a solar cell from a single $I - V$ curve under the constant illumination level is proposed. With the help of the Lambert W function, the explicit analytical expression for I is obtained. By reducing the number of parameters, the expression for I only depends on the ideality factor n, the series resistance R_s, and the shunt resistance R_{sh}. This analytical expression is directly used to fit the experimental data and extract the device parameters.

To describe the device $I - V$ characteristics, the equivalent circuit as shown in Fig. 2.7 is usually used.

Based on the equivalent circuit, the relation between I and V can be given by

$$I = I_0\left(e^{\frac{q(V-R_sI)}{nk_BT}} - 1\right) + \frac{V-R_sI}{R_{sh}} - I_{ph}, \qquad \text{(Eq. 2.7)}$$

where I_0, I_{ph}, R_s, R_{sh}, q, n, k_B, and T are the saturation current, the photocurrent, the series resistance, the shunt resistance, the electron charge, the ideality factor, the Boltzmann constant, and the temperature, respectively.

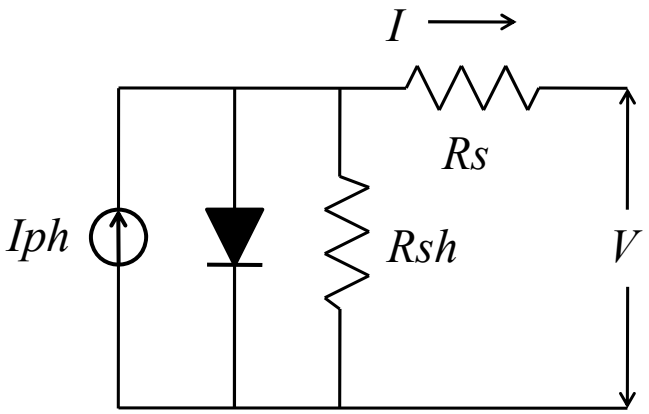

Figure 2.7 The equivalent circuit of a solar cell based on single-diode model.

Eq. 2.7 gives the most popular description of $I - V$ characteristics of a solar cell under a given illumination level. It is an implicit equation and cannot be solved analytically. But with the help of the Lambert W function, the solution can be given:

$$I = \frac{V}{R_s} - \frac{R_{sh}(R_S I_{ph} + R_s I_0 + V)}{R_s(R_{sh} + R_s)} + \frac{nk_BT}{qR_s} lambertw[\frac{qR_s I_0 R_{sh}}{(R_{sh} + R_s)nk_BT} \exp(\frac{qR_{sh}((R_S I_{ph} + R_s I_0 + V))}{(R_{sh} + R_s)nk_BT})],$$

(Eq. 2.8)

where *lambertw* is the Lambert W function which can be easily solved numerically. The reason that we can derive Eq. 2.8 is that there is only one exponential term in Eq. 2.7. If there are two or more exponential terms in the equation, it will be very difficult to derive the expression for I based on the Lambert W function. This is another very important reason for choosing the single-diode model in this work. Eq. 2.8 has an analytical form and it is very convenient to be used in computer program to reproduce the $I - V$ curves of a solar cell when knowing all the parameters. However, this expression is still unsuitable for the purpose of extracting the device parameters [2.19]. When it is used in the curve fitting to extract the device parameters, very large errors can be introduced. This is mainly caused by the very large value difference between I_0 and I_{ph}. Although both I_0 and I_{ph} are current, the difference between their values is usually larger than six orders. Thus Eq. 2.8 must be dealt before it is used for the device parameter extraction.

By applying the short circuit ($V = 0$, $I = I_{sc}$) and open circuit ($V = V_{oc}$, $I = 0$) conditions, from Eq. 2.7, it gives

$$I = \frac{V}{R_s} - \frac{R_{sh}\left(R_S\frac{I_{sc}+\frac{R_sI_{sc}-V_{oc}}{R_{sh}}}{1-\exp\left(\frac{q(R_sI_{sc}-V_{oc})}{nk_BT}\right)}+\frac{V_{oc}}{R_{sh}}+V\right)}{R_s(R_{sh}+R_s)} + \frac{nk_BT}{qR_s}lambertw[\frac{qR_s}{nk_BT}\frac{\left(I_{sc}-\frac{V_{oc}}{R_{sh}+R_s}\right)\exp\left(-\frac{qV_{oc}}{nk_BT}\right)}{1-\exp\left(\frac{q(R_sI_{sc}-V_{oc})}{nk_BT}\right)}\exp\left(\frac{qR_{sh}\left(R_S\frac{I_{sc}+\frac{R_sI_{sc}-V_{oc}}{R_{sh}}}{1-\exp\left(\frac{q(R_sI_{sc}-V_{oc})}{nk_BT}\right)}+\frac{V_{oc}}{R_{sh}}+V\right)}{(R_{sh}+R_s)nk_BT}\right).$$

(Eq. 2.9)

Now, the current I is only related to three unknown variables, n, R_s, and R_{sh} since all other values can be obtained from the experimental data. This makes Eq. 2.9 suitable to be used in parameter extraction by the numerical fitting method. In the derivation of Eq. 2.9, no assumption or approximation has been used. Therefore, Eq. 2.9 is the accurate expression of Eq. 2.7. However, this expression seems a little complicated. It can be greatly simplified, if we make the assumption

$$\Delta = \exp\left(\frac{q(R_sI_{sc}-V_{oc})}{nk_BT}\right) \ll 1 \qquad \text{(Eq. 2.10)}$$

Based on this assumption, Eq. 2.13 can be reduced to

$$I = \frac{V}{R_s} - I_{sc} - \frac{R_{sh}V}{R_s(R_{sh}+R_s)} + \frac{nk_BT}{qR_s}lambertw[\frac{qR_s}{nk_BT}\left(I_{sc}-\frac{V_{oc}}{R_{sh}+R_s}\right)\exp\left(-\frac{qV_{oc}}{nk_BT}\right)\exp\frac{q}{nk_BT}(R_sI_{sc}+\frac{R_{sh}V}{R_s(R_{sh}+R_s)}).$$

(Eq. 2.11)

Now, Eq. 2.11 is much simpler than Eq. 2.9. However, it requires that the assumption 2.10 is valid. Fortunately, this assumption is generally valid for various solar cells [2.25].

Both Eq. 2.9 and Eq. 2.11 are suitable to be used to extract the device parameters of n, R_s and R_{sh} by employing the mature least square method. Since there is only one independent variable V in the right side of Eq. 2.11, the fitting process is only one dimensional and thus the whole parameter extracting process becomes simple. For example, in a Matlab environment, only a few lines of code are required. After n, R_s and R_{sh} are extracted, I_0 and I_{ph} can be calculated.

The initial values of n, R_s and R_{sh} are given as following.

From Eq. 2.7, dV/dI is expressed as

$$\frac{dV}{dI} = \frac{nk_BT/q}{I_{ph}+I_0-I-(V-R_sI-nk_BT/q)/R_{sh}} + R_s. \quad \text{(Eq. 2.12)}$$

Under the short circuit condition,

$$\frac{dV}{dI}|_{I=I_{sc},V=0} = R_{sh} + R_s \sim R_{sh}, \quad \text{(Eq. 2.13)}$$

and around the open circuit condition ($I = 0$ and $V = V_{oc}$),

$$\frac{dV}{dI} = \frac{nk_BT/q}{I_{sc}+I-\frac{V}{R_{sh}}+\frac{nk_BT}{qR_{sh}}+\frac{R_S(I_{SC}+I)}{R_{sh}}} + R_S \approx \frac{k_BT/q}{I_{sc}+I-\frac{V}{R_{sh}}} + R_S. \quad \text{(Eq. 2.14)}$$

The initial values of n and R_s are derived by the y-intercept and the slope of the plot of dV/dI as a function of $(I_{sc} + I - \frac{V}{R_{sh}})^{-1} k_BT/q$. In the derivation of Eq. 2.13 and Eq. 2.14, the assumption $R_{sh} \gg R_s$ has been used, which is generally a good approximation to set the initial values.

Fig. 2.8 shows one example of the experimental $J - V$ curve and fitting curves. It can be seen that they are in good consistent.

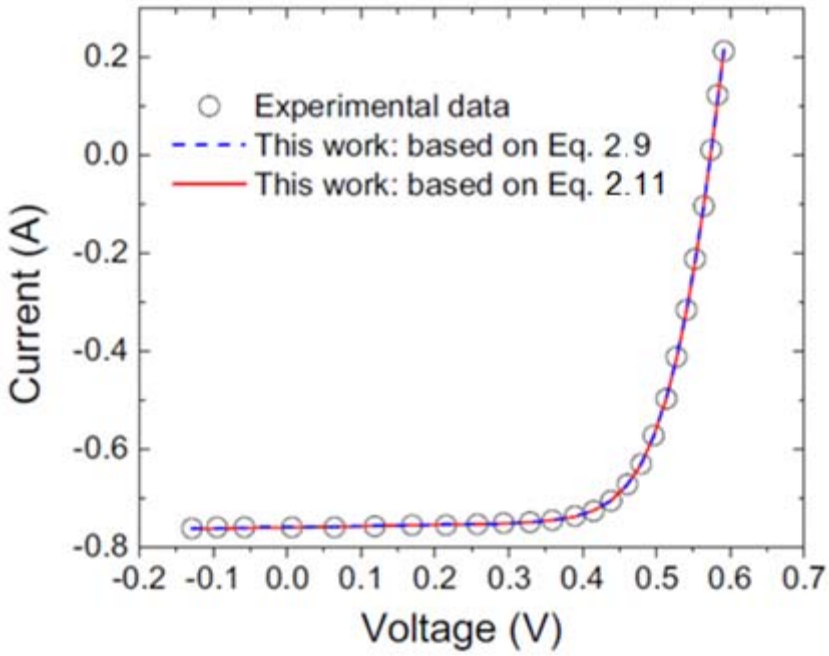

Figure 2.8 One example of the experimental $J - V$ curve and fitting curves.

References

[2.1] S. E. Shaheen, R. Radspinner, N. Peyghambarian and G. E. Jabbour, Applied Physics Letters 79, 2996 – 2998 (2001).

[2.2] P. W. M. Blom, V. D. Mihailetchi, L. J. A. Koster and D. E. Markov, Advanced Materials 19, 1551 – 1566 (2007).

[2.3] Y. S. Cho and R. R. Franklin, Transactions on Electrical and Electronic Materials 13, 237 – 240 (2012).

[2.4] http://en.wikipedia.org/wiki/Relative_permitivity

[2.5] B. A. Gregg and M. Hanna, Journal of Applied Physics 93, 3605 – 3614 (2003).

[2.6] T. Bak, J. Nowotny, M. Rekas and C. C. Sorrell, International Journal of Hydrogen Energy 27, 991 – 1022 (2002).

[2.7] S. Günes, H. Heugenauer and N. S. Sariciftci, Chemical Review 107, 1324 – 1338 (2007).

[2.8] N. S. Sariciftci, L. Smilowitz, A. J. Heeger and F. Wudl, Science 258, 1474 - 1476 (1992).

[2.9] H. Sirringhaus, P. J. Brown, R. H. Friend, M. M. Nielsen, K. Bechgaard, B. M. W. Langeveld-Voss, A. J. H. Spiering, R. A. J. Janssen, E. W. Meijer, P. Herwig and D. M. de Leeuw, Nature 401, 685 – 688 (1999).

[2.10] A. Ullmann, J. Ficker, W. Fix, H. Rost, I. McCulloch, M. Giles, G. E. ed. Jabbour and N. S. Sariciftci, Materials Research Society Symposium Proceeding 665 (2002).

[2.11] B. Carsten, J. M. Szarko, H. J. Son, W. Wang, L. Lu, F. He, B. S. Rolczynski, S. J. Lou, L. X. Chen and L. Yu, Journal of the American Chemistry Society 133, 20468 – 20475 (2011).

[2.12] Z. He, C. Zhong, S. Su, M. Xu, H. Wu and Y. Cao, Nature Photonics 6, 591 – 595 (2012).

[2.13] T.-Y.Chu, S. Alem, S.-W. Tsang, S.-C. Tse, S. Wakim, J. Lu, G. Dennler, D. Waller, R. Gaudiana and Y. Tao, Applied Physics Letters 98, 253301 (2011).

[2.14] V. D. Mihailetchi, J. K. J. van Duren, P. W. M. Blom, J. C. Hummelen, R. A. J. Janssen, J. M. Kroon, M. T. Rispens, W. J. H. Verhees and M. M. Wienk, Advanced Functional Materials 13, 43 – 46 (2003).

[2.15] G. L. Araujo, E. Sanchez and M. Marti, Solar Cells 5, 199 – 204 (1982).

[2.16] B. Mazhari, Solar Energy Materials and Solar Cells 90, 1021 – 1033 (2006).

[2.17] B. P. Rand, D. P. Burk, and S. R. Forrest, Physical Review B: Condensed Matter Materials Physics 75, 115327 (2007).

[2.18] K. Nishioka, N. Sakitani, K. Kurobe, Y. Yamamoto, , Y. Ishikawa, Y. Uraoka, T. Fuyuki, Journal of Applied Physics 42, 7175 – 7179 (2003).

[2.19] A. Ortiz-Conde, F. J. Garc_a Sanchez and J. Muci, Solar Energy Materials and Solar Cells 90, 352 – 361 (2006).

[2.20] D. Pysch, A. Mette, and S.W. Glunz, Solar Energy Materials and Solar Cells 91, 1698 – 1706 (2007).

[2.21] R. Hussein, D. Borchert, G. Grabosch, and W. R. Fahrner, Solar Energy Materials and Solar Cells 69, 123 – 129 (2001).

[2.22] P. Mialhe, A. Khoury, and J. P. Charles, Physica Status Solidi A 83, 403 – 409 (1984).

[2.23] K. Ishibashi, Y. Kimura, and M. Niwano, Journal of Applied Physics 103, p094507 (2008).

[2.24] A. Jain and A. Kapoor, Solar Energy Materials and Solar Cells 86, 197 – 205 (2005).

[2.25] K. Ishibashi, Y. Kimura, and M. Niwano, Journal of Applied Physics 103, p094507 (2008).

Chapter 3

ALD-Grown Metal Oxide Interlayers Combined with Patterned ITO Cathode in Inverted OSCs

3.1 Introduction

Due to advantages of capability of low-cost and large area fabrication process, and light weight and mechanical flexibility using plastic substrates, organic photovoltaics (OPVs) have attracted much attention in recent years [3.1-3.3]. One key challenge in making efficient inverted OSCs lies in the electron selective buffer layer: it should work as a high conductive path for efficient electron extraction and exhibit good hole blocking capability. N-type metal oxides, zinc oxide (ZnO) and titanium oxide (TiO_x), have been considered as good candidates to work as electron selective layer due to their acceptable carrier mobility and high transparency in the visible wavelength range.

The synthesis of ZnO and TiO_x has been widely investigated [3.4-3.13] and a number of works have been carried out in inverted OSCs using ZnO or TiO_2 film as an electron selective layer deposited by solution processing sol-gel [3.8-3.10], sputtering [3.11], spray pyrolysis [3.12], or atomic layer deposition (ALD) [3.13]. Spray pyrolysis usually employs a high temperature (>250 °C) process for titanium oxide precursor decomposition, which may not be suitable for low-cost plastic substrates. Solution processing sol-gel methods have demonstrated promising low

temperature and roll-to-roll fabrication potential for metal oxide thin film for OSCs. However, it has its limitations in precisely controlling the thickness and uniformity of the ultra-thin metal oxide film over a large area and its poor conformal coating capability on nanostructured surfaces [3.14-3.16]. Compared with other synthesis methods, ALD technique has been developed extensively in many fields, such as batteries and capacitors [3.17], sensors [3.18], separactive membranes [3.19], photovoltaics [3.20, 3.21] and photocatalysis [3.22]. This method has several advantages over the other depositing methods. It can control the deposition thickness in atomic scale by the number of deposited cycles. Besides, it could provide highly repeatable, uniform, dense and highly conformal films on 2D and 3D structured surfaces [3.23]. However, there are very few reports on inverted OSCs using ALD-processed TiO_2 film as the electron selective layer. Kang et al. reported an efficient inverted OSC fabricated by using nanocrystalline TiO_2 film deposited by ALD at 220 °C [3.13]. However, this deposition temperature is too high for commonly used plastic substrates such as polyethylene terephthalate (PET) or polyethylene naphthalate (PEN). In a recent study of using TiO_2/ZnO selection layer for inverted OSC, ALD-processed TiO_2 is only used as a surface modification on ZnO film because of its high resistance.

Meanwhile, even though the power conversion efficiency (PCE) for bulk heterojunction solar cell has reached to above 9 % [3.24], further improvement of PCE is still the main focus under intensive studies. Two strategies to improve OPV device performance are generally used to date, including tuning the optical and electronic properties of the blend components [3.25-3.27] and design of advanced device structures [3.28-3.34]. Tuning the optical and electronic properties of the blend component can increase the open-circuit voltage (V_{oc}) of the cell by engineering

energy levels [3.25-3.26], and the short-circuit current density (J_{sc}) by engineering bandgap [3.27]. The design and adoption of advanced device structures are to improve the light absorption using light trapping or optical-field arrangement [3.29-3.34], and decrease the recombination loss by interface or morphology engineering techniques [3.35, 3.36].

The introduction of nanostructured patterns in OPV cells has been reported to be an effective method to enhance the light absorption, improve the excitons separations, and facilitate the charge carrier transport. Nano-patterned indium-tin-oxide (ITO) electrodes used in OPV devices have been reported by several research groups, and the methods to fabricate nano-patterns on ITO electrode include nanoimprint lithography [3.29, 3.30], laser interference lithography (LIL) [3.31], colloidal lithography [3.32] with chemical vapor etching [3.33] or depositing additional ITO layer [3.34]. Among these techniques, LIL is the preferable method for patterning the ITO substrates, which is mold-less, mask-less and room temperature-operated method [3.37]. While for the nanoimprinting technique, high-degree ordered molds need to be designed and fabricated, and generally, it is difficult to generate textures on hard surfaces, such as ITO and metal oxide buffer layers. For the normal lithography, masks need to be designed and fabricated. For the colloidal lithography, the only shape can be achieved is honeycomb-like pattern.

Despite some works have been reported using nano-patterned ITO electrode for OPV device fabrication, a poly(3,4-ethyl-enedioxithiophene): poly(styrenesulfonate) (PEDOT:PSS) layer is usually deposited on top of the ITO pattern by spin-coating before the polymer active layer deposition [3.29-3.31]. The solution deposited PEDOT layer usually flattens the grooves, degrading the benefits of the patterns on the active layer. Moreover, the PEDOT interfacial layer on the ITO

pattern may cause an uneven thickness (thicker in the grooves and thinner on the protrusions), which is unfavorable to the cell performance since OPV devices are usually sensitive to the thickness of the interfacial layer.

To address the above issue, inverted OPV devices based on nano-patterned ITO electrodes are investigated. The ITO electrode was patterned by using LIL method. A thin film of metal oxide (ZnO or TiO_2) which is used as an electron selective layer was conformably coated on the patterned ITO surfaces by ALD. By using ALD coating, it is expected that the ITO patterns will be maintained upon adding the metal oxide layer, thus avoiding the "flattening effect" which usually happens when spin coating PEDOT on the ITO patterns. We found that the device performance especially the photocurrent has been significantly increased by using the patterned ITO electrodes combined with ALD deposited metal oxide interlayer for the cells. The performance improvement is believed due to the enhanced charge collections and light absorption arising from the light trapping and also morphology improvement in the active layer.

3.2 ALD deposited TiO_2 film as electron selective layer on flat ITO cathode

In this section, the effects of the deposition temperature and film thickness of ALD-grown TiO_2 film on inverted OSC device performance are investigated. The S-shape problem (light soaking) occurred during the device measurement has also been studied.

Fig. 3.1 illustrates the schematic device structure of the inverted OSCs. The precursors used for TiO_2 film deposition were water (H_2O) and titanium tetrachloride

($TiCl_4$). The pulse time for each reactant was set to 0.5 s, and nitrogen was used as a purge and carrier gas with the flow rate of 50 sccm and the purging time was set to 30 s. The device fabrication process was the same as described in Chapter 2.

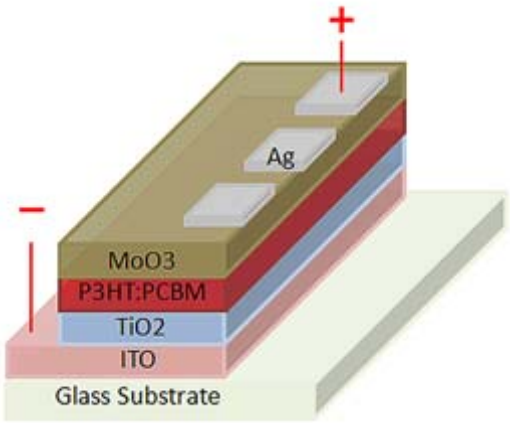

Figure 3.1 Schematic device structure of the inverted organic solar cell.

Fig. 3.2 shows the x-ray diffraction (XRD) patterns of TiO_2 thin films deposited by ALD at 170 ºC and 250 ºC on Si wafer substrates. It can be seen that the film deposited at 250 ºC clearly shows the characteristic (101) and (200) diffraction peaks of anatase TiO_2 crystalline phase, while no diffraction peaks originated from crystalline TiO_2 are observed from the film deposited at 170 ºC, indicating that the TiO_2 film deposited by ALD at 170 ºC or below is amorphous in nature and the Ti/O ratio calculated from the x-ray photoelectron spectroscopy (XPS) measurement as shown in Fig. 3.3 is about 1:2 for all the samples.

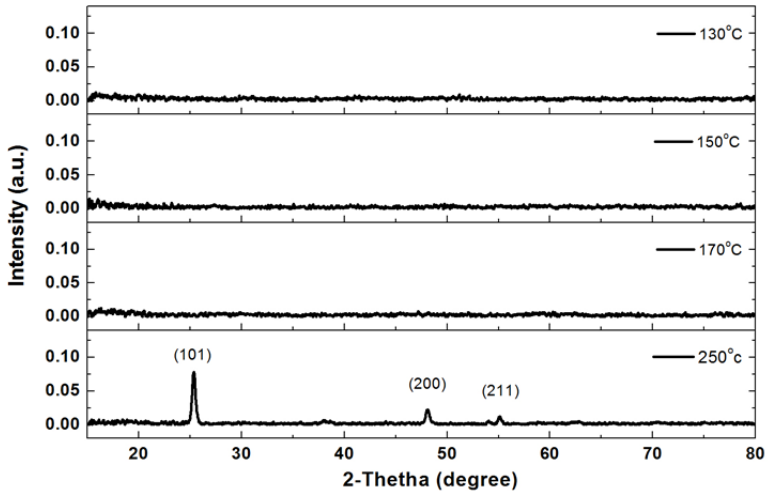

Figure 3.2 XRD patterns of TiO_2 films grown by ALD at 130 ºC, 150 ºC, 170 ºC and 250 ºC, respectively.

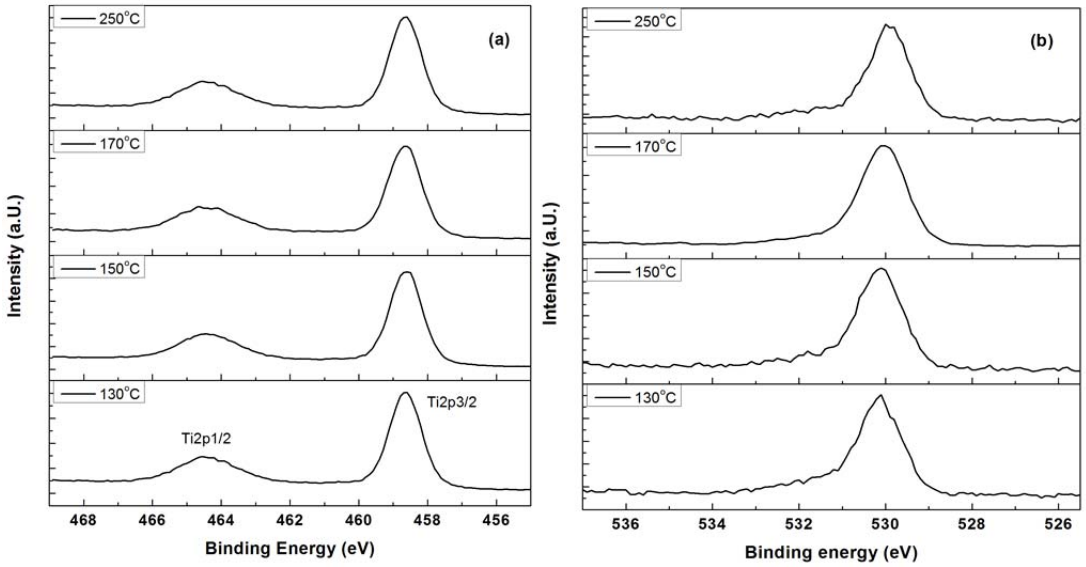

Figure 3.3 XPS spectra of (a) Ti2p and (b) O1s scans of TiO_2 films grown by ALD at temperature of 130 °C, 150 °C, 170 °C and 250 °C, respectively.

Film thickness effects on the device performance

Inverted cells using TiO_2 films with different thicknesses produced on ITO by ALD at 170 ºC were fabricated. It was found that the current density - voltage ($J - V$) curves measured for all these cells as fabricated show a pronounced S-shape and the

S-shape can be removed after a short time (typically 5 – 10 min) light soaking (under illumination, AM1.5G, 100 mW/cm^2). Fig. 3.4 shows one example of the $J - V$ curves measured for a cell as fabricated and after light soaking and also the dark $J - V$ performances. Table 3.1 summarizes the values of photovoltaic performance parameters measured as fabricated and after light soaking of the cells with different TiO_2 thicknesses from 10, 12, 15, 17 to 20 nm. From the data of measurements after light soaking, it can be seen that with the increase of the TiO_2 film thickness, the open circuit voltage (V_{oc}), short circuit current density (J_{sc}), fill factor (FF) and PCE all increase first and reach to their maximum values (V_{oc}=0.54V, J_{sc}=10.10 mA/cm^2, FF=0.60 and PCE=3.31%) at 15 nm thickness, and then decrease with further increasing the TiO_2 thickness. The poorer cell performance at thinner (10-12 nm) and thicker (17-20 nm) TiO_2 thickness is mostly because a relatively thinner layer of TiO_2 increases the hole leakage through the TiO_2 layer leading to an increased recombination of electrons and holes and hence a reduction on V_{oc}, FF and J_{sc}; while a relatively thicker amorphous TiO_2 layer increases the resistance for electron transport and causes the electrons more difficult to be collected at the cathode, and hence a reduction in the FF and J_{sc}. The similar trend on TiO_2 thicknesses was also observed in the performance data without light soaking (measurements as fabricated). Meanwhile, comparing measurements as fabricated with those after light soaking, the cell performance was significantly increased after light soaking due to the largely decreased series resistance which also can be seen from Fig. 3.4 (b), the dark $J - V$ curves. The series resistances (R_s) of the devices with light soaking decreased at least tens of times compared with those of the devices without light soaking for all the devices with different TiO_2 thicknesses, which causes both J_{sc} and FF increased. Taking the performance of the device with 15 nm thick TiO_2 film as an example, after

light soaking, the R_s decreases from 399 Ω/cm^2 to 5.58 Ω/cm^2, the J_{sc} increases form 9.35 mA/cm^2 to 10.16 mA/cm^2 and the FF increases from 0.26 to 0.60, which make the PCE increased by 149%, from 1.33% to 3.31%.

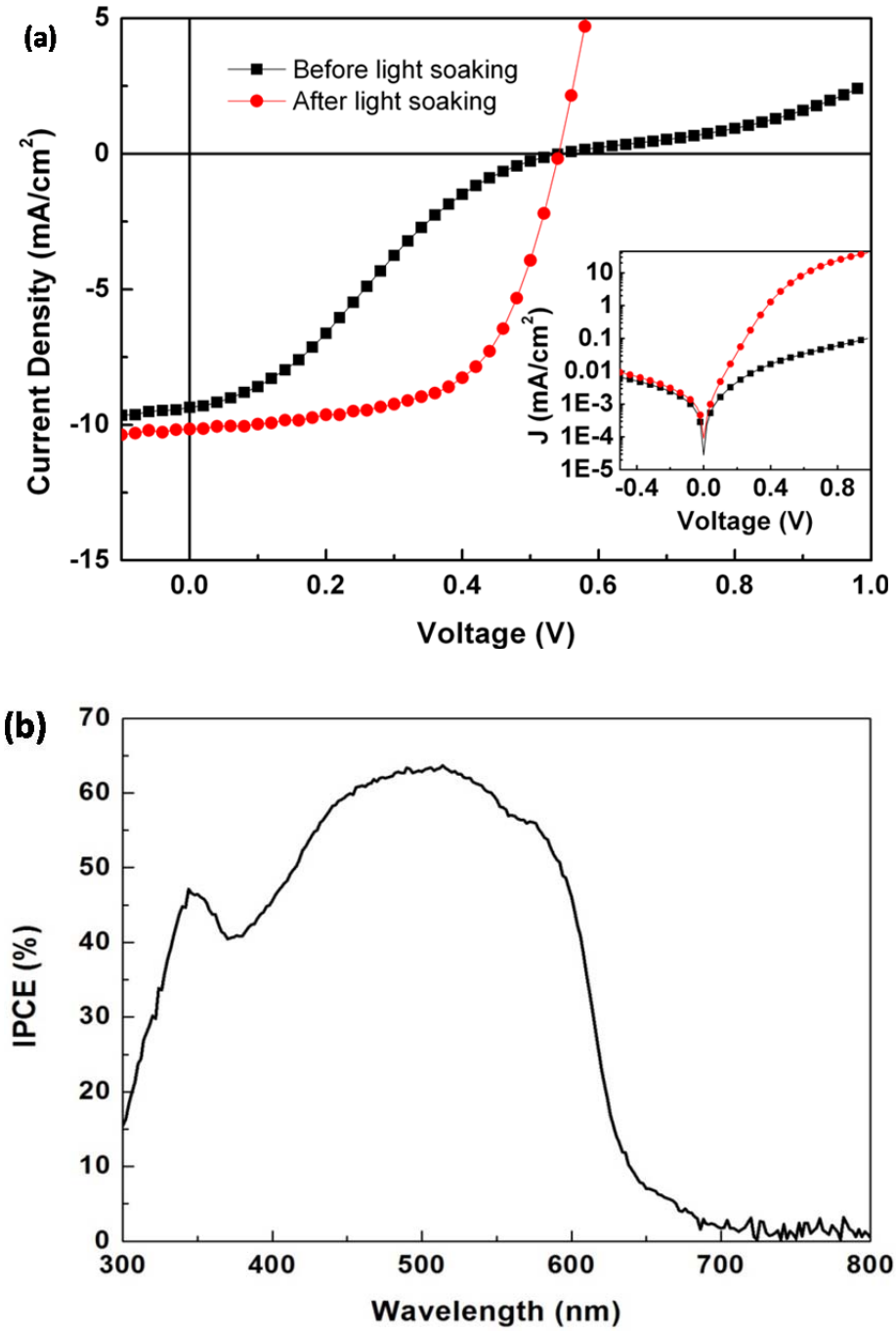

Figure 3.4 (a) $J-V$ curves measured under illumination of a cell before and after light soaking (Inset: the dark $J-V$ curves before (black squares) and after (red circles) light soaking); (b) incident photon-to-electron conversion efficiency (IPCE) for the cell with 15 nm TiO_2 layer deposited at 170 ºC.

Table 3.1 Values of photovoltaic performance parameters of inverted OSCs with different thickness TiO_2 layers grown at 170 ºC by ALD process (under simulated illumination of 100 mW/cm^2 AM 1.5G). Devices were measured as-fabricated and after light soaking (5 min simulated illumination). The device has the best performance when the TiO_2 layer thickness is 15 nm.

Thickness (nm)	J_{sc} (mA/cm^2)	V_{oc} (V)	FF	η (%)	R_s (Ω/cm^2)	R_{sh} (Ω/cm^2)	*Remark*
10	7.08	0.46	0.20	0.65	99	120	As-fabricated
	7.59	0.49	0.44	1.63	7.68	177	After light soaking
12	8.29	0.49	0.19	0.75	904	102	As-fabricated
	8.91	0.53	0.58	2.71	9.1	398	After light soaking
15	9.35	0.54	0.26	1.33	399	418	As-fabricated
	10.16	0.54	0.60	3.31	5.58	310	After light soaking
17	8.52	0.53	0.19	0.88	461	89.1	As-fabricated
	9.42	0.53	0.56	2.83	8.4	338	After light soaking
20	4.82	0.51	0.19	0.27	138	45.2	As-fabricated
	8.60	0.53	0.53	2.43	5.8	376	After light soaking

ALD deposition temperature effects on the device performance

The effect of deposition temperature of TiO_2 has also been investigated. Inverted solar cells with 15 nm thick TiO_2 layer deposited by ALD at different temperatures (130 ºC, 150 ºC, 170 ºC and 250 ºC) were fabricated, and the values of photovoltaic performance parameters of these cells are presented in Table 3.2, where the measurements were also done as fabricated and after light soaking. From the XRD pattern shown in Fig. 3.2, it can be seen that the TiO_2 film is amorphous in nature when the deposition temperature is 170 ºC or below, and the film becomes poly-crystal when the temperature is 250 ºC. It can be found that when the TiO_2 film is in amorphous phase, with the increase of the TiO_2 deposition temperature from 130 to

170 ºC, the V_{oc} and FF are nearly the same, and only J_{sc} increases and reaches a maximum value of 10.16 mA/cm^2 at 170 ºC. The considerable change solely in J_{sc} is usually arisen from the active layer with changes in morphology or optical coupling. This is possibly because the TiO_2 layers fabricated at different temperatures have different surface and optical properties, which usually affect the morphology of active layer [3.38]. Fig. 3.5 shows the surface scanning electron microscopy (SEM) images and transmittance of these TiO_2 films with different deposition temperatures. The SEM images show that the roughness of TiO_2 films increases with the deposition temperature due to the growing of the grain size on the film, which becomes pronounced in the TiO_2 film deposited at 250 ºC. From Fig. 3.5(e), it shows that the transmittance profiles are different in these TiO_2 films; with the 170 ºC deposited film has the highest transmittance in the wavelength range 300 - 700 nm.

Table 3.2 Values of photovoltaic performance parameters of inverted OSCs with 15 nm thick TiO_2 layer grown at different temperatures by ALD process (under simulated illumination of 100 mW/cm^2 AM 1.5G). Devices were measured as-fabricated and after light soaking (5 min simulated illumination). The device has the best performance when the deposition temperature is 170 ºC.

Deposition Temperature	J_{sc} (mA/cm^2)	V_{oc} (V)	FF	η (%)	R_s (Ω/cm^2)	R_{sh} (Ω/cm^2)	*Remark*
130 ºC	4.49	0.52	0.10	0.23	147	432	As-fabricated
	8.43	0.53	0.59	2.65	4.94	967	After light soaking
150 ºC	4.27	0.42	0.12	0.22	160	456	As-fabricated
	8.50	0.54	0.59	2.72	4.39	627	After light soaking
170 ºC	9.35	0.54	0.26	1.33	399	418	As-fabricated
	10.16	0.54	0.60	3.31	5.58	310	After light soaking
250 ºC	7.84	0.52	0.26	1.05	289	551	As-fabricated
	8.75	0.52	0.56	2.59	7.84	338	After light soaking

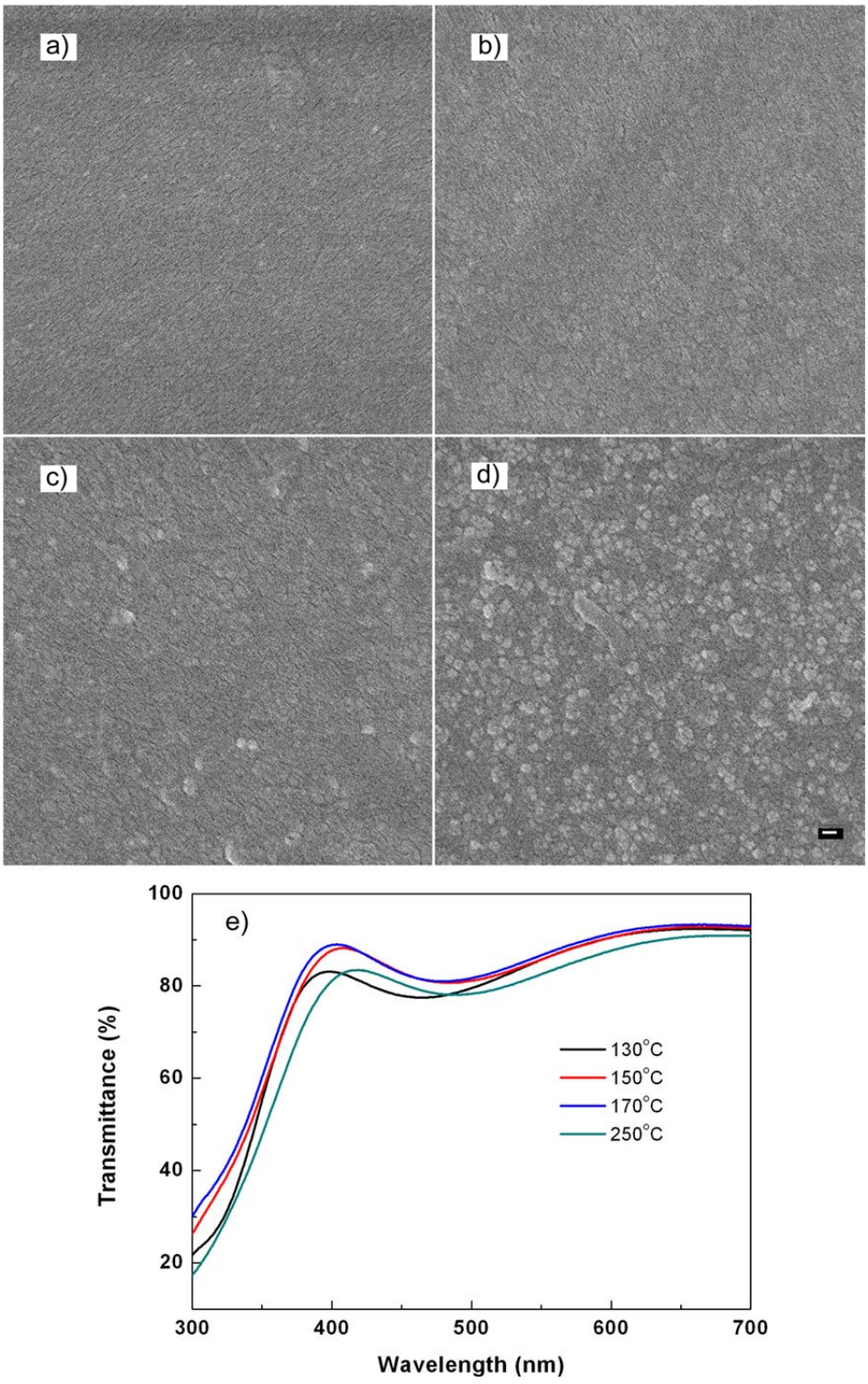

Figure 3.5 FESEM images of TiO_2 film surfaces deposited at (a) 130, (b) 150, (c) 170, and (d) 250 °C (scale bar: 100 nm), and (e) the optical transmittance spectra of these films.

Nevertheless, the better performance of the cells based on 15 nm amorphous TiO_2 layers fabricated at low temperature (130-170 ºC) as compared to that of the cell with the 15 nm poly-crystal TiO_2 layer demonstrates that low temperature ALD processed ultra-thin and dense TiO_2 layer is promising for use to achieve high performance and stable OSCs on plastic substrate. Moreover, the stable and robust ALD-produced TiO_2 film makes it possible to integrate the TiO_2 films on ITO plastic substrates for easier processing and distribution of the film products, which will benefit the roll-to-roll mass production of plastic OSCs.

Light soaking issue in device performance

For our case, the observed S-shape together with the high series resistance (see Table 3.1, measurements as fabricated) is mostly because of the low electrical conductivity of these TiO_2 layers. The S-shape is removed and the series resistance of the device is significantly decreased after light soaking, indicating that light illumination changes the electrical properties of the TiO_2 film. It is usually thought that high density surface state is produced on TiO_2 upon UV-light illumination, which may result in improved electron transport [3.39]. The surface states could be from oxygen vacancy or Ti^{3+} states induced by the photoreaction under light soaking [3.40, 3.41].

The change in the S-shape by light soaking is found reversible after storing the cell inside glovebox (without illumination) for a period of time. It is observed from Fig. 3.6 that, for the device after light soaking and stored in glovebox, the S-shape is returned bit by bit with the increase of the storage time, from 18h, 48h, 96h, to 8 days. Furthermore, when the device was placed under one more light soaking, the S-shape can be removed again.

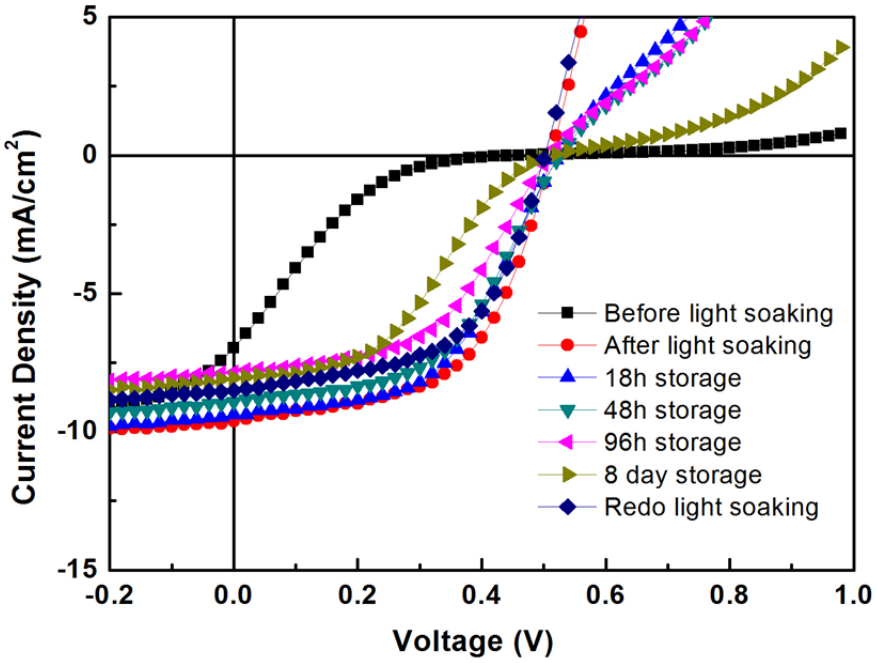

Figure 3.6 *J* – *V* curves of a cell measured after different storage time in N_2-filled glove box.

To further investigate the cause for the S-shape, we put the S-shape removed devices to be stored in three different environments of air ambient (dry box), N_2-filled glove box and high vacuum ($8x10^{-7}$ torr) separately, and measured the *J* – *V* characteristics before and after the storages (as shown in Fig. 3.7). Fig. 3.7 (a) shows that there is an obvious S-shape appeared in the *J* – *V* curve of the device stored in air ambient after only 3 hours. Moreover, there is little S-shape appeared in the *J* – *V* curve of the device stored in the glovebox even after 4 hours, as shown in Fig. 3.7 (b). Furthermore, there is no S-shape appeared in the device that is stored in high vacuum ambient for even 18 hours. The different behaviors of S-shape with different storage ambiences can be explained by different amounts of oxygen: the amount of oxygen contained in air ambient is much more than those contained in glove box and high vacuum, so it will be more quickly for the TiO_2 layer to adsorb oxygen and get rid of the surface states, which causes the conductivity of the TiO_2 film decrease and the S-

shape return back. Fig. 3.7 (d) shows the change of the series resistance after storage in glove box. It can be seen that R_s increases with the storage time. This result confirms our above explanation about the cause of the S-shape. The much improved stability observed in the devices stored in the high vacuum suggests that the S-shape can also be permanently removed by proper encapsulation of the devices to prohibit the oxygen and water contamination, which needs further investigation.

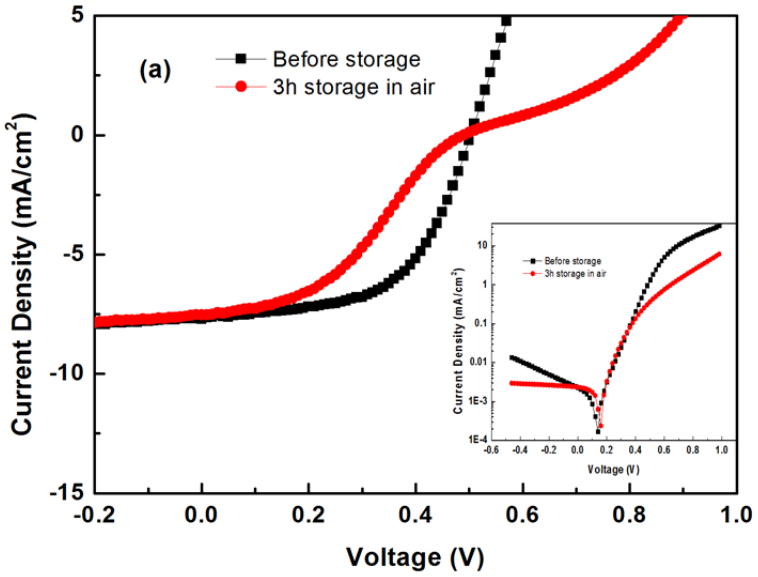

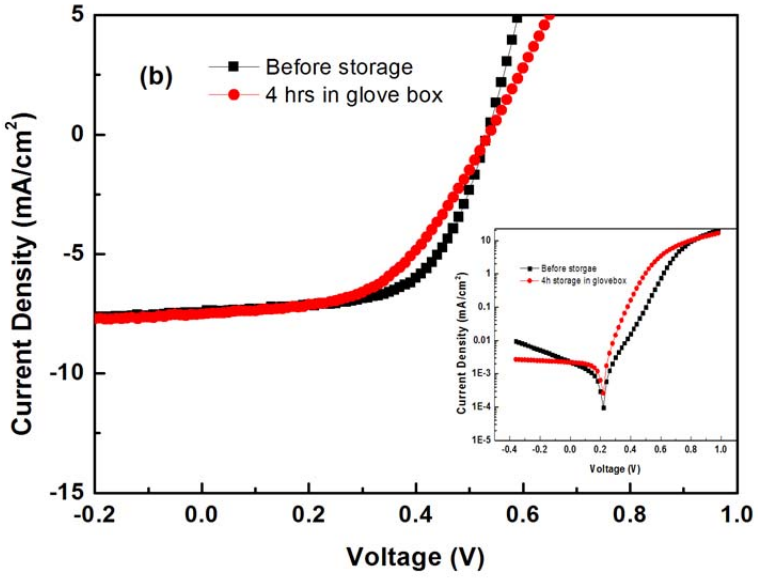

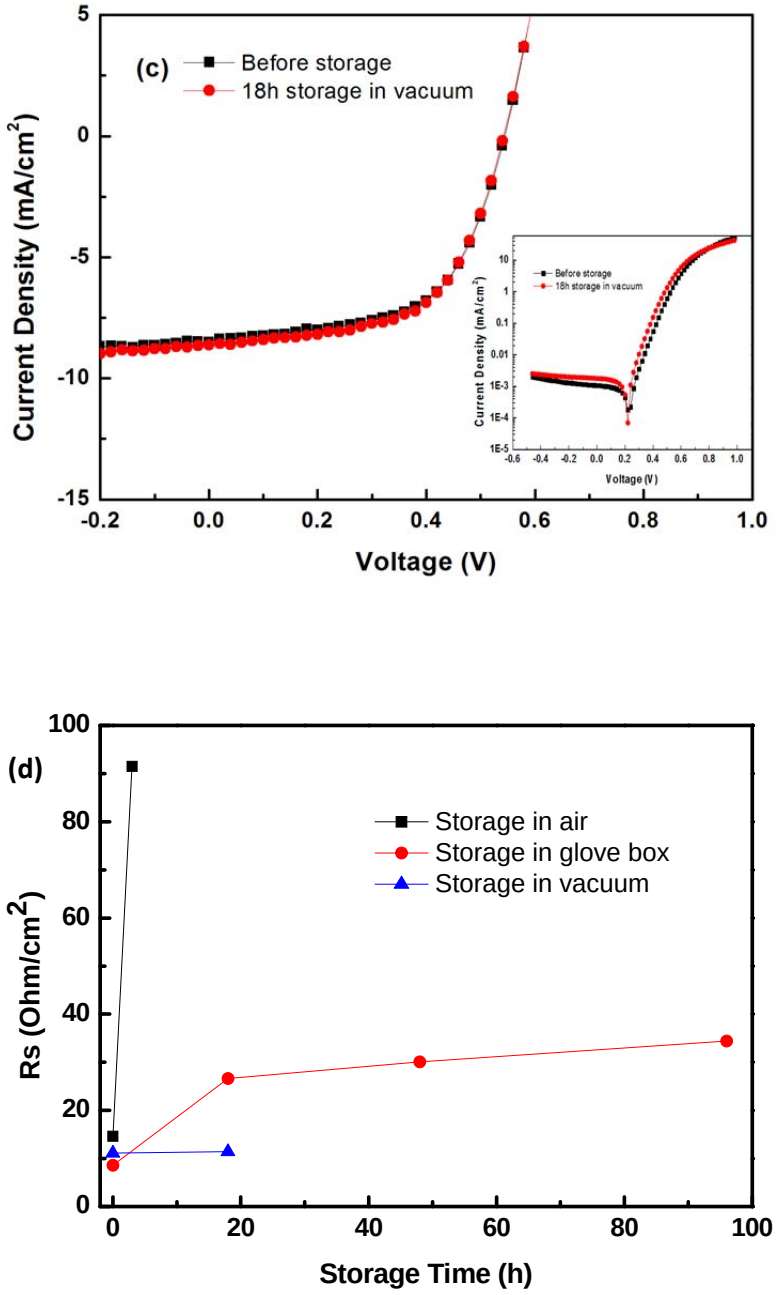

Figure 3.7 The $J - V$ curves measured for devices before and after storages in air ambient for 3 hours (a), in glove box for 4 hours (b), in high vacuum for 18 hours (c) (light soaking for 5 min was conducted for each cell before the storage) and the change of the series resistance with time for the cells stored in different ambient (d). Insets in a, b, and c are the corresponding dark $J - V$ curves before (black line) and after (red line) storage.

3.3 ALD-grown metal oxide interlayers on patterned ITO nanogroove cathode

In this section, the patterned ITO cathodes combined with ALD deposited metal oxide films are applied to enhance the inverted OSC device performance.

Fig. 3.8 shows the schematic illustration of the fabrication process of the ITO nano-groove arrays. The pre-cleaned ITO-coated glass substrates were spin coated with a layer of photoresist (Ultra-i 123) at 6000 rpm for 60 s (approximately 300 nm thick) and cured at 90 °C for 90 s. The photoresist was then exposed using a Lloyd's-mirror-type LIL set-up with a He-Cd laser source (λ = 325 nm) for about 60 s. The unexposed photoresist was removed using Microposit MF CD-26 developer, leaving behind lines of photoresist on the ITO surface. After that, the sample was chemically etched in Bromic acid for different times (30 s, 45 s, 60 s, 75 s and 90 s) to transfer the nano-groove patterns to the ITO layer. The variation of the etching time will result in different heights of the nano-grooves. Finally, all the photoresist was removed by acetone in an ultrasonic bath for 2 minutes.

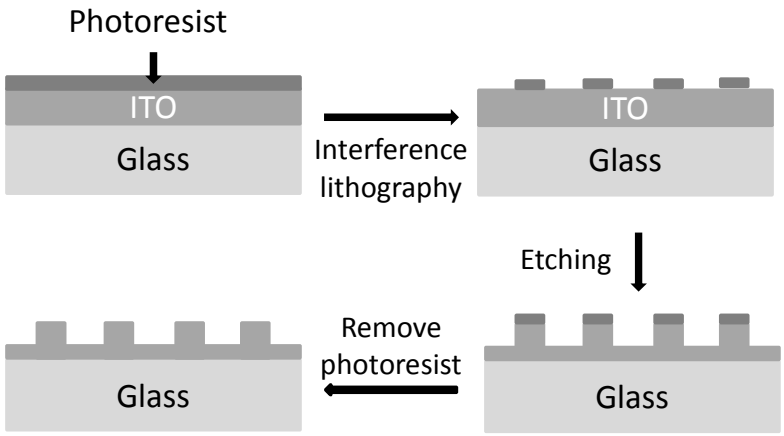

Figure 3.8 Schematic illustration of patterning ITO film by combining LIL and chemical etching.

The structure of the cell is ITO/metal oxide/P3HT:PCBM/MoO_3/Ag as shown in Fig. 3.9. The precursors used for ALD-grown ZnO film were H_2O and diethylzinc (DEZ) and the deposition temperature was 150 ^oC.

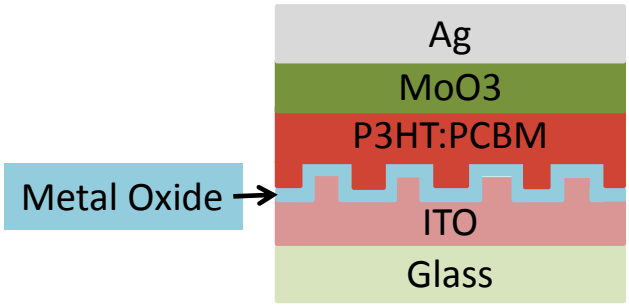

Figure 3.9 Schematic device structure of inverted organic solar cells.

Fig. 3.10 (a) to (e) show the AFM images and step profiles of the ITO surfaces with etching time of 30 s, 45 s, 60 s, 75 s and 90 s, respectively. The nano-groove patterns are clearly shown in both the AFM images and the step profiles for all these samples. The period of the pattern is about 500 nm. From the step profiles, it can be seen that the nano-groove depth increases with the etching time, and reaches to the maximum about 30 nm when the etching time is 75 s. However, when the etching time increases to 90 s, the pattern starts to disappear. This is because chemical wet etching is isotropic etching. When the etching time is long enough, the top of ITO surface can be totally etched and thus the photoresist will be removed and not protect the ITO surface furthermore.

Fig. 3.10 (f) shows the AFM image of ITO surface (75 s etching) after 18 nm atomic layer deposited ZnO film. Compared with the patterned ITO surface before ZnO layer deposition (Fig. 3.10 (d)), it clearly shows that there is no change with the pattern after depositing ZnO film, which indicates that ALD deposition can avoid "flattening effect".

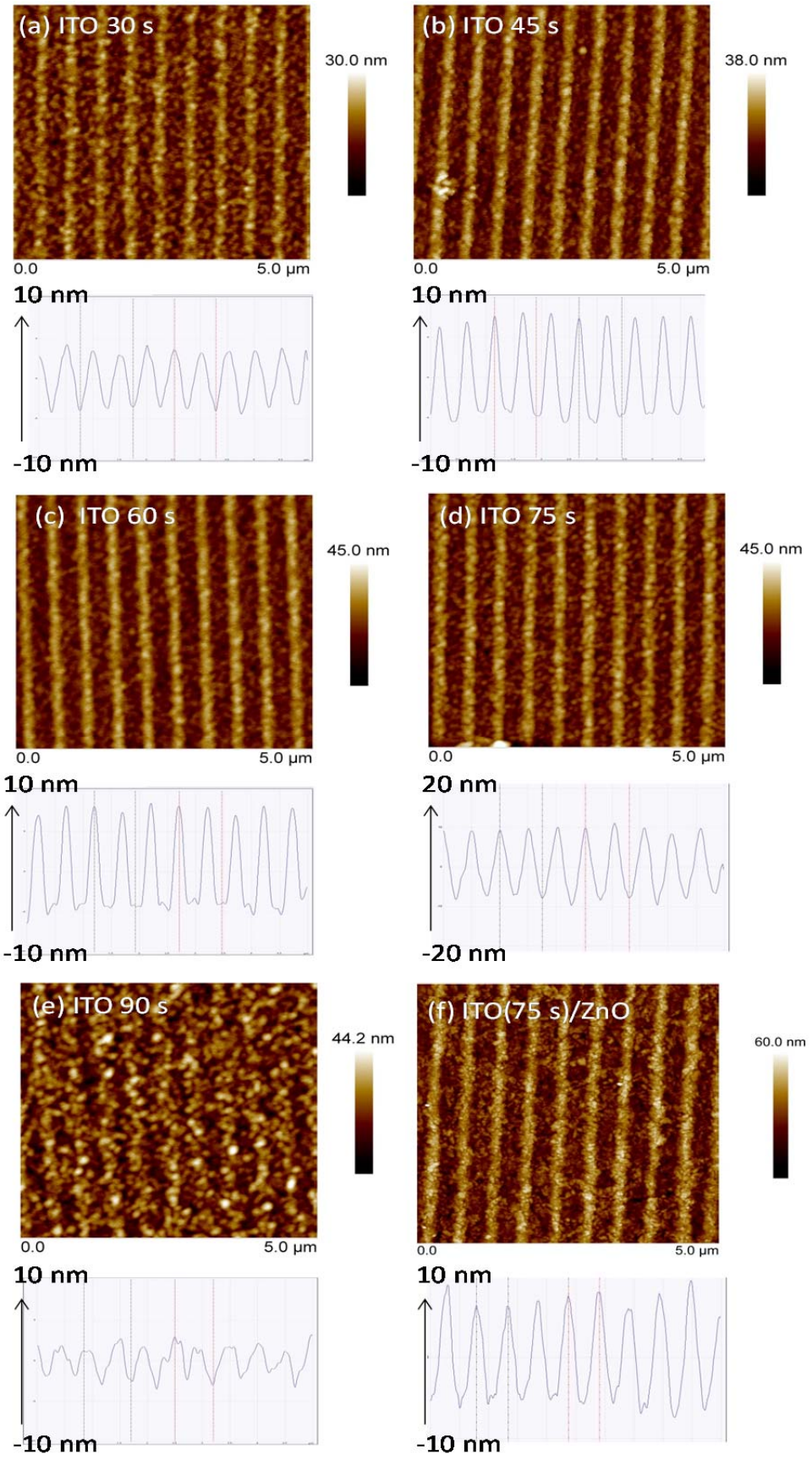

Figure 3.10 AFM images of patterned ITO film with different etching time: (a) 30 s, (b) 45 s, (c) 60 s, (d) 75 s, (e) 90s and (f) ZnO film deposited on patterned ITO (75 s).

Fig. 3.11 shows the *J* - *V* curves of the inverted OPV devices fabricated on planar ITO and patterned ITO electrodes with different etching time, and the cell performance parameters are summarized in Table 3.3. The ZnO film thickness has been optimized as shown in Fig. 3.12. From Table 3.3, it can be seen that both V_{oc} and FF of the devices (on flat ITO and patterned ITO) are similar, but J_{sc} of the patterned-ITO cells (30 s, 45 s, 60 s and 75 s) are higher than that of the flat-ITO cell, increasing from 10.21 (planar-ITO cell) to 10.42 (pattern-30s), 11.26 (pattern-45s), 11.31 (pattern-60s) and 11.24 mA/cm^2 (pattern-75s) with increment up to 10.77 %. A maximum PCE of 3.22% has been achieved when the etching time is 75 s.

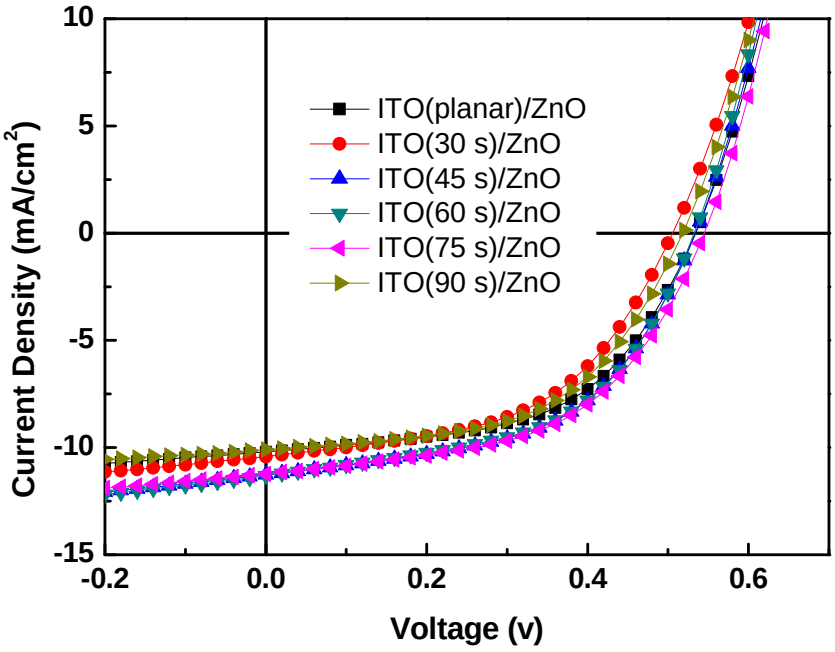

Figure 3.11 *J* – *V* curves of devices with flat ITO film and patterned ITO films with different etching time (30 s, 45 s, 60 s, 75 s and 90s).

Table 3.3 Values of photovoltaic performance parameters of inverted OSCs with and without electron selective layer (ESL) (under simulated illumination of 100 mW/cm^2 AM 1.5G). Devices were measured as-fabricated and after illumination.

ITO type	J_{sc} (mA/cm^2)	V_{oc} (V)	FF	η (%)	R_s (Ω/cm^2)	R_{sh} (Ω/cm^2)	ESL type
Planar	8.29	0.30	0.37	0.92	25	73	No ESL
Patterned	9.88	0.31	0.38	1.20	14	112	No ESL
Planar	10.21	0.53	0.54	2.92	11	350	ZnO
30 s	10.42	0.51	0.51	2.71	12	246	ZnO
45 s	11.26	0.53	0.53	3.16	11	241	ZnO
60 s	11.31	0.53	0.53	3.17	10	205	ZnO
75 s	11.24	0.54	0.53	3.22	11	285	ZnO
90 s	10.11	0.52	0.53	2.78	12	360	ZnO
Planar	2.25	0.43	0.13	0.12	752	71	TiO_2 as-fabricated
	9.52	0.52	0.54	2.67	14	361	TiO_2 after light soaking
Patterned	2.80	0.33	0.16	0.15	2327	538	TiO_2 as-fabricated
	11.72	0.52	0.51	3.07	5.9	479	TiO_2 after light soaking

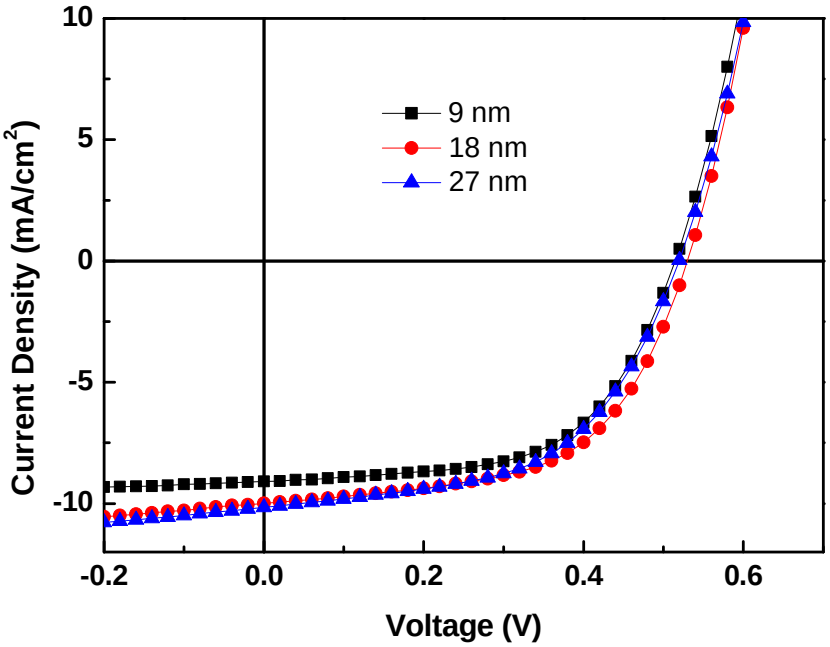

Figure 3.12 *J* – *V* curves of devices with flat ITO film and different-thick ZnO electron selective layers (9 nm, 18 nm, 27 nm).

There are several possible explanations for the increased J_{sc}. Firstly, the patterned ITO electrode increases the contact area between the cathode and active layer and shortens the electron collection pathway. Due to the limited carrier mobilities in the P3HT:PCBM film, the photo generated free electrons and holes in the active layer in a standard flat ITO device are easily recombined with each other when they are transporting towards the electrodes (charge-collection). The thicker of the active layer, the higher the recombination loss. Usually, it is electron conductivity limited charge-collection, that means the electron conductivity (through PCBM network) is lower than hole conductivity (through P3HT network) in the active layer [3.42]. Since in the patterned ITO device, the electrode is extended to the polymer film periodically, the contact area between the cathode and active layer is increased, and the pathway for the electron collection is shortened, which decreases the

recombination loss and thus increases the photocurrent. To further prove this point, two devices without ZnO interfacial layer on a planar ITO electrode and a patterned ITO electrode (75s etching time) were fabricated (with structure of ITO/P3HT:PCBM/MoO_3/Ag), the $J - V$ curves of devices are shown in Fig. 3.13, and the photovoltaic performance parameters of the two cells are also summarized in Table 3.3 (no electron selective layer (ESL)). It shows clearly that there is an increase in the current density from the cell with patterned ITO as compared to the cell with planar ITO, although both cells (without ESL) show much poorer performance than the cells with ZnO ESL.

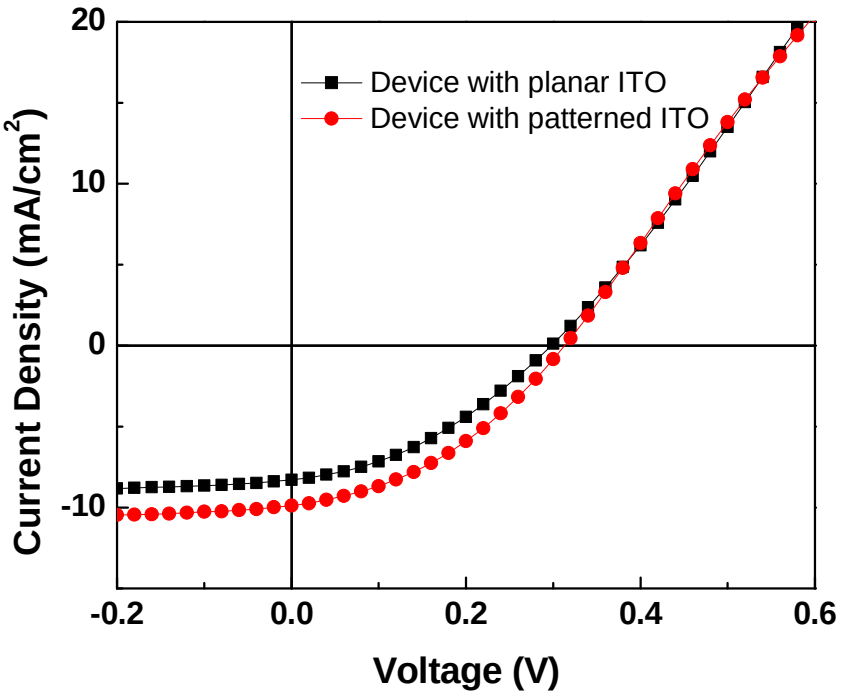

Figure 3.13 $J - V$ curves of devices with flat ITO film and patterned ITO films with nano-groove arrays without electron selective layer.

Light absorption is also one of the factors directly related to the value of J_{sc}. Organic solar cells with nano-structured substrate have been shown to reduce the reflection due to the good matching of the refractive index with air (light trapping) as compared to the device with planar substrate [3.43, 3.44]. Fig. 3.14 shows the light absorption and reflection spectra, over the wavelength range from 300 to 800 nm, of P3HT:PCBM films deposited on planar-ITO/ZnO and patterned-ITO/ZnO electrodes. The main absorption of P3HT:PCBM is located in the wavelength range from 400 to 650 nm. In this range, we can see from Fig. 3.14 the increased absorbance and decreased reflectance in the films with patterned ITO electrodes (with etching time of 45s, 60s and 75s) as compared to that with a planar ITO electrode, which is believed contributing to the photocurrent of the cell with patterned-ITO.

The surface morphologies of the P3HT:PCBM active layers fabricated on planar-ITO/ZnO electrode and patterned-ITO/ZnO electrodes are investigated by AFM measurements, and the AFM images and roughness data are shown in Fig. 3.15. It shows that the surface of the P3HT:PCBM active layer on planar-ITO is smooth with a root mean square (RMS) roughness of 1.98 nm. However, the surface RMS roughnesses of the active layer were increased to 3.46 nm, 3.84 nm, 4.61 nm, 3.95 nm and 2.27 nm for the films on patterned-ITO with etching time of 30s, 45s, 60s, 75s and 90s, respectively. This morphology change may be due to the graphoepitaxy which can be caused by the wet chemical etching [3.45].

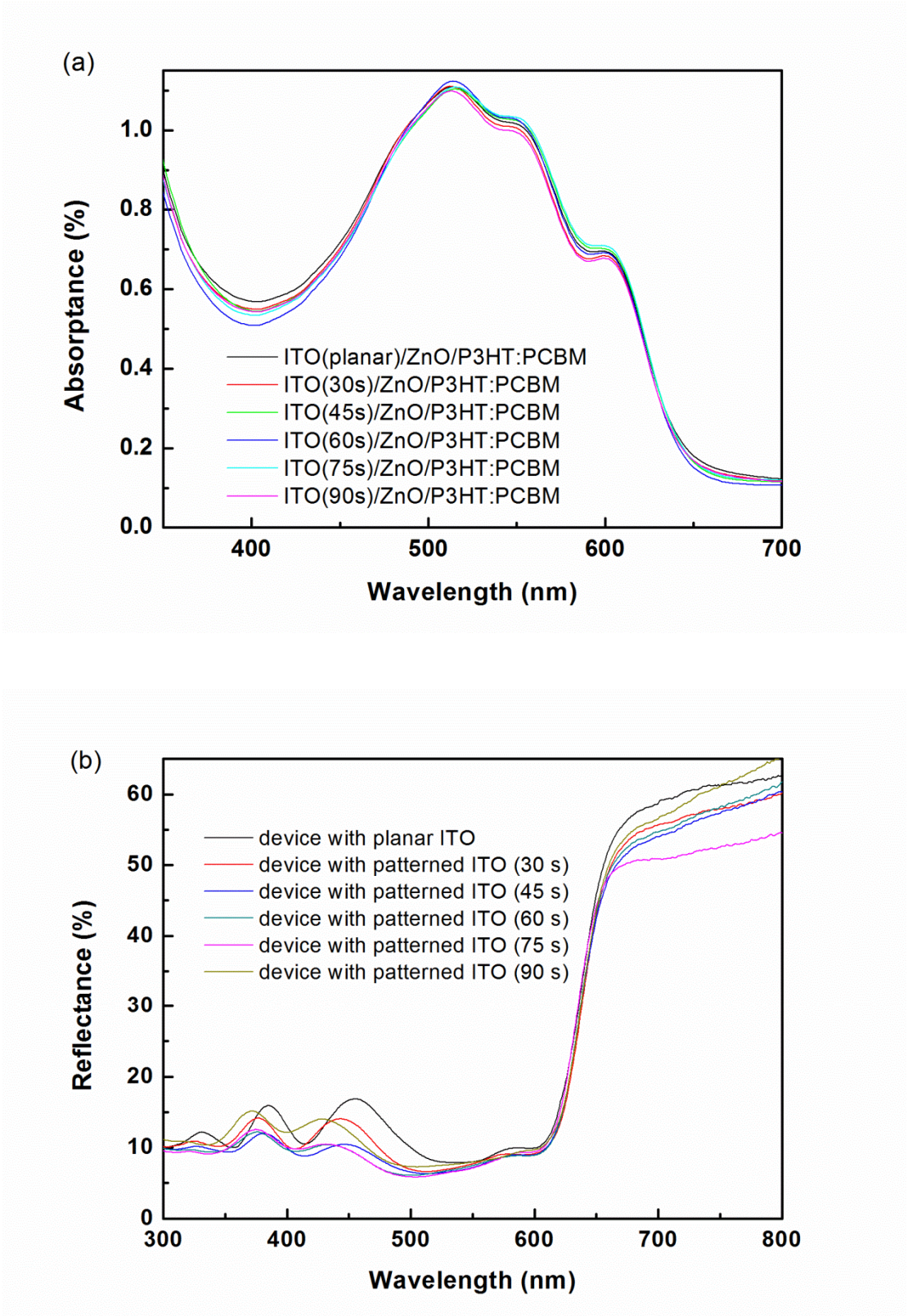

Figure 3.14 (a) The absorbance and (b) reflectance spectra of ITO/ZnO/P3HT:PCBM (with and without pattern) films.

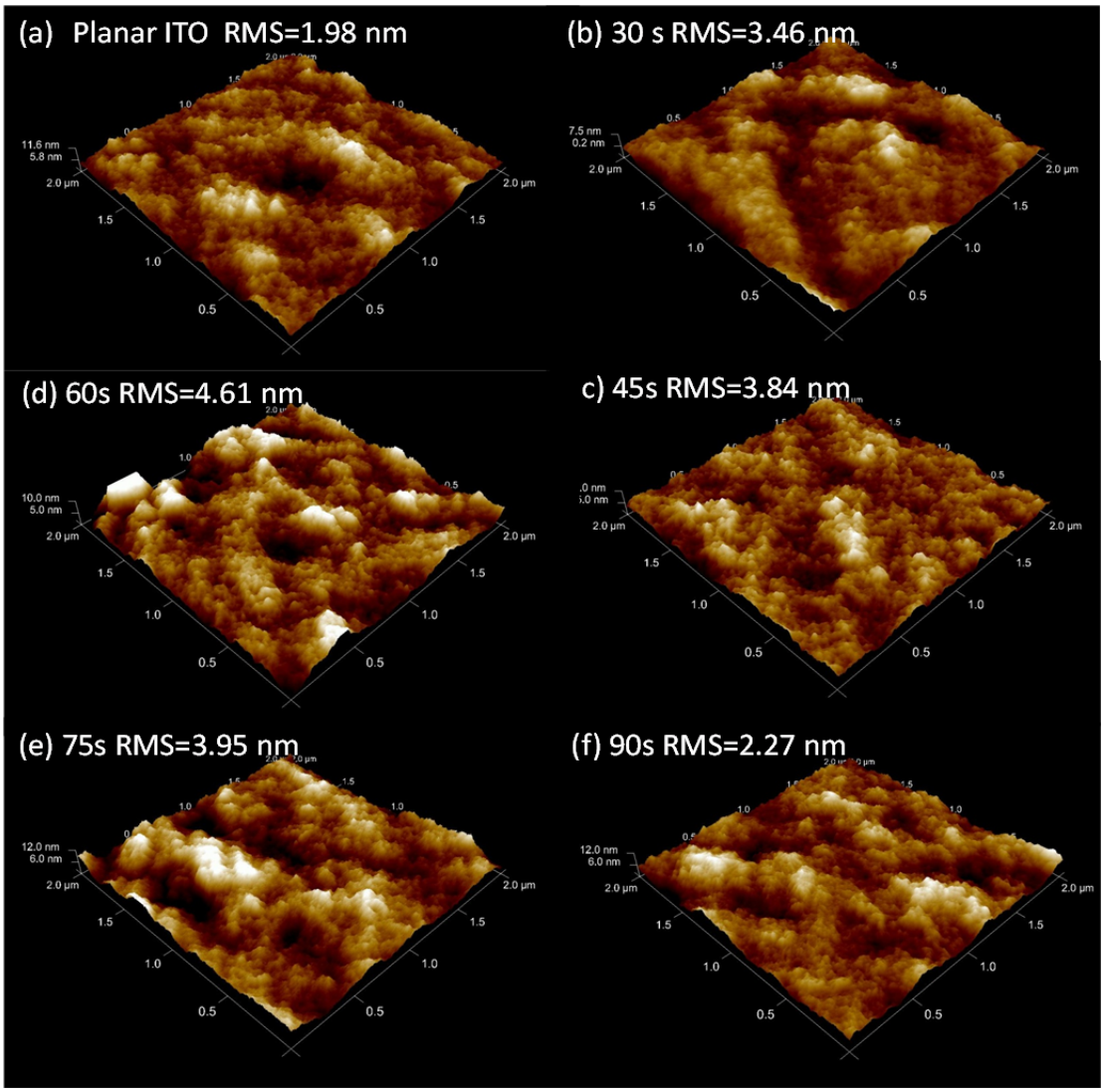

Figure 3.15 AFM images of P3HT:PCBM films coated on (a) flat ITO/ZnO substrate and patterned ITO/ZnO substrates with different etching time: (b) 30 s, (c) 45 s, (d) 60 s, (e) 75 s and (f) 90s.

ZnO layer can provide high electron mobility due to the high oxygen vacancy concentration. However, the dense surface defects may act as the trap-assistant recombination center, resulting in current loss [3.35, 3.36, 3.46]. When the contact area increases, the trap-assisted recombination alsos increase, which could limit the current increase for the patterned devices. However, compared with ZnO, TiO_2 layer contains less defects, which effectively reduces the current loss, but with comparable electron mobility, both making it to be an effective electron selective layer [3.47].

Fig. 3.16 (a) and (b) show the *J* - *V* curves of devices with flat and patterned ITO films after TiO_2 film deposition by measuring the devices as fabricated and after light soaking, respectively. The TiO_2 film was fabricated by ALD at 150 ^oC, since this deposition temperature is acceptable for nearly all the plastic substrates. The TiO_2 thickness was 15 nm. Light soaking is done by placing the device under illumination (AM1.5G solar simulator, 100 mW/cm^2) for a certain time. It shows that there is an obvious S-shape in each curve of the as-fabricated cell (Fig. 3.16 (a)), and the S-shape can be removed by light soaking (Fig. 3.16 (b)), which is due to the removal of the oxygen defects by light illumination resulting in much improved TiO_2 conductivity and improved electron injection. From Fig. 3.16 (b), it can be seen that, after illumination, the V_{oc} of the two devices (on flat ITO and patterned ITO) almost does no change, but the J_{sc} of the patterned-ITO cell is higher than that of the flat-ITO cell, increasing from 9.52 to 11.72 mA/cm^2. The increase (23.11%) is much higher than the ZnO based device (10.77%) due to less recombination occurred on the oxide surface.

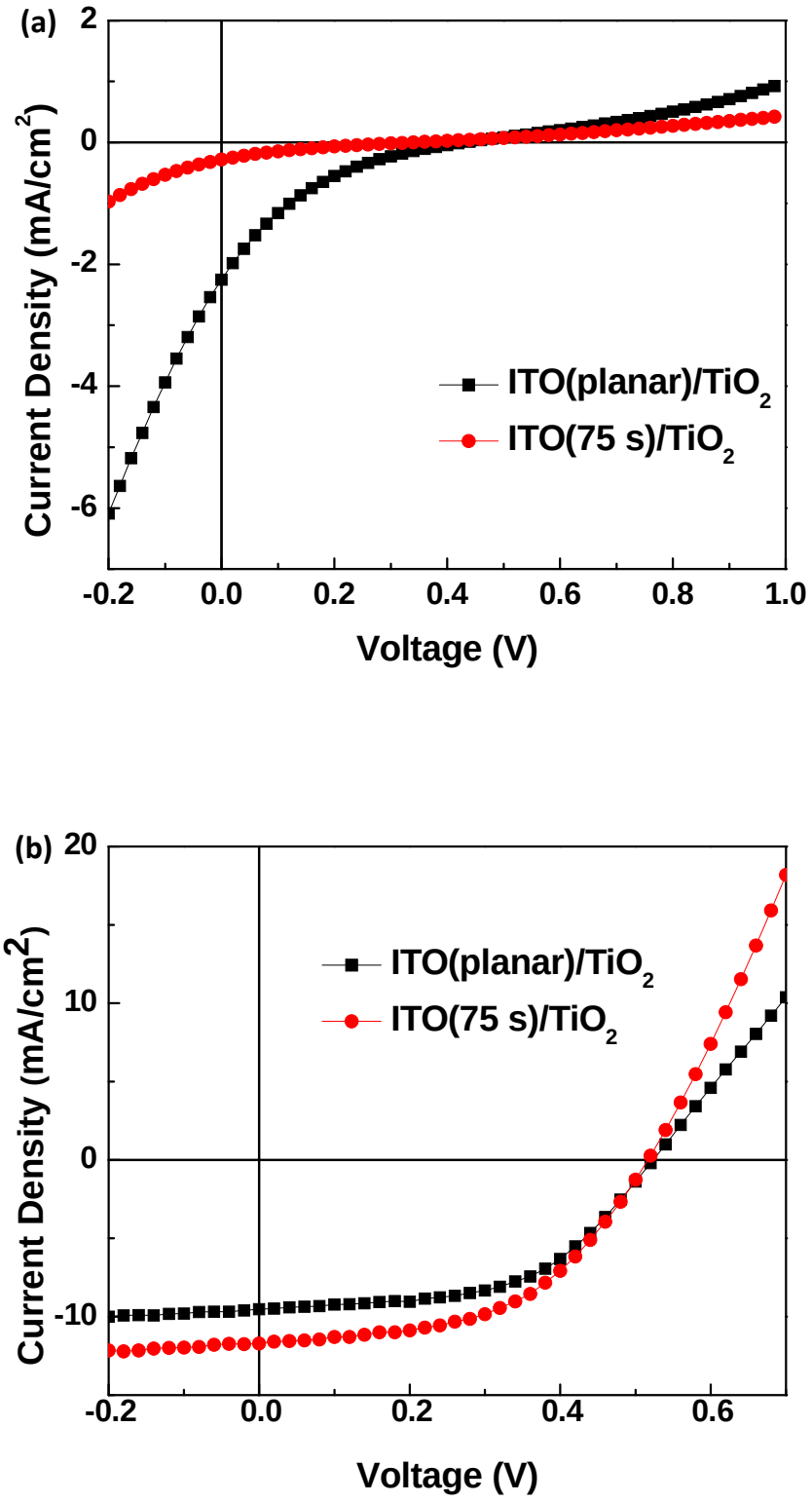

Figure 3.16 *J – V* curves of devices with planar ITO/TiO_2 and patterned ITO/TiO_2 films with nano-groove arrays measured as fabricated (a) and after light soaking (b).

3.4 Summary

In this chapter, firstly, TiO_2 films, fabricated using low temperature (e.g., 130−170 °C) ALD on flat ITO substrates, are used as electron selective interface layers to investigate inverted OSCs. It is found that though the as-deposited TiO_2 films are high resistive due to the presence of oxygen defects, the defects can be significantly reduced by light soaking. PV cells with 15-nm-thick amorphous-TiO_2 layers fabricated at low temperature show better performance than those with poly crystal TiO_2 with same thickness deposited at 250 °C. The low temperature ALD-grown TiO_2 films are dense, stable and robust with capability of conformal coating on nanostructural surfaces, showing a promising interface layer for achieving air-stable plastic OSCs.

After optimizing the flat device, patterned ITO electrodes with well-ordered periodic nano-groove structures were constructed using a simple and cost-effective method, LIL, and worked as the cathode. The patterned ITO cathode combined with ALD deposited metal oxide thin films (ZnO, TiO_2) as the electron selective layer were studied in inverted OSCs. Compared to the flat ITO cathode, the use of patterned ITO cathode leads to a significantly increased short circuit current density (J_{sc}) which increased by 10.8% (from 10.21 to 11.31 mA/cm^2) for devices using ZnO interlayer and 23.11% (from 9.52 to 11.72 mA/cm^2) for devices using TiO_2 interlayer. The improvement in the photocurrent is the result of enhanced charge collections and light absorption, and improved morphology in the active layer fabricated on patterned ITO substrate.

References

[3.1] N. S. Sariciftci, L. smilowitz, A. J. Heeger and F. Wudl, Science 258, 1474 – 1476 (1992).

[3.2] G. Yu, J. Cao, J. C. Hummelen, F. Wudl and A. J. Heeger, Science 270, 1789 – 1791 (1995).

[3.3] L. Müller-Meskamp, Y. H. Kim, T. Roch, S. Hofmann, R. Scholz, S. Eckardt, K. Leo and A. F. Lasagni, Advanced Materials 24, 906 – 910 (2012).

[3.4] I. L. Violi, M. D. Perez, M. C. Fuertes and G. J. A. A. Soler-Illia, ACS Applied Materials and Interfaces 4, 4320-4330 (2012).

[3.5] E. Nilsson, Y. Sakamoto and A. E. C. Palmqvist, Chemistry of Materials 23, 2781 – 2785 (2011).

[3.6] M. Rawolle, E. V. Braden, M. A. Niedermeier, D. Magerl, K. Sarkar, T. Fröschl, N. Hüsing, J. Perlich and P. Müller-Buschbaum, ChemPhysChem 13, 2412 – 2417 (2012).

[3.7] J. Y. Xie, H. Wang, H. D. Bai, P. Yang, M. X. Shi, P. Guo, C. Wang, W. T. Yang and H. H. Song, ACS Applied Materials and Interfaces 4, 2891 – 2896 (2012).

[3.8] C. Waldauf, M. Morana, P. Denk, P. Schilinsky, K. Coakley, S. A. Choulis and C. J. Brabec, Applied Physics Letters 89, 233517 (2006).

[3.9] J. Y. Kim, S. H. Kim, H.-H. Lee, K. Lee, W. Ma, X. Gong and A. J. Heeger, Advanced Materials 18, 572 – 576 (2006).

[3.10] A. K. K. Kyaw, X. W. Sun, C. Y. Jiang, G. Q. Lo, D.W. Zhao and D.L. Kwong, Applied Physics Letters 93, 221107 (2008).

[3.11] S. K. Hau, H.-L. Yip, O. Acton, N. S. Baek, H. Ma and A. K. Y. Jen, Journal of Materials Chemistry 18, 5113 – 5119 (2008).

[3.12] H. Sun, J. Weickert, H. C. Hesse and L. Schmidt-Mende, Solar Energy Materials and Solar Cells 95, 3450 – 3454 (2011).

[3.13] Y.-J. Kang, C. S. Kim, S.-H. Kwon and J. W. Kang, 37th IEEE Photovoltaic Specialists Conference; Seattle, June 19−24, 2011 ; IEEE:Piscataway, NJ, 2011; 001165 - 001166 (2011).

[3.14] S. B. Rim, S. Zhao, S. R. Scully, M. D. McGehee and P. Peumans, Applied Physics Letters 91, 243501 (2007).

[3.15] L. He, D. Lai, H. Wang, C. Jiang and Rusli, Small 8, 1664 – 1668 (2012).

[3.16] L. Müller-Meskamp, Y. H. Kim, T. Roch, S. Hofmann, R. Scholz, S. Eckardt, K. Leo and A.F. Lasagni, Advanced Materials 24, 906 – 910 (2012).

[3.17] M. E. Donders, H. C. Knoops, W. M. M. Kessels and P. H. Notten, ECS Transactions 41, 321 – 330 (2011).

[3.18] J. Y. Park, S.-W. Choi and S. S. Kim, Journal of Physics D: Applied Physics 44, 205403 (2011).

[3.19] T. H. Y. Tran, W. G. Haije, V. Longo, W. M. M. Kessels and J. Schoonman, Journal of Membrane Science 378, 438 – 443 (2011).

[3.20] T. R. B. Foong, Y. Shen, X. Hu and A. Sellinger, Advanced Functional Materials 20, 1390 – 1396 (2010).

[3.21] Z. Lin, C. Jiang, C. Zhu and J. Zhang, ACS Applied Materials and Interfaces 5, 713 – 718 (2013).

[3.22] Y. Lin, S. Zhou, X. Liu, S. Sheehan and D. Wang, Journal of the American Chemical Society 131, 2772 – 2773 (2009).

[3.23] C. Marichy, M. Bechelany and N. Pinna, Advanced Materials 24, 1017 – 1032 (2012).

[3.24] Z. He, C. Zhong, S. Su, M. Xu, H. Wu and Y. Cao, Nature Photonics 6, 591 – 595 (2012).

[3.25] N. Blouin, A. Michaud and M. Leclerc, Advanced Materials 19, 2295 – 2300 (2007).

[3.26] Y. Liang, D. Feng, Y, Wu, S.-T. Tsai, G. Li, C. Ray and L. Yu, Journal of the American Chemical Society 131, 7792 – 7799 (2009).

[3.27] H. A. Atwater and A. Polman, Nature Materials 9, 205 – 213 (2010).

[3.28] M. Wang, Y. Li, H. Huang, E. D. Peterson, W. Nie, W. Zhou, W. Zeng, W. Huang, G. Fang, N. Sun, X. Zhao, and D. L. Carroll, Applied Physics Letters 98, 103305 (2011).

[3.29] D. H. Wang, D.-G. Choi, K.-J. Lee, J.-H. Jeong, S. H. Jeon, O. Park and J. H. Park, Organic Electronics 11, 285– 290 (2010).

[3.30] M.-G. Kang, M.-S. Kim, J. Kim and L. J. Guo, Advanced Materials 20, 4408 – 4413 (2008)

[3.31] K. S. Nalwa, J.-M. Park, K.-M. Ho and S. Chaudhary, Advanced Materials 23, 112 – 116 (2011).

[3.32] P.-C. Tseng, M.-H. Hsu, M.-A. Tsai, C.-W. Chu, H.-C. Kuo and P. Yu, Organic Electronics 12, 886 – 890 (2011).

[3.33] J. Li, L. Zuo, H. Pan, H. Jiang, T. Liang, Y. Shi, H. Chen and M. Xu, Journal of Materials Chemistry A DIO: 10.1039/c2ta00687a (2013).

[3.34] S.-Y. Chen, Y.-T. Yen, Y.-Y. Chen, C.-S. Hsu, Y.-L. Chueh and L.-J. Chen, RSC Advance 2, 1314 – 1317 (2012).

[3.35] C.-H. Hsieh, Y.-J. Cheng, P.-J. Li, C.-H. Chen, M. Dubosc, R. M. Liang and C.-S. Hsu, Journal of the American Chemical Society 132, 4887 – 4893 (2010).

[3.36] S. K. Hau, H.-L. Yip, H. Ma and K.-Y. Jen, Applied Physics Letters 93, 233304 (2008).

[3.37] M. Zhu, L. Zhou, B. Li, M. K. Dawood, G. Wan, C. Q. Lai, H. Cheng, K. C. Leong, R. Rajagopalan, H. P. Too, and W. K. Choi, Nanoscale 3, 2723-2729 (2011).

[3.38] M. Campoy-Quiles, T. Ferenczi, T. Agostinelli, P. G. Etchegoin, Y. Kim, T. D. Anthopoulos, P. N. Stavrinou, D. D. C. Bradley and J. Nelson, Nature Materials 7, 158 – 164 (2008).

[3.39] B. A. Gregg, S. G. Chen and S. Ferrere, Journal of Physical Chemistry B 107, 3019 – 3029 (2003).

[3.40] R. Wang, K. Hashimoto, A. Fujishima, M. Chikuni, E. Kojima, A. Kitamura, M. Shimohigoshi and T. Watanabe, Advanced Materials 10, 135 – 138 (1998).

[3.41] K. Komaguchi, T. Maruoka, H. Nakano, I. Imae, Y. Ooyama and Y. Harima, Journal of Physical Chemistry C 113, 1160 – 1163 (2009).

[3.42] G. Li, V. Shrotriya, Y. Yao, J. Huang and Y. Yang, Journal of Materials Chemistry 17, 3126 – 3140 (2007).

[3.43] J. Q. Xi, M. F. Schubert, J. K. Kim, E. F. Schubert, M. Chen, S. Y. Lin, W. Liu and J. A. Smart, Nature Photonics 1, 176 – 179 (2007).

[3.44] Y. F. Huang, S. Chattopadhyay, Y. J. Jen, C. Y. Peng, T. A. Liu, Y. K. Hsu, C. L. Pan, H. C. Lo, C, H. Hsu, Y. H. Chang, C. S. Lee, K. H. Chen and L. C. Chen, Nature Nanotechnology 2, 770 – 774 (2007).

[3.45] K. A. Singh, T. Young, R. D. McCullough, T. Kowalewski and L. M. Porter, Advanced Functional Materials 20, 2216 – 2221 (2010).

[3.46] L. J. Brillson and Y. C. Lu, Journal of Applied Physics 109, 121301 (2011).

[3.47] E. L. Ratcliff, B. Zacher and N. R. Armstrong, Journal of Physical Chemistry Letters 1337 – 1350 (2011).

Chapter 4

Solution Processed Metal Oxide Films as Electron Selective Layer in Inverted OSCs

4.1 Introduction

In chapter 3, ALD deposited metal oxide film as electron selective layer (ESL) in inverted OSCs is discussed. However, the long-time consumption and non-cost effective metal oxide deposition process is not desirable for the roll-to-roll and cost-effective fabrication process for OSCs. As a result, the solution processed metal oxide films as ESL in inverted OSCs are fully worth of investigation.

Zinc oxide (ZnO) and titanium oxide (TiO_x) films have been considered as good candidates due to the acceptable electron mobility and high transparency in the visible wavelength range which allow them to be the effective transporter and excellent waveguide [4.1, 4.2]. Meanwhile, ZnO and TiO_x are cheap and environmentally friendly materials and can be synthesized with high purity at low temperature. Besides, ZnO and TiO_x buffer layers can be easily prepared and processed via a solution method followed by thermal annealing at relatively low temperature, which makes them compatible with roll-to-roll fabrication onto flexible substrates [4.3, 4.4].

In this chapter, aqueous solution processed ZnO and sol-gel TiO_x films as ESLs are investigated in inverted OSCs. Both device performance and photo-stability will be studied.

4.2 Effects of post-treatments on aqueous solution processed ZnO films in OSCs

Solution processed ZnO is mainly obtained by sol-gel, nano-crystalline colloid (Nc-ZnO) and aqueous solution route. However, sol-gel based ZnO usually requires high annealing temperature ($\geq$ 200 ^{o}C) to remove carbon impurities, which is not compatible with flexible substrates [4.4, 4.5]. The colloidal processed Nc-ZnO possesses much larger surface area than the corresponding dense layers, which results in a significantly environmentally sensitive electrical performance in ambient atmosphere [4.6, 4.7]. While the aqueous solution of ammine-hydroxo zinc complex could avoid these problems to afford the capability of low temperature annealing to densify ZnO thin films [4.8]. Previously, ZnO electron selective layers deposited by aqueous solutions of an ammine-hydroxo zinc complex have been investigated and showed much higher performance [4.9, 4.10]. Kim *et al.* has reported the effects of different annealing temperatures on the inverted OSC device performance showing that the annealing temperature could be as low as 80 ^{o}C [4.9]. However, studies on post-treatment have not yet been reported.

In this section, we investigated the effects of different post-treatments using thermal, humidity, and vacuum on aqueous solution-processed ZnO buffer layers on the film properties and inverted OSC device performance. It was found that the

thermal and vacuum post-treatments not only reduce the surface defect sites but also significantly increase the charge carrier mobility of ZnO films to 0.36 $cm^2V^{-1}s^{-1}$ and 0.31 $cm^2V^{-1}s^{-1}$, respectively, compared to the as-prepared films. Finally, efficient inverted OSC devices with 3.58 % and 3.51 % PCE based on P3HT and $PC_{61}BM$ blend were achieved, respectively, which is much higher (15 ~ 20 % enhancement) compared to the reference device based on the ZnO buffer layer without post-treatment.

4.2.1 Effects of ZnO film post-treatments on device performance

The ZnO aqueous solution was prepared as described in section 2.2.3 and the inverted OSC fabrication process was described in section 2.2.2. ZnO solution was spin-coated on top of ITO substrates at 3000 rpm for 30s. The reference device (device A) was prepared with as-spun ZnO thin film and directly thermally annealed at 150 ^oC for 10 min. Devices B, C and D were firstly prepared in manner similar to device A, but further treated at 150 ^oC for 12 h in an oven (device B), or with high humidity air treated for 12 h (RH 80%) (device C) or with 0% RH high vacuum for 12 h in vacuum chamber (device D). Fig. 4.1 (a) and (b) illustrate the schematic device structure and the band diagram of the inverted OSCs, respectively.

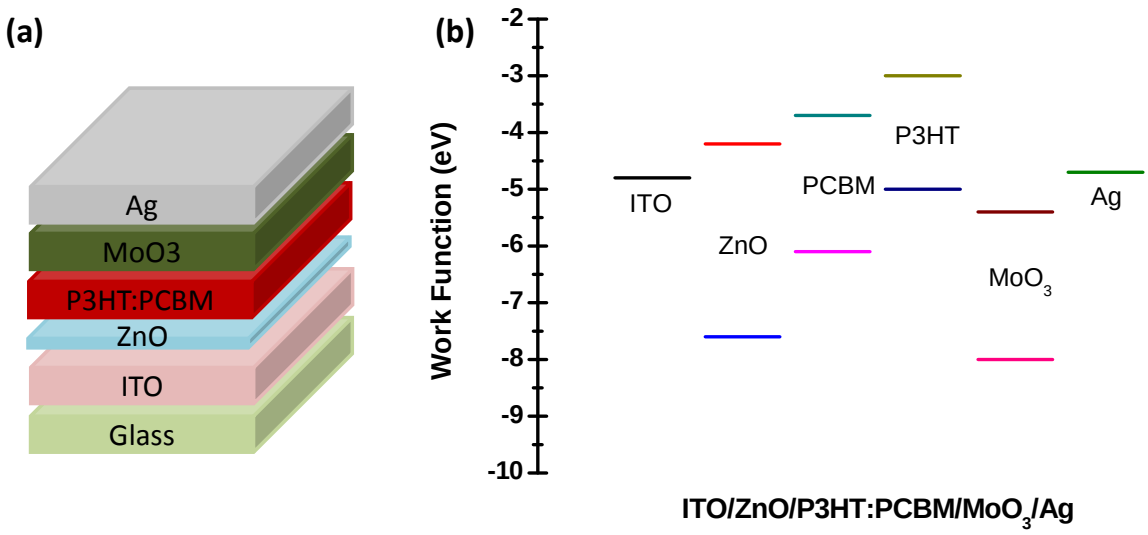

Figure 4.1 (a) Device structure of the inverted P3HT:$PC_{61}BM$ solar cell and (b) energy level diagram of the component materials used in device fabrication.

The current density – voltage (J – V) characteristics of the P3HT:$PC_{61}BM$ devices incorporating ZnO buffer layers without (device A) and with thermal, humidity, and vacuum treatments (devices B, C, D respectively) are shown in Fig. 4.2 (a), and the corresponding extracted device parameters are summarized in Table 4.1. Compared with reference device (device A), the V_{oc} slightly increases for thermal and vacuum treated devices. However, a significant increase in short circuit current density (J_{sc}) from 8.93 mA/cm^2 (device A) to 10.29 mA/cm^2 (device B) upon thermal post-treatment was observed. The series resistance (R_s) decreases from 9.7 Ω/cm^2 to 8.8 Ω/cm^2. For humidity treatment, while there was almost no change and the vacuum treatment resulted in a large improvement to 9.92 mA/cm^2 with a smaller R_s of 9.3 Ω/cm^2. The resulting PCEs were 3.58%, 3.07%, and 3.51% for thermal, humidity, and vacuum treatment, respectively. Incident photon-to-current conversion efficiency (IPCE) spectra of these devices are shown in Fig. 4.2 (b). For devices B and D, the

maximum IPCEs were 71% and 68% at the wavelength of 550 nm, respectively. The integrated IPCE values are all in good agreement with the measured J_{sc}.

In order to investigate the feasibility in other materials systems, the inverted solar cell based on PTB7/$PC_{71}BM$ incorporating with the ZnO layer after thermal post-treatment and reference cell have also been fabricated. The $J - V$ characteristics and photovoltaic parameters of the device are shown in Fig. 4.3 (a). A high PCE of 7.1% for the device with optimized ZnO layer was obtained with V_{oc} of 0.74 V, J_{sc} of 14.34 mA/cm^2 and FF of 0.67. Compared with the reference device performance, V_{oc} and FF are similar, while J_{sc} is higher than that of the reference device, 13.76 mA/cm^2. The IPCE spectrum is shown in Fig. 4.3 (b). The integrated IPCE value is in good agreement with the measured J_{sc}. To understand the mechanisms of post-treatment effects on the device performance, various techniques were employed.

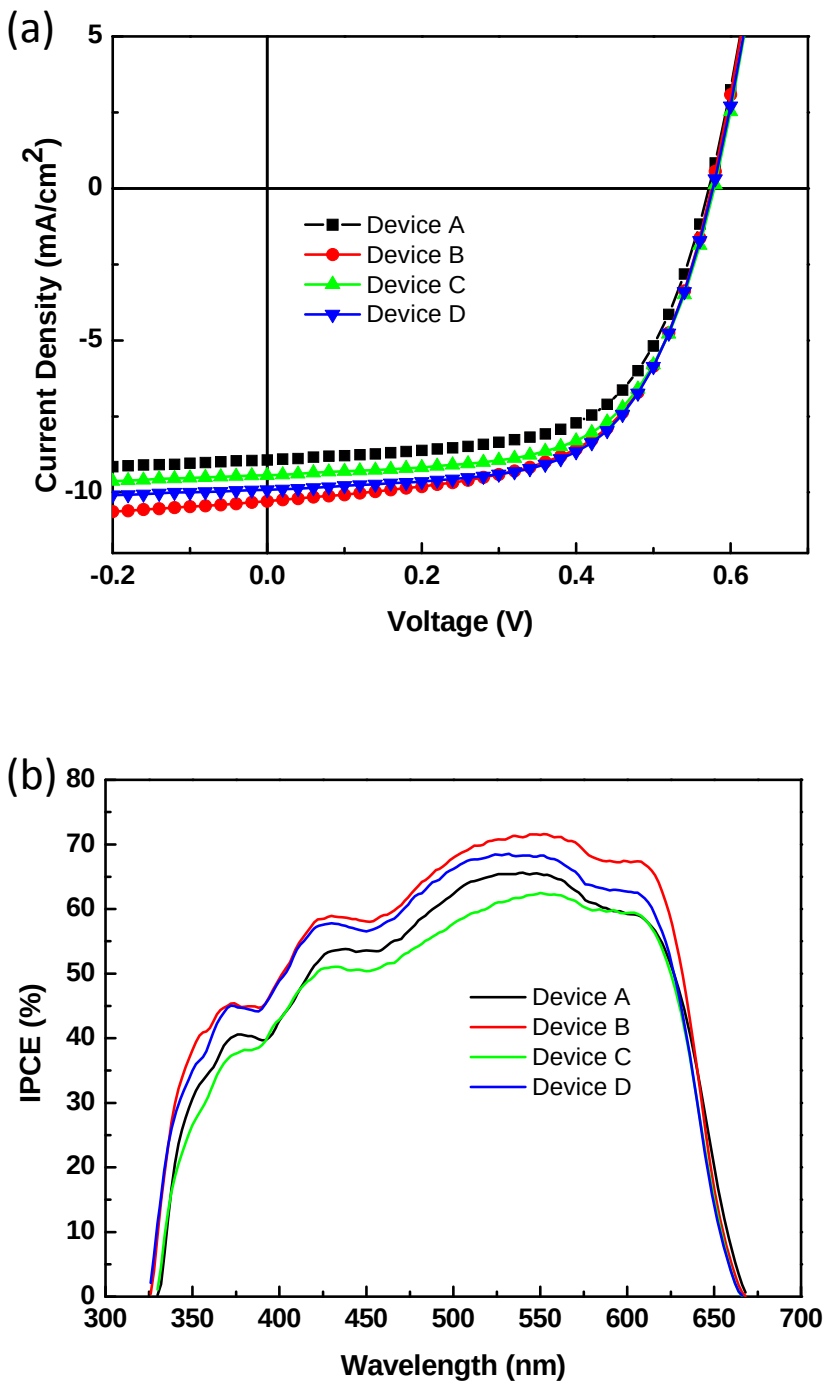

Figure 4.2 (a) *J – V* characterisctics of inverted P3HT:PC_{61}BM solar cells incorporating ZnO films without and with different post-treatments. (b) IPCE spectra of inverted P3HT:PC_{61}BM solar cells.

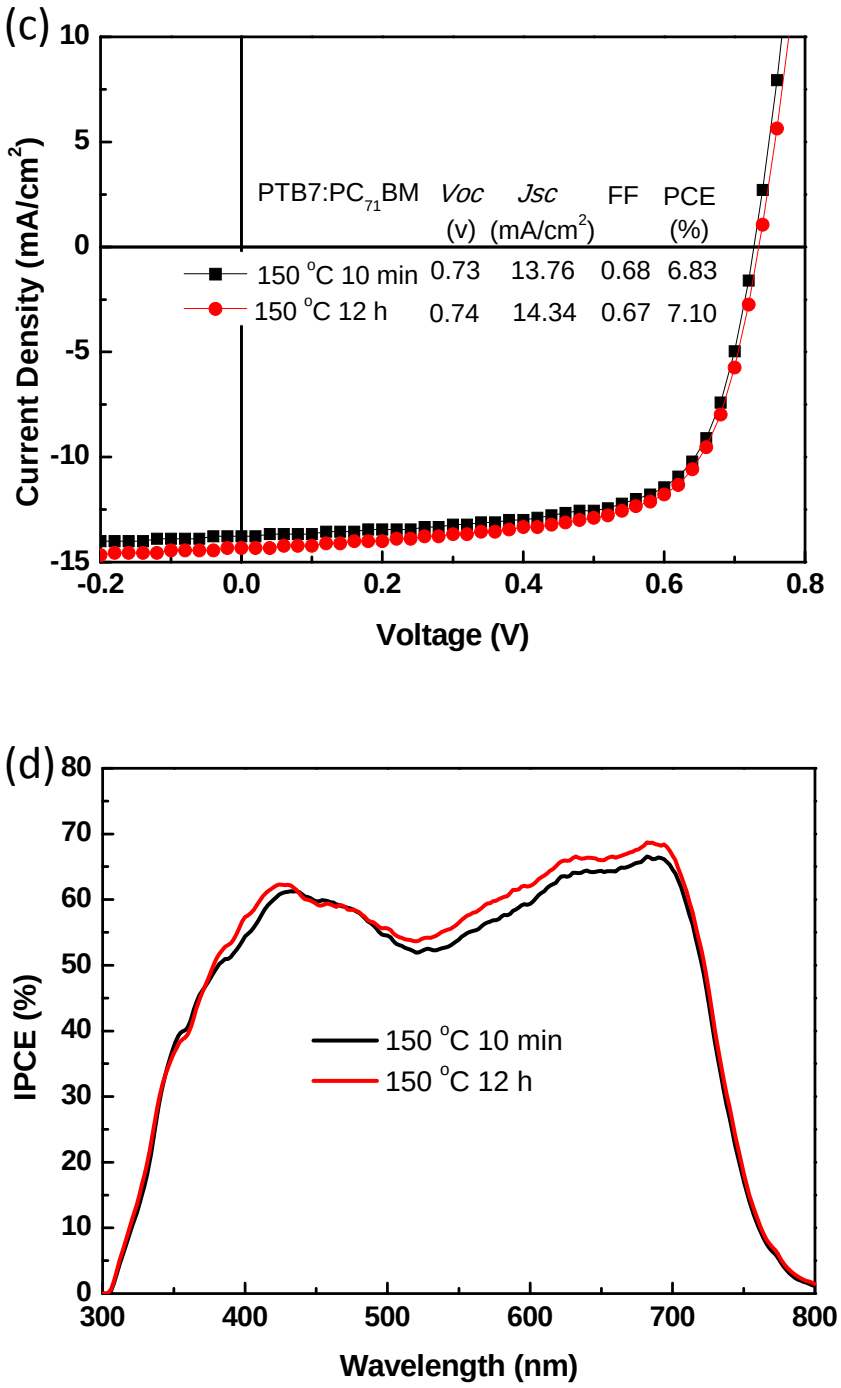

Figure 4.3 (a) *J* – *V* characterisctics of inverted PTB7:$PC_{71}BM$ solar cells. (b) IPCE spectra of inverted PTB7:$PC_{71}BM$ solar cells.

Table 4.1 Optical and electrical properties of ZnO films without (device A) and with thermal (device B), humidity (device C) and vacuum (device D) post-treatments, and device photovoltaic performance parameters of inverted P3HT:$PC_{61}BM$ solar cells incorporating these ZnO films as the electron transport layer.

Device	E_g (eV)	μ_e ($cm^2 V^{-1} s^{-1}$)	V_{TH} (V)	J_{sc} (mA/cm^2)	V_{oc} (V)	FF	η (%)	R_s (Ω/cm^2)	R_{sh} (Ω/cm^2)
A	3.418	0.225	27-32	8.93	0.56	0.61	3.05	9.7	900
B	3.354	0.360	16-21	10.29	0.58	0.60	3.58	8.8	615
C	3.406	0.183	26-32	9.01	0.56	0.61	3.07	10.2	947
D	3.398	0.311	25-29	9.92	0.58	0.61	3.51	9.3	1049

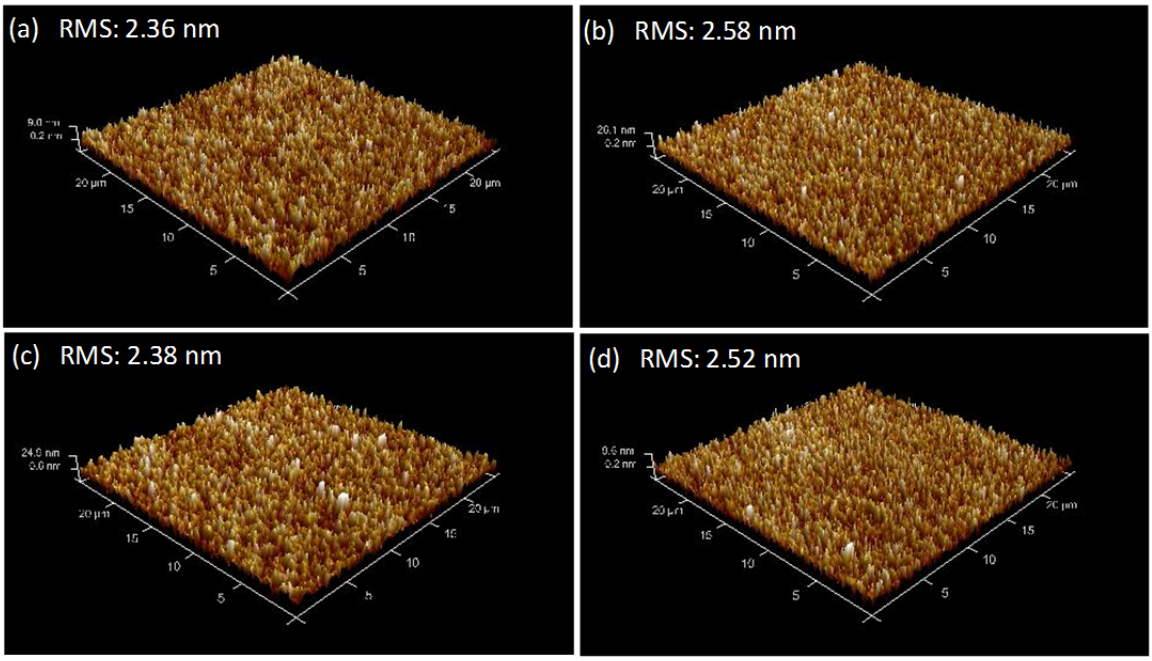

Figure 4.4 AFM images (25μm × 25 μm) of the ZnO films deposited on ITO coated glass substrates without (a), and with thermal (b), humidity (c), and vacuum post-treatment (d), respectively.

4.2.2 Surface roughness of ZnO films

The surface morphologies of the ZnO films (on ITO coated glass substrate) without and with different post-treatments were measured by tapping-mode AFM as shown in Fig. 4.4. The roughness mean square (RMS) values were 2.36 nm, 2.58 nm, 2.38 nm, and 2.52 nm for the ZnO films without and with thermal, humidity, and vacuum post-treatments, respectively. As can be seen, the post-treatment has little effect on the surface roughness, which means that the current density increase is not caused by the surface roughness change.

4.2.3 Transmittance and optical bandgap of ZnO film

The transmittance of the metal oxide buffer layer was investigated by UV-Vis spectroscopy to study the post-treatment effect on ZnO surface properties. Fig. 4.5 (a) shows the UV-visible wavelength optical transmittance spectra of bare ITO film and ZnO buffer layers coated on ITO (ITO/ZnO) films with different post-treatments. It can be seen that all ITO/ZnO films have good transmittances, above 80% over the visible wavelength range which are close to the bare ITO film. Meanwhile, in the range from 370 nm to 450 nm, the transmittance of the ITO/ZnO layers are higher than the bare ITO film, which is due to the antireflection caused by the ZnO layer coated on the ITO substrate [4.1].

In order to further investigate the optical bandgap of each ZnO buffer layer, the optical transmittance spectra of ZnO buffer layers coated on quartz substrates have been measured and shown in Fig. 4.5 (b). From the transmittance spectra, the absorption coefficient as a function of photon energy has been plotted in Fig. 4.5 (c),

and the optical bandgap of each ZnO film can be read. The absorption coefficient α can be calculated using $T = Aexp(-\alpha d)$, where T is the transmittance of the ZnO film, A is a constant and approximately unity, and d is the film thickness [4.11]. The value of optical bandgap can be calculated using the Tauc model [4.12] and the Davis Mott model [4.13] in the high absorbance region: $\alpha h\upsilon = D(h\upsilon - E_g)^n$, where $h\upsilon$ is the photon energy, E_g is the optical bandgap, D is a constant, and n equals to 1/2. In Fig. 4.5 (c), the relationship between $(\alpha h\upsilon)^2$ and $h\upsilon$ is plotted. The E_g value can be obtained by extrapolating the linear portion to the photon energy axis. The optical bandgap values obtained are also summarized in Table 4.1. It can be seen that the bandgaps of the ZnO films decreased after post-treatments. The band gap of the ZnO film decreased from 3.418 eV to 3.354 eV, 3.406 eV, and 3.398 eV for thermal, humidity, and vacuum post-treatment, respectively. The narrowing bandgap should be due to increased crystallinity caused by the post-treatments. Same results were also observed when increasing the thermal annealing temperatures [4.11]. The increased crystallinity should be responsible for current density increase upon post-treatments due to the decreased electron extraction barrier between the metal oxide conduction band and the lowest unoccupied molecular orbital (LUMO) of PCBM.

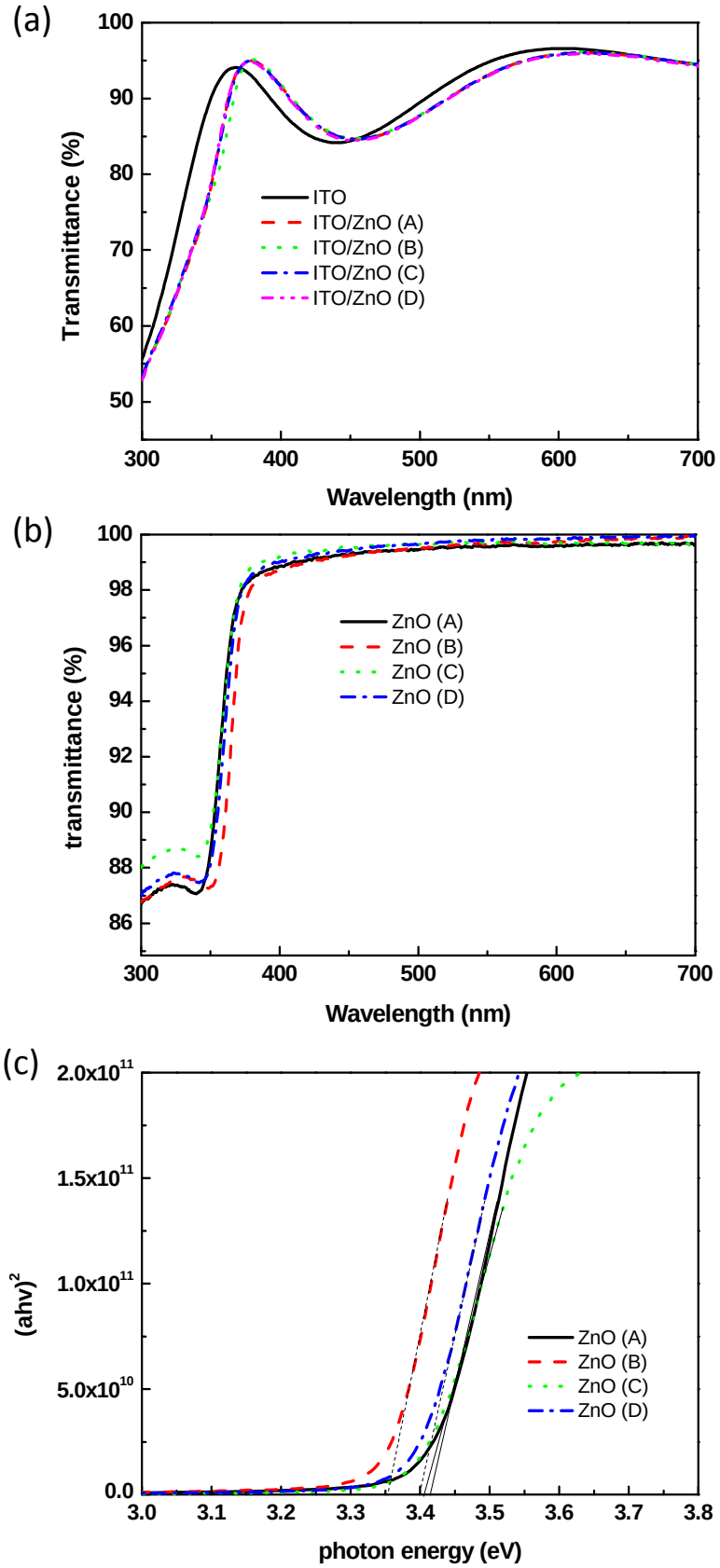

Figure 4.5 Transmittance spectra of (a) ITO and ITO/ZnO buffer layers, and (b) ZnO buffer layers deposited on quartz sbstrates. (c) plot of $(\alpha h\upsilon)^2$ vs. photon energy for ZnO films with different post-treatments.

4.2.4 Photoluminescence spectroscopy of ZnO thin films

The surface defect of ZnO films was studied with the room temperature photoluminescence (PL) spectra deposited on quartz substrates without/with post-treatments (Fig. 4.6). Strong emission at ~ 370 nm was observed for all the samples, which corresponds to the near band-edge emission [4.14]. This band is usually assigned to free excitons recombination or unspecified localized state [4.14]. Usually, a broad green emission peak is present in the ZnO PL spectrum, which is commonly referred to as a deep-level or trap-state emission. The green emission has been attributed to the singly ionized oxygen vacancy in ZnO film and the emission results from the radiative recombination of a photo-generated hole with an electron occupying the oxygen vacancy [4.15]. For our cases, the weak green emission peak and narrow UV band after post-treatments indicate increased film crystallinity and negligible contribution of defects, which are responsible for the deep level emissions [4.16].

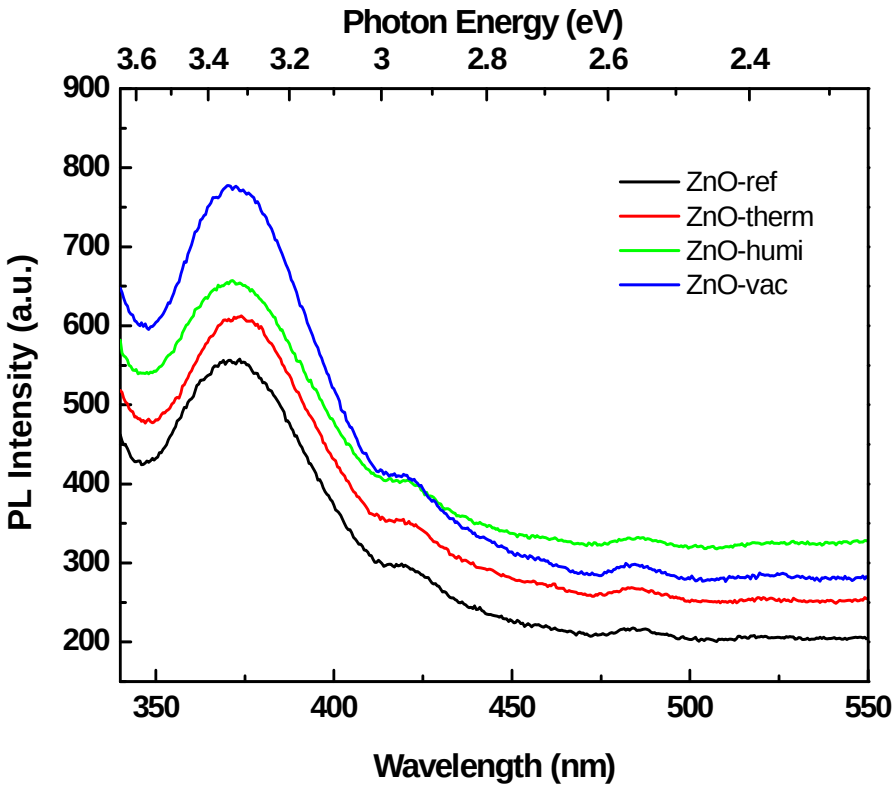

Figure 4.6 PL spectra of ZnO films without (A) and with thermal (B), humidity (C), and vacuum (D) post-treatments.

4.2.5 XPS measurement

In order to further understand the change in J_{sc} caused by post-treatments, x-ray photoelectron spectroscopy (XPS) measurements were carried out. All atomic spectra were calibrated by taking hydrocarbon C 1s peak at 284.6 eV as a reference. Fig. 4.7 shows core level XPS spectra of O 1s for the ZnO films with different post-treatments. The O 1s XPS spectra exhibit asymmetric line shapes as shown in Fig. 4.7. The main peak with lower binding energy (529.8eV) corresponds to oxygen lattice in ZnO matrix, while the other two peaks (at 531.1eV and 531.9 eV) correspond to the lattice oxygen in oxygen-deficient regions (oxygen vacancy) and zinc hydroxide ($Zn(OH)_2$), respectively [4.17, 4.18]. From Fig. 4.7, the decreased intensity of the

peak located near 531.9 eV infers that the zinc hydroxide component decreases with post-treatments due to conversion from metal hydroxide to oxides. From the fitting curves of the XPS spectra, the relative percentage contributed to the spectrum from zinc hydroxide component decreased from 13 % (ZnO layer without post-treatment) to 9.5%, 10%, and 9.7% for ZnO layer with thermal, humidity, and vacuum treatment, respectively. Therefore, the decreased metal hydroxide component and increased oxide lattices content in the ZnO films result in reduced defect sites. The possible explanation is that zinc hydroxide in the ZnO layer needs more energy to convert it into metal oxide lattices.

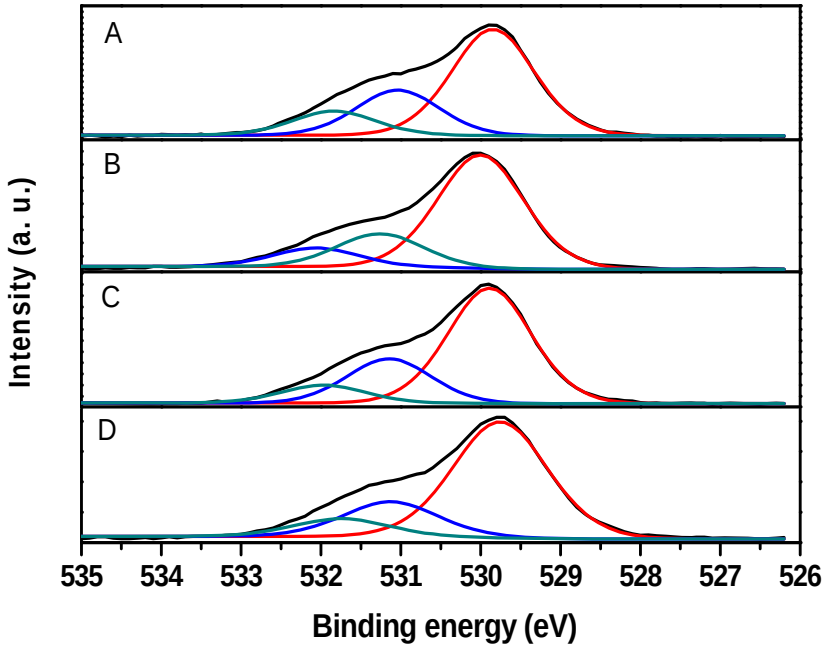

Figure 4.7 O 1s XPS spectra of ZnO films without (A) and with thermal (B), humidity (C), and vacuum (D) post-treatments.

4.2.6 Charge carrier mobility of ZnO film

To evaluate the charge transport properties of ZnO with various post-treatments, ZnO thin film transistors with bottom-gate top-contact structure were employed (Fig. 4.8 (a)). For the device fabrication, a heavily doped p-type Si wafer (purchased from Silicon Quest International, Inc.) was served as the gate electrode and 200 nm of thermally grown SiO_2 was used as the dielectric layer. Prior to spin coating ZnO precursors, the Si/SiO_2 substrates were firstly cleaned with acetone, IPA, and de-ionized water, and then treated with Ar plasma to facilitate the thin film formation. ZnO precursors were then spun coated at 3000 rpm for 30 s to get ZnO thin film around 10~15 nm. Following that, the substrates were pre-annealed at 150 ^{o}C for 10 min. Then the ZnO films underwent different post-treatments. Finally, Al layers, as the source and drain electrodes (W = 1000 μm, L = 100 μm), were deposited on the ZnO thin film with a shadow mask. The transistors were characterized with Keithley 4200 parameter analyzer in the N_2-filled glove box. The field-effect mobility of the fabricated transistor was extracted using the following equation in the saturation region from the gate sweep: $I_D = W/(2L)C_i\mu(V_G-V_T)^2$, where I_D is the drain current in the saturation region, μ is the field-effect mobility, C_i is the capacitance per unit area of the gate dielectric layer (SiO_2, 200 nm, C_i = 17 nF cm^{-2}), V_G and V_T are gate voltage and threshold voltage, and W and L are channel width and length, respectively.

As shown in Fig. 4.8, all the films underwent different post-treatments showed good transistor characteristics. The ZnO film with thermal post-treatment resulted in the best device performance with a μ_e of 0.36 cm^{2}V^{-1}s^{-1}, on/off ratio of 5 × 10^7, and threshold voltage (V_{th}) of 19 V. This result is in accord with the solar cell result,

which shows the lowest R_s and the highest J_{sc} (Table 4.1). The samples experienced humidity and vacuum treatment have charge carrier mobilities of 0.183 $cm^2V^{-1}s^{-1}$ and 0.311 $cm^2V^{-1}s^{-1}$, respectively.

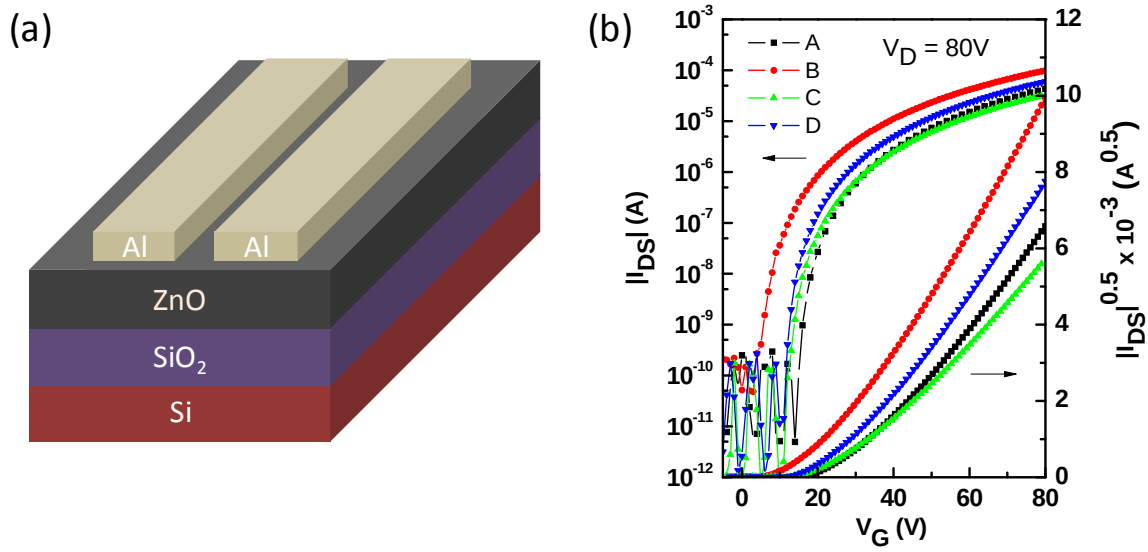

Figure 4.8 (a) The device structure used in this study. (b) The transfer characteristics of the ZnO films without (A) and with thermal (B), humidity (C), and vacuum (D) post-treatments.

4.2.7 Charge extraction

The capacitance – voltage ($C - V$) measurements were carried out in the dark at room temperature to explore the variation of the inverted OSC device performances, as shown in Fig. 4.9 [4.19]. The capacitance was measured against different biases, with AC excitation amplitude of 10 mV at a frequency of 10 kHz. For a schottky diode, the junction capacitance shows a bias dependence according to Mott-Schottky relation [4.20], $C^{-2} = 2(V_{bi}\text{-}V)/(A^2q\varepsilon\varepsilon_0N_A)$, where V_{bi} is the built-in potential, V is the applied voltage, A corresponds to the device active surface (0.09 cm^2), q accounts for

the elementary charge, ε is the relative dielectric constant of the semiconductors (assume to be 3), ε_0 the permittivity of the vacuum, and N_A the doping density. The built-in voltage (V_{bi}) could be estimated by the voltage corresponding to the maximal of capacitance which equals to the flat-band condition. From Fig. 4.9, we obtained the V_{bi} of 0.43 ± 0.02 V, 0.25 ± 0.02 V, and 0.39 ± 0.02 V, for thermal, humidity, and vacuum post-treatments, respectively. While the reference device without the post-treatment shows similar V_{bi} with humidity treated device (0.26 ± 0.02 V). The V_{bi} enhancement after the post-treatment indicates improved charge extraction, which could be a good evidence for the current density increase.

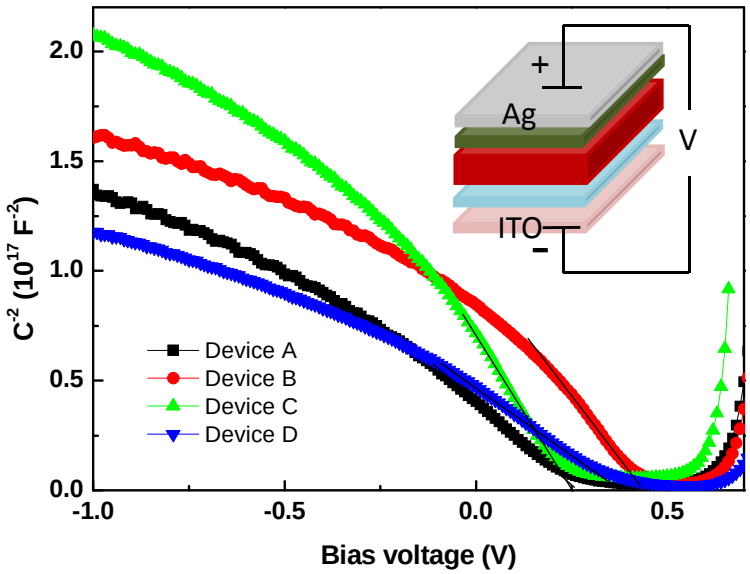

Figure 4.9 *C – V* characteristics of devices in the dark at room temperature, the corresponding devices were those based on ZnO films without (device A) and with thermal (device B), humidity (device C), and vacuum (device D) post-treatments.

In summary, inverted OSCs with low-temperature aqueous solution-processed ZnO buffer layers underwent different post-treatments have been investigated. The device performance has been optimized by the thermal and vacuum post-treatments.

Based on transmittance, PL, XPS and $C - V$ results, it was found that the post-treatments especially thermal and vacuum treatments, not only reduce the surface defect sites but also increase the film crystallinity compared to the reference film, which is responsible for the higher current density compared to the reference device.

4.3 Photo-stability of inverted OSCs based on different ESLs

In order to achieve the device commercialization of OSCs, most research works have been focused on two aspects: (1) the PCE enhancement due to the much lower PCE compared with inorganic solar cells; and (2) device air stability [4.21-4.23]. Device encapsulation is a good method to increase device air stability by preventing the cell from oxygen and moisture in the air ambient [4.24, 4.25]. However, there is another challenge for OSCs, the operational lifetime. Several groups have studied the OSC operational lifetime [4.26-4.28]. Hauch *et al.* reported flexible polymer solar cells with more than 1 year operational lifetime [4.26]. However, the cell PCE was not high (~ 1%). Zimmermann *et al.* has presented completely inverted OSCs with 1500 h operational lifetime by inserting titanium (Ti) or chromium (Cr) layer between Al cathode and active layer, and the cell PCE was about 1.5 – 3% [4.27]. Katz *et al.* reported a method of relevant accelerated tests of operational lifetime [4.28]. The cells were treated with ~ 4 Suns concentrated light for 100 min illumination, and comparisons of V_{oc} and fill factor (FF) between fresh cells and graded cells based on ZnO nanoparticle buffer layers were recorded.

For ZnO layer, surface defects can act as trap-assistant recombination center [4.29]. When ZnO layer is under UV-illumination, oxygen desorption occurs and the release of oxygen induces a highly n-doped ZnO layer [4.28]. This highly n-doped

ZnO layer has a narrow bandwidth which can be easily tunneled by both electrons and holes, so the ZnO capability to act as an electron selective layer is reduced. This phenomenon causes OSC device with the ZnO layer degraded with UV-illumination easily.

For TiO_x layer, the work-function of ITO/TiO_x surface has a little increase compared with the bare ITO surface, which causes a schottky contact formed with the active layer [4.30]. This barrier blocks the electrons' transport to the cathode, resulting in a hole-only device and an S-shaped formed in the $J - V$ curve measured. The work function has a blue shift after UV-illumination by surface band binding and the S-shape is eliminated by the UV-illumination (light soaking) [4.30]. However, during this process, a harmful photo-oxidation in the organic active layer occurs, which also causes the device degradation.

Riedl *et al.* reported the performance of devices based on atomic layer deposited (ALD) ZnO, TiO_x, Al doped ZnO and their combination bilayers [4.30]. It was found that the light soaking problem is due to the interface effect rather than bulk electrical properties. Lim *et al.* reported the performance of devices based on solution processed ZnO and ALD deposited TiO_x bilayer [4.31]. The device performance was improved compared with the bare ZnO layer because the ZnO layer surface was passivated by the ALD deposited TiO_x layer. However, the photo-stability of devices based on aqueous solution processed ZnO, sol-gel processed TiO_x and their combination bilayers still need further investigation. Here, the photo-induced degradation of devices based on solution processed TiO_x, ZnO and their bilayer structures in inverted architecture was studied and compared. The device performance, the light soaking problem for TiO_x layer, and the photo-degradation of V_{oc} and FF

under different light intensities and time duration up to 20 min were measured and analyzed.

4.3.1 Performance of devices based on different ESLs

The TiO_x solution was spin-coated on top of ITO substrates at 4000 rpm for 1min and the formed TiO_x films were immediately annealed at 150 °C for 10 min. For the TiO_x/ZnO (or ZnO/TiO_x) bilayer preparation, the ZnO (or TiO_x) layer was deposited and annealed as the bare ZnO (or TiO_x) film after TiO_x (or ZnO) layer deposited on ITO substrate and annealed.

Fig. 4.10 shows the $J - V$ characteristics of four types of inverted devices with ESLs of ZnO, TiO_x, TiO_x/ZnO and ZnO/TiO_x, and the corresponding extracted device parameters are summarized in Table 4.2. As shown in Fig. 4.10 (a), the devices using the bilayer ESLs show better performance than the devices with bare ZnO or TiO_x ESL. Both V_{oc} and J_{sc} have been improved. The significant increase of J_{sc} for the device based on ZnO/TiO_x bilayer film compared with the bare ZnO film was attributed to the reduced surface recombination by surface passivation [4.31]. For the device based on TiO_x/ZnO bilayer, the possible explanation for the improved device performance compared with the bare TiO_x film was due to the reduced series resistance and enhanced hole blocking capability.

Fig. 4.10 (c) shows $J - V$ characteristics of inverted cells with TiO_x and ZnO/TiO_x ESLs before and after light soaking. The $J - V$ curves of both devices contained a kink before light soaking. For the bare TiO_x device, after light soaking for 10 min, a PCE of 2.9 % could be achieved with a short-circuit current density of 9.97

mA/cm^2, an open-circuit voltage of 0.55 V, and a fill factor of 0.53. The combination of ZnO and TiO_x layer (ZnO/TiO_x bilayer) not only reduces the light soaking time to 2 min, but also enhances J_{sc} (10.25 mA/cm^2) and V_{oc} (0.57 V) simultaneously, which results in higher PCE.

However, when a ZnO film was deposited on TiO_x layer (TiO_x/ZnO bilayer), the S-shape in the $J - V$ curve can be eliminated, as shown in Fig. 4.9 (a). The eliminated S-shape is due to the ohmic contact formed between ZnO and active layer. The UPS measurement (Fig. 4.11) shows that the ITO/ZnO and ITO/TiO_x/ZnO films have similar surface work-functions, and has a decrease of about 0.5 eV compared with the bare ITO surface. However, the ITO/TiO_x film has slightly larger surface work-function than the bare ITO surface.

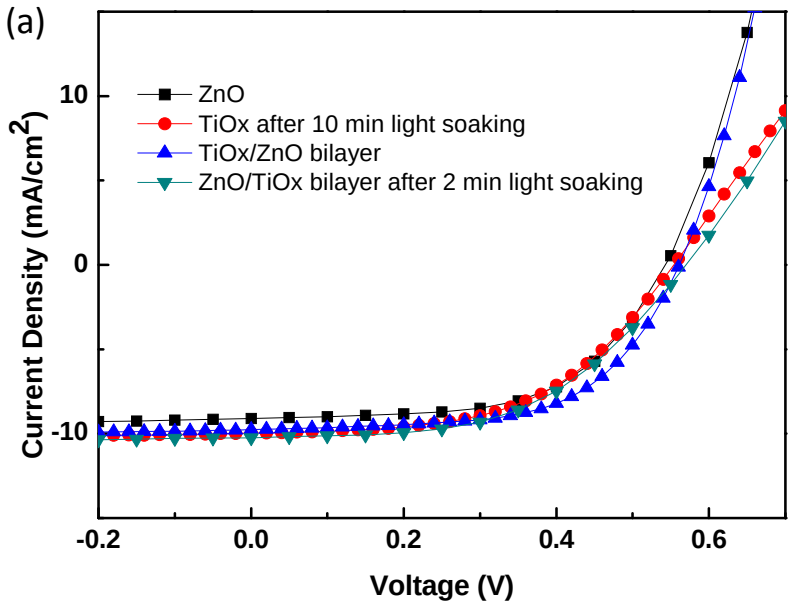
(a)
ZnO
TiOx after 10 min light soaking
TiOx/ZnO bilayer
ZnO/TiOx bilayer after 2 min light soaking
Current Density (mA/cm2)
10
0
-10
-0.2
0.0
0.2
0.4
0.6
Voltage (V)

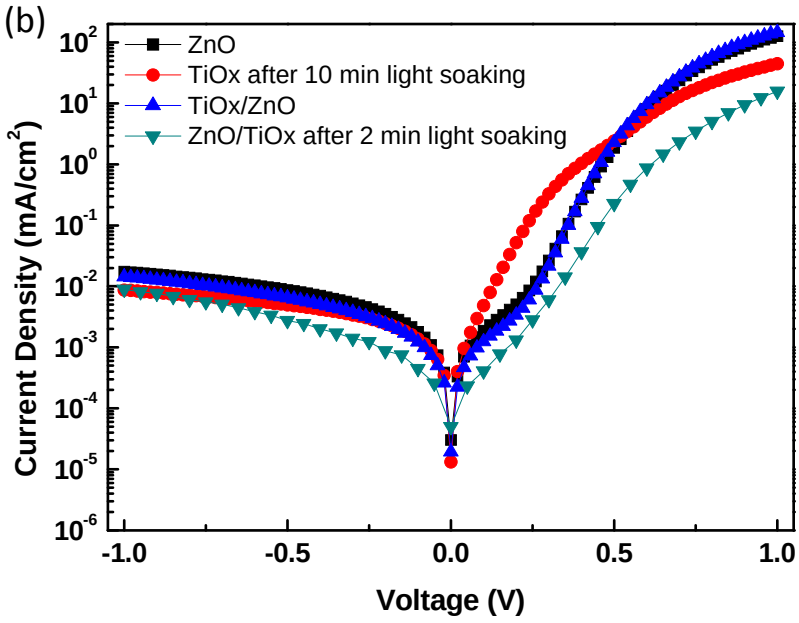
(b)
ZnO
TiOx after 10 min light soaking
TiOx/ZnO
ZnO/TiOx after 2 min light soaking
Current Density (mA/cm2)
10^2
10^1
10^0
10^-1
10^-2
10^-3
10^-4
10^-5
10^-6
-1.0
-0.5
0.0
0.5
1.0
Voltage (V)

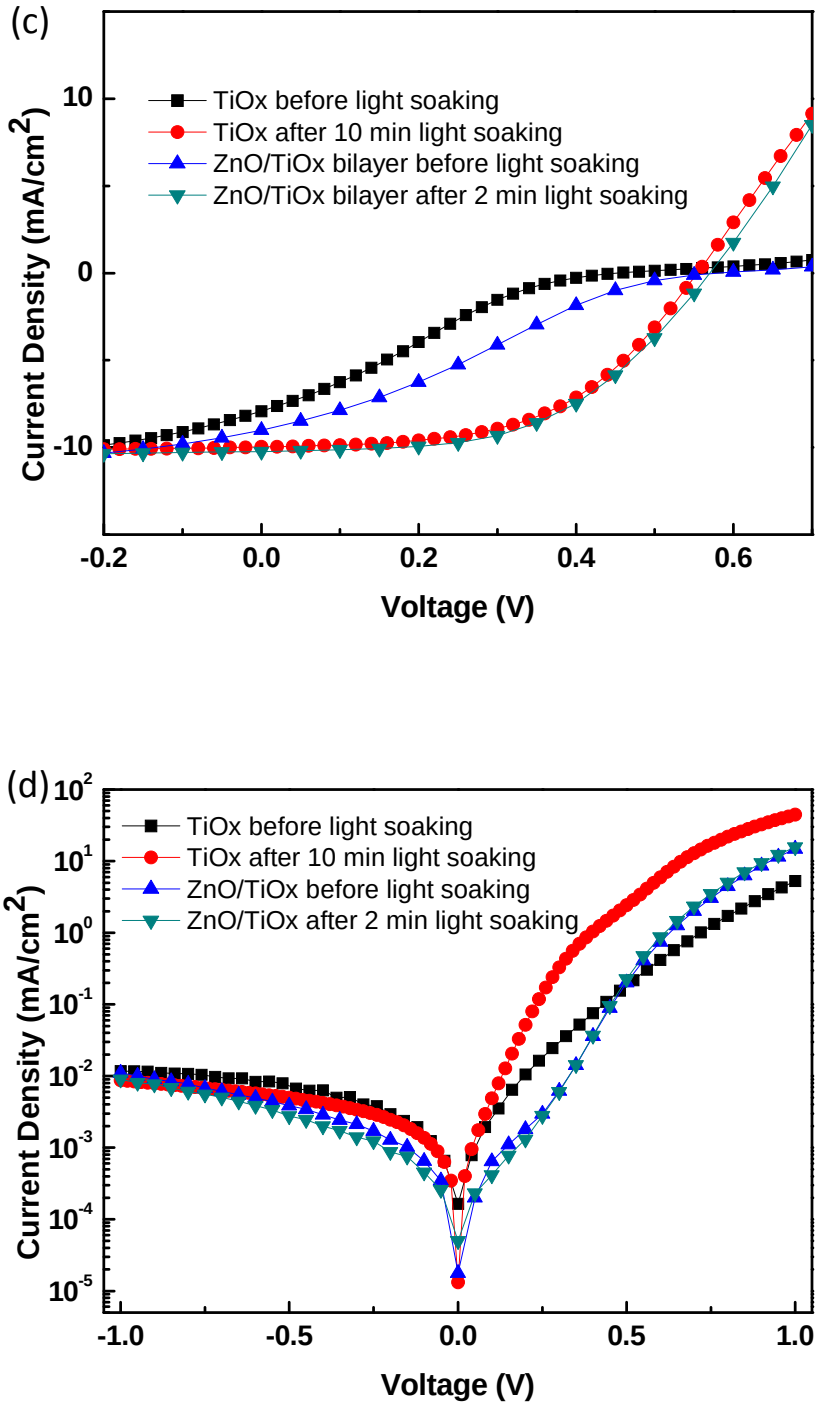

Figure 4.10 (a) $J - V$ characterisctics of inverted P3HT:$PC_{61}BM$ solar cells incorporating different ESLs under (a) illumination and dark; $J - V$ characterisctics of inverted P3HT:$PC_{61}BM$ solar cells incorporating with TiO_x and ZnO/TiO_x ESLs before and after light soaking under (c) illumination and (d) dark.

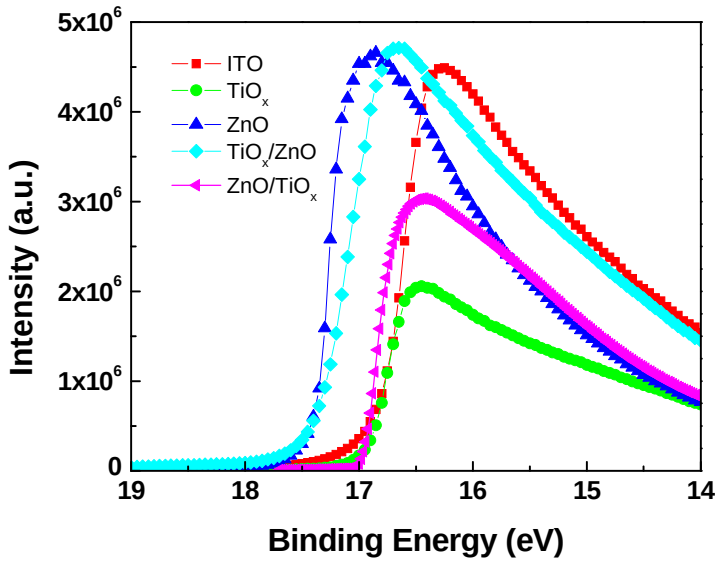

Figure 4.11 UPS spectra of TiO_x, ZnO, ZnO/TiO_x and TiO_x/ZnO deposited on top of ITO film and bare ITO film.

Table 4.2 Device photovoltaic performance parameters of inverted P3HT:$PC_{61}BM$ solar cells incorporating ZnO, TiO_x, TiO_x/ZnO and ZnO/TiO_x as the electron transport layers.

	Conditions	J_{sc} (mA/cm^2)	V_{oc} (V)	FF	η (%)	R_s (Ω/cm^2)	R_{sh} (Ω/cm^2)
1	ZnO	9.10	0.542	0.58	2.86	10.5	1000
2	TiO_x	9.97	0.554	0.53	2.92	16.3	1125
3	TiO_x/ZnO	9.77	0.561	0.60	3.28	15	1285
4	ZnO/TiO_x	10.25	0.570	0.52	3.04	17.2	1333

The optical and morphological properties of each ESL deposited on ITO/glass substrate have also been investigated. The transmittances of the ESL films have been shown in Fig. 4.12. It can be seen that TiO_x layer has better transmittance than ZnO layer, and the transmittance of ZnO and TiO_x single layer was better than those after deposited with another type of layer. The surface roughness of each electrode has also been characterized by AFM, as shown in Fig. 4.13. The RMS values of surface roughness were 3.99 nm, 2.36 nm, 4.12 nm, 1.3 nm and 2.5 nm for bare ITO, ITO/ZnO, ITO/TiO_x, ITO/TiO_x/ZnO, ITO/ZnO/TiO_x, respectively.

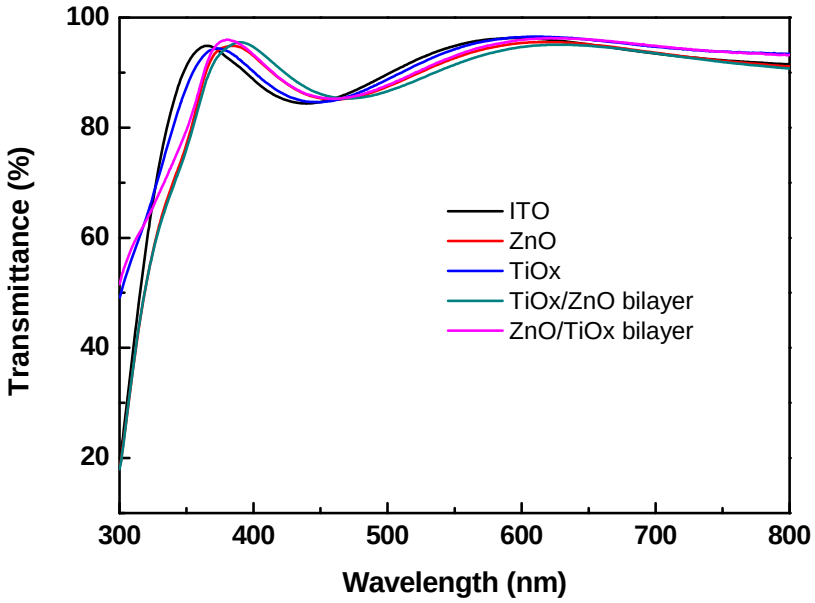

Figure 4.12 Transmittance of TiO_x, ZnO, ZnO/TiO_x and TiO_x/ZnO films deposited on top of ITO film and bare ITO film.

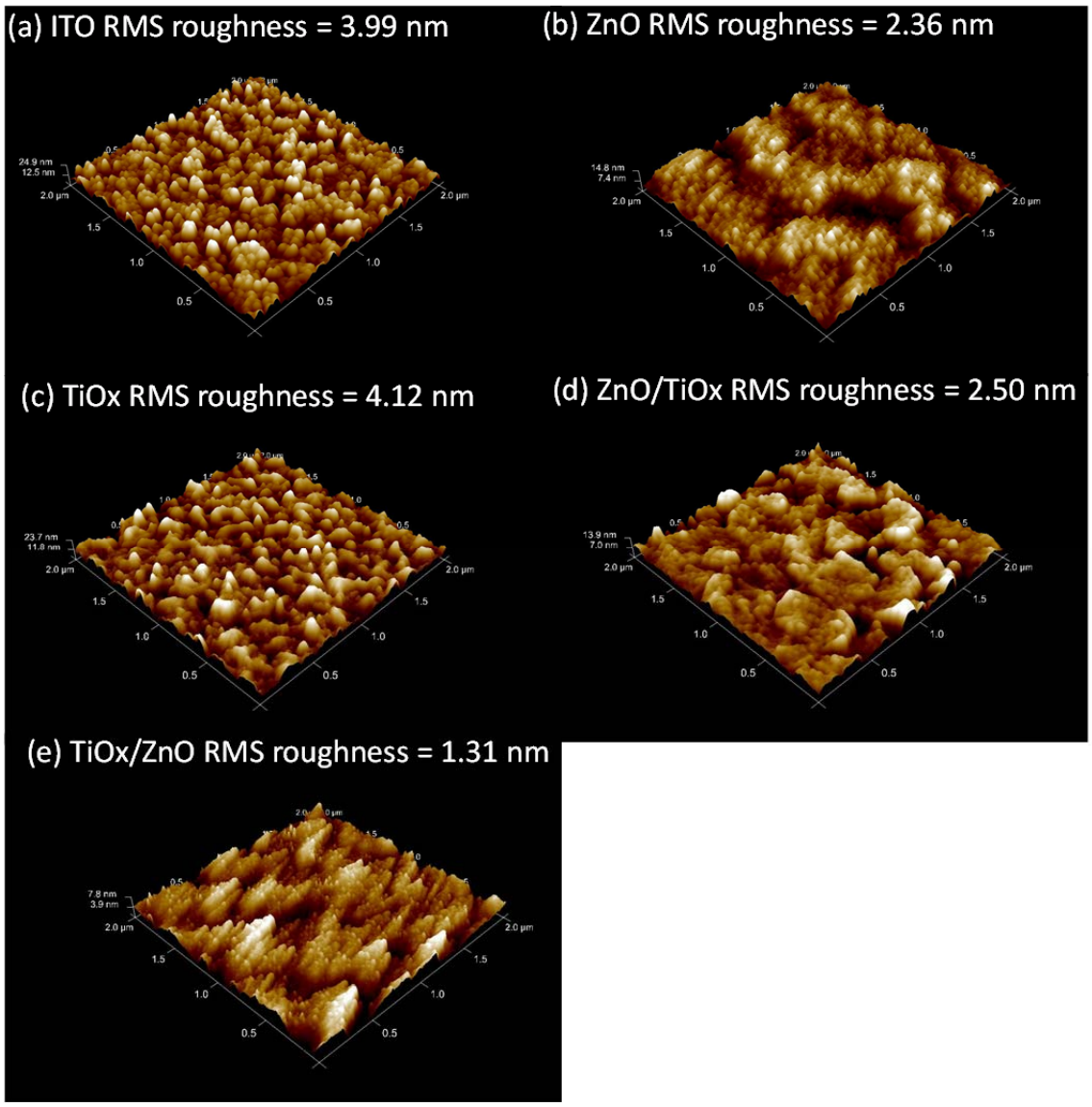

Figure 4.13 AFM images of (a) bare ITO film, and (b) TiO_x, (c) ZnO, (d) ZnO/TiO_x and (e) TiO_x/ZnO films deposited on top of ITO films.

4.3.2 Photo-stability of devices based on different ESLs

In order to investigate the device operational lifetime, the devices were kept under illumination and measured periodically to observe the illumination effect on the device performance. Fig. 4.14 (a) to 4.14 (d) show the periodic $J - V$ curve measurements for the devices based on different ESLs under illumination for 20 min and Fig. 4.13 (e) shows the change of normalized V_{oc} with the illumination time being

increased. It can be seen that the performance of all the devices decreases with the illumination time, especially V_{oc} values of the devices. From Fig. 4.13 (e), it shows that V_{oc} of the device based on ZnO-only ESL has a most rapid and significant decrease than other ESLs. After 20 min illumination, only 89 % of the original V_{oc} value remains. However, for the device based on ZnO/TiO_x ESL, the remaining V_{oc} value was as high as 98.3 %. It also can be observed that V_{oc} of the devices based on TiO_x layer contacted with active layer decreases slowly than the ZnO layer contacted with active layer. Meanwhile, compared with devices based on bare ZnO (or TiO_x) film, the devices based on ZnO (or TiO_x) with TiO_x (or ZnO) layer prior deposited had better photo-stability.

The light intensity dependence of the device performance has also been investigated. The $J - V$ characteristics of the device performance with different light intensities has been measured and shown in Fig. 4.14. The in semi-logarithmic was also plotted (insets of Fig. 4.14), and Fig. 4.14 (e) shows the light intensity dependence of normalized V_{oc}. Since $V_{oc} \approx (nkT/q)\ln(I_{sc}/I_o) = (nkT/q)\ln(C) + \text{constant}$, where n, k, T, q, I_o and C are the ideality factor, the Boltzmann constant, the temperature, the electron charge, the photocurrent and the concentration of the sunlight delivered to the cell, respectively [4.32]. From this equation, the value of n can be estimated by the slope of $(nkT/q)\ln(C)$. From Fig. 4.14 (e), it can be observed that $n_{ZnO} > n_{TiOx/ZnO} > n_{TiOx} > n_{ZnO/TiOx}$. The ideality factor is a good tool to analyze the transport and recombination process. Higher ideality factor extracted from V_{oc} means larger shunting effect caused by higher trap-assisted recombination [4.33].

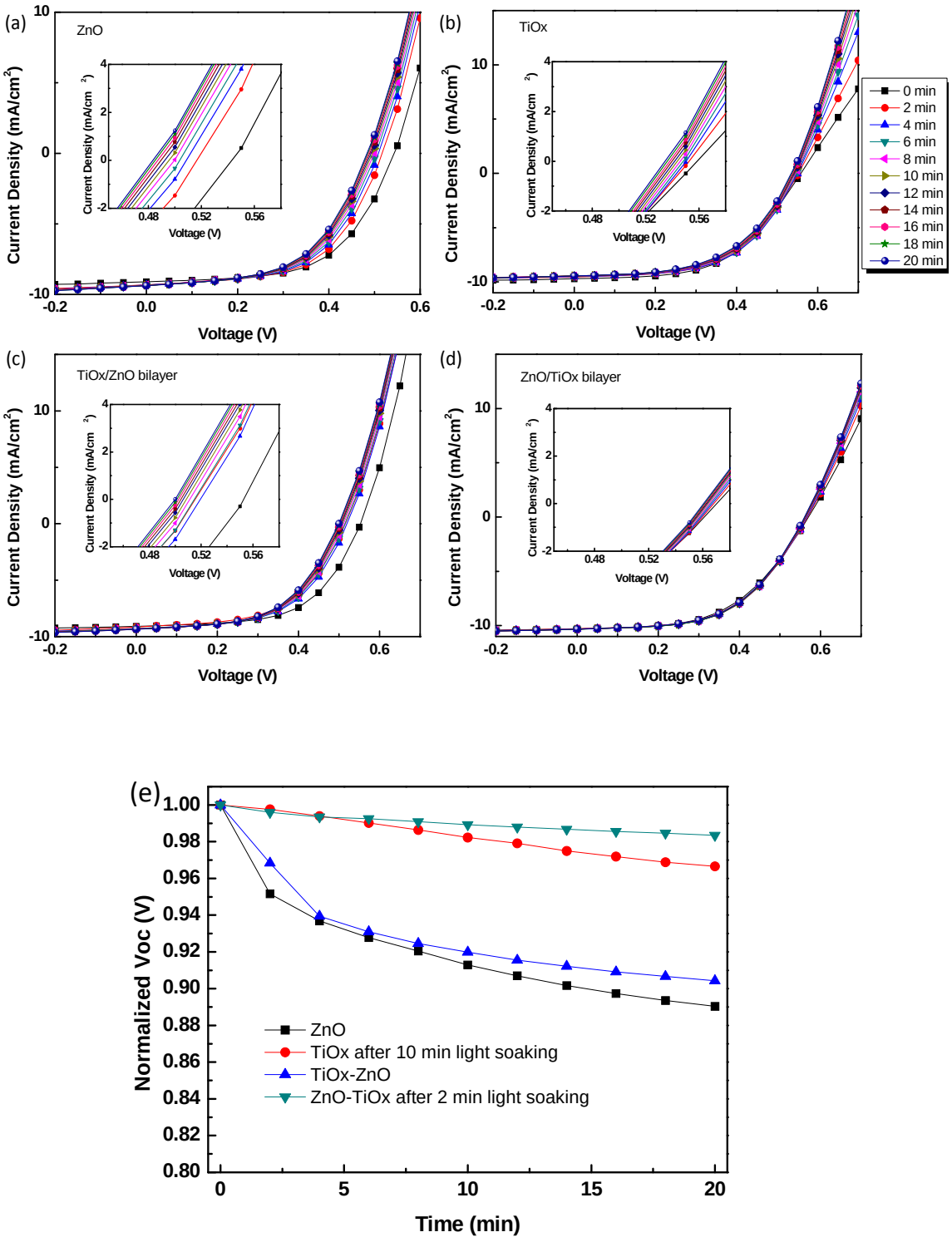

Figure 4.13 Periodic $J - V$ curve measurements for the devices based on (a) ZnO, (b) TiO_x, (c) TiO_x/ZnO and ZnO/TiO_x ESLs under illumination for 20 min; (e) the change of normalized V_{oc} with the illumination time being increased.

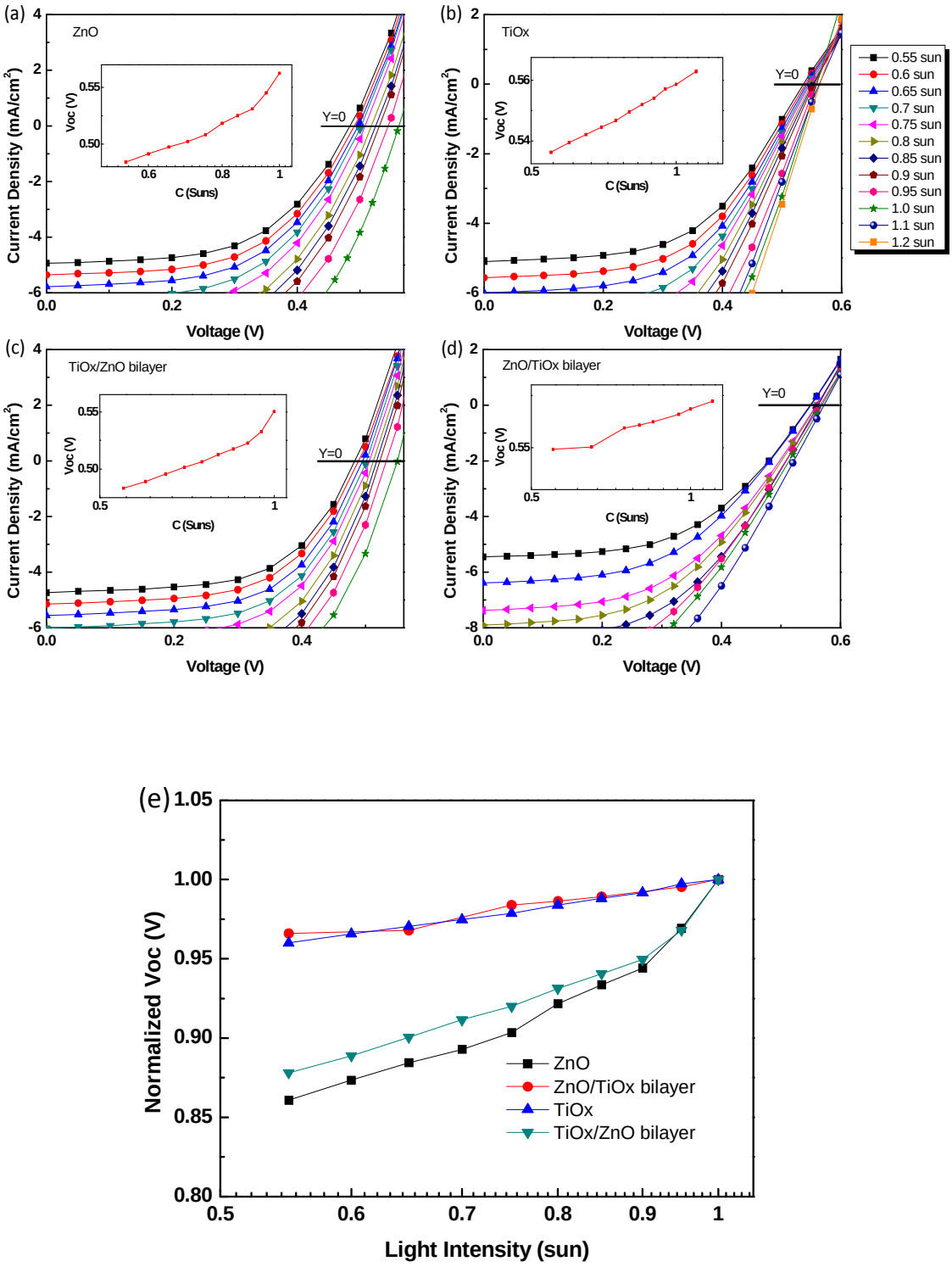

Figure 4.14 $J - V$ characteristics of the device performance with different light intensities for devices based on (a) ZnO, (b) TiO_x, (c) TiO_x/ZnO and (d) ZnO/TiO_x ESLs; (e) the light intensity dependence of normalized V_{oc}.

The possible physical mechanism of shunting effect for the device based ZnO film has already been reported [4.30]. The oxygen desorption in ZnO layer under illumination induces a narrow bandwidth, which reduces the ZnO capability to act as ESL. However, when an additional TiO_x film was added, the TiO_x layer was contacted with active layer and played the hole blocking role. Meanwhile, since the oxygen desorption process is reversible, which means the ambient oxygen will be re-adsorbed by the ZnO surface, when TiO_x layer was deposited on top of ZnO film, the oxygen in TiO_x film could be adsorbed by ZnO surface, leading to a lower TiO_x work-function. This could be the possible explanation for the reduced light soaking time of device based on ZnO/TiO_x film compared with the bare TiO_x film.

4.4 Summary

In this chapter, firstly, we optimized the ZnO buffer layer fabrication process of inverted OSCs to obtain the maximum device PCE. Effects of different post-treatments (thermal, humidity, and vacuum) of aqueous solution processed ZnO buffer layer on device performance in terms of surface structure and properties were investigated. The surface properties of the ZnO buffer layers with thermal, humidity (RH 80%), and vacuum post-treatment were investigated by TM-AFM, UV-Vis spectroscopy, PL, and XPS measurements. It was found that the thermal and vacuum post-treatments not only reduce the surface defect sites but also increase the films crystallinity compared to the reference film. Based on P3HT:$PC_{61}BM$ system, devices with the ZnO buffer layer which underwent thermal and vacuum post-treatments were found to exhibit the higher average PCE 3.58% and 3.51%, and the highest short circuit current density (J_{sc}), 10.29 mA/cm^2 and 9.92 mA/cm^2, respectively.

Meanwhile, based on the optimized ZnO layer subjected to thermal post-treatment, a high PCE of 7.1% was obtained from an inverted OSC with PTB7:$PC_{71}BM$ active layer.

Photo-stability and performance of devices with different metal oxides ESLs were also studied. Photo-induced degradation is a big obstacle for the commercialization of OSCs. Due to the shunts generation and degeneration in ZnO layer, a significant degradation of V_{oc} has been observed for the device based on ZnO layer by periodic measurements of $J - V$ curves with 20 min illumination. For the device based on TiO_x layer, a UV-induced band binding on TiO_x layer surface occurs to remove the schottky barrier caused by high surface work-function of ITO/TiO_x layer, which causes a harmful photo-oxidation in the organic active layers. Due to the oxygen re-adsorption process in ZnO layer and excess of oxygen property in TiO_x layer, TiO_x and ZnO layers were combined and applied as ESL in inverted OSCs. The device $J - V$ curves with 20 min illumination and different light intensities have been both measured. It was found that the device based on TiO_x/ZnO had better device performance and the device based on ZnO/TiO_x layer had better device photo-stability.

References

[4.1] H. Cheun, C. Fuentes-Hernandez, Y. Zhou, W. J. Potscavage, S.-J. Kim, J. Shim, A. Dindar and B. Kippelen, Journal of physics Chemistry C 114, 20713 – 20718 (2010).

[4.2] H. Sun, J. Weickert, H. C. Hesse and L. Schmidt-Mende, Solar Energy Materials and Solar Cells 95, 3450 – 3454 (2011).

[4.3] F. C. Krebs, T. D. Nielsen, J. Fyenbo, M. Wadstrom and M. S. Pedersen, Energy Environmental Science 3, 512 – 525 (2010).

[4.4] Y. Sun, J. H. Seo, C. J. Takacs, J. Seifter and A. J. Heeger, Advanced Materials 23, 1679 – 1683 (2011).

[4.5] A. K. K. Kyaw, X. W. Sun, C. Y. Jiang, G. Q. Lo, D. W. Zhao and D. L. Kwong, Apploed Physics Letters 93, 221107 (2008).

[4.6] S. K. Hau, H. L. Yip, N. S. Baek, J. Zou, K. O'Malley and A. K. Y. Jen, Applied Physics Letters 92, 253301 (2008).

[4.7] C. Pacholski, A. Kornowski and H. Weller, Angewandte Chemie International Edition 41, 1188 – 1191 (2002).

[4.8] S. Meyers, J. Anderson, C. Hung, J. Thompson, J. Wager and D. Keszler, Journal of the American Chemistry Society 130, 17603 – 17609 (2008).

[4.9] Y. Ka, E. Lee, S. Y. Park, J. Seo, D. -G. Kwon, H. H. Lee, Y. Park, Y. S. Kim and C. Kim, Organic Electronics 14, 100 – 104, (2013).

[4.10] S. Bai, Z. Wu, X. Xu, Y. Jin, B. Sun, X. Guo, S. He, X. Wang, Z. Ye, H. Wei, X. Han and W. Ma, Applied Physics Letters 100, 203906, (2012).

[4.11] S. T. Tan, B. J. Chen, X. W. Sun and W. J. Fan, Journal of Applied Physics 98, 013505 (2005).

[4.12] J. Tauc, Amorphous and Liquid Semiconductors (Plenum, London, 1974).

[4.13] E. A. David and N. F. Mott, Philosophical Magazine 22, 903 – 922 (1970).

[4.14] M. H. Huang, Y. Wu, H. Feick, N. Tran, E. Weber and P. Yang, Advanced Materials 13, 113 – 116, (2011).

[4.15] K. Vanheusden, W. L. Warren, C. H. Seager, D. R. Tallant, J. A. Voigt and B. E. Gnade, Journal of Applied Physics 79, 7983 – 7990 (1996).

[4.16] G. Adamopoulos, A. Bashir, W. P. Gillin, S. Georgakopoulos, M. Shkunov, M. A. Baklar, N. Stingelin, D. D. C. Bradley, and T. D. Anthopoulos, Advanced Functional Materials 21, 525 – 531 (2011).

[4.17] J. C. C. Fan and J. B. Goodenough, Journal of Applied Physics 48, 3524 – 3531 (1977).

[4.18] S. Jeong, Y. -G. Ha, J. Moon, A. Facchetti and T. J. Marks, Advanced Mateials 22, 1346 – 1350 (2010).

[4.19] J. C. Wang, X. C. Ren, S. Q. Shi, C. W. Leung and P. K. L. Chan, Organic Electronics 12, 880 – 885 (2011).

[4.20] P. W. M. Blom, V. D. Mihailetchi, L. J. A. Koster, and D. E. Markov, Advanced Materials 19, 1551 – 1566 (2007).

[4.21] Y. Sun, C. J. Takacs, S. R. Cowan, J. H. Seo, X. Gong, A. Ray and A. J. Heeger, Advanced Materials 23, 2226 – 2230 (2011).

[4.22] T. Hu, F. Li, K. Yuan and Y. Chen, ACS Applied Materials and Interfaces 5, 5763 – 5770 (2013).

[4.23] M. J. Tan, S. Zhong, J. Li, Z. Chen and W. Chen, ACS Applied Materials and Interfaces 5, 4696 – 4701 (2013).

[4.24] W. J. Potscavage, S. Yoo, B. Domercq, B. Kippelen, Applied Physics Letters 90, 253511 (2007).

[4.25] S. Sarkar, J. H. Culp, J. T. Whyland, M. Garvan and V. Misra, Organic Electronics 11, 1896 – 1900 (2010).

[4.26] J. A. Hauch, P. Schilinsky, S. A. Choulis, R. Childers, M. Biele and C. J. Brabec, Solar Energy Materials and Solar Cells 92, 727 – 731 (2008).

[4.27] B. Zimmermann, U. Würfel and M. Niggemann, Solar Energy Materials and Solar Cells 93, 491 – 496 (2009).

[4.28] A. Manor, E. A. Katz, T. Tromholt and F. C. Krebs, Advanced Energy Materials 1, 836 – 843 (2010).

[4.29] C.-H. Hsieh, Y.-J. Cheng, P.-J. Li, C.-H. Chen, M. Dubosc, R.-M. Liang and C.-S. Hsu, Journal of the American Chemistry Society 132, 4887 – 4893 (2010),.

[4.30] S. Trost, K. Zilberberg, A. Behrendt, A. Polywka, P. Görrn, P. Reckers, J. Maibach, T. Mayer and T. Riedl, Advanced Energy Materials, DOI: 10.1002/aenm.201300402 (2013).

[4.31] H. O. Seo, S.-Y. Park, W. H. Shim, K.-D. Kim, K. H. Lee, M. Y. Jo, J. H. Kim, E. Lee,D.-W. Kim, Y. D. Kim and D. C. Lim, Journal of Physical Chemistry C 115, 21517 – 21520 (2011).

[4.32] T. Tromholt, E. A. Katz, B. Hirsch, A. Vossier and F. C. Krebs, Applied Physics Letters 96, 073501 (2010).

[4.33] G. A. H. Wetzelaer, M. Kuik, M. Lenes and P. W. M. Blom, Applied Physics Letters 99, 153506 (2011).

Chapter 5

PEI:PSS as Cathode Interfacial Layer in Inverted OSCs

5.1 Introduction

Inverted structural polymer solar cells (PSCs) [5.1-5.3], which use indium-tin-oxide (ITO) substrate as the cathode and a high-work-function metal such as silver or gold as the top anode, have been considered as an advantageous approach for improving the cells' air stability. Usually, an additional interfacial layer between the ITO cathode and organic active layer is introduced in an inverted PSC. This is because that the high work-function of the bottom ITO cathode usually hampers the formation of ohmic contact for electron transport from the active layer to the ITO cathode when the blends of poly(3-hexylthiophene) (P3HT) and phenyl-C61-butyric acid methylester ($PC_{61}BM$) are used for the active layers. A barrier to electron extraction is usually formed if the high work-function ITO is in contact with n-type organic semiconductor such as PCBM. Thus, an interfacial layer is added in between the ITO cathode and the active layer to decrease or eliminate the electron-extraction barrier [5.4-5.11].

In Chapters 3 and 4, inorganic metal oxides, zinc oxide (ZnO) and titanium oxide (TiO_x), have been investigated and applied for the interfacial layer in inverted PSCs, due to their high transparency, efficient electron extraction and hole blocking capability. However, there are intrinsic limitations in these devices with metal oxides

as the interfacial layer, such as the high rate of trap-assisted recombination in the interfacial layer [5.12, 5.13], and inherent incompatibility between the inorganic metal oxides and organic active layer [5.14-5.16]. Meanwhile, devices with ZnO film as the buffer layer usually suffer a significant photo-induced degradation during the exposure of light [5.17], and devices with TiO_x film as the buffer layer usually need post-UV treatment to improve the performance which causes a harmful photo-oxidation in the organic active layers [5.6]. All these limitations hinder the further improvements in cell performance and device lifetime of inverted PSCs.

To avoid these weaknesses of the metal-oxide interfacial layers, alcohol-water-soluble polymer-based materials, such as poly[(9,9-bis(3'-(N,N-dimethylamino)propyl)-2,7-fluorene)-alt-2,7-(9,9-dioctyfluorene)] (PFN) [5.9], poly(ethylene oxide) (PEO) [5.10], polyallylamine (PAA) [5.11] and polyethylenimine (PEI) [5.11], have been employed to form the interfacial layer on ITO for inverted PSCs. These polymer layers can lower the work-function of ITO cathode and facilitate the collections of photo-generated charge carriers by forming interfacial dipoles [5.18, 5.19]. These polymers are electrical insulators with large bandgap, thus should not be considered as a thin film of charge-injection layer but as surface modifier. However, most of the conjugated polyelectrolytes are unstable or complicated to synthesis, while nonconjugated polyelectrolyte like PEI is cost-effective and stable in aqueous solutions, and suitable for simple solution process at low temperature, which is desirable for large-area printing solar cells. However, the bare PEI polymer is insulting with very low conductivity, thus the PEI interfacial layer produces high series resistance in inverted solar cells, resulting in typically low current density. Therefore, the conductivity improvement of the PEI interfacial layer is desirable for developing highly efficiency solar cells.

In this Chapter, we demonstrated a high performance cathode interfacial layer for realizing PSC with higher efficiency and better stability using a water-soluble branched polyetherimine:poly(styrene sulfonate) sodium salt (PEI:PSS) polyelectrolyte complex. The conjugated anionic polyelectrolyte PSS is introduced into the material system to well tune the solution PH value, imine protonation ability, and film electronic properties. It was found that the PEI:PSS interfacial layer could enhance the built-in potential across the device due to the increased interface dipole. The interfacial layers with different PEI:PSS ratios were investigated, and it was found that at a proper ratio, the work-function of ITO electrode could decrease by 0.42 ~ 0.9 eV. Compared to ZnO or PEI-only interlayer, the PEI:PSS interlayer results in significantly increased photocurrent, which could be ascribed to the improved imine protonation, and forming cation/anion ionic polyelectrolytes. When PEI:PSS ratio equals to 1:0.3, the highest power conversion efficiency (PCE) of 3.68% was obtained from the P3HT:$PC_{61}BM$ based cell and a PCE of 5.02 % for poly[[9-(1-octylnonyl)-9H-carbazole-2,7-diyl]-2,5-thiophenediyl-2,1,3-benzothiadiazole-4,7-diyl-2,5-thiophenediyl]: phenyl-C71-butyric acid methyl ester (PCDTBT: $PC_{71}BM$) based cell. When a TiO_x/PEI:PSS bilayer configuration was used as the electron selective layer, the device performance was further enhanced to 3.9 % (P3HT/$PC_{61}BM$ based cell) and 5.34 % (PCDTBT: $PC_{71}BM$ based cell). Furthermore, the post-UV light treatment, which is usually needed for TiO_x based cell, could be avoided. The high performance TiO_x/PEI:PSS based cells demonstrates a promising cathode configuration for realizing high efficiency and long lifetime PSCs.

5.2 Performance of devices based on PEI:PSS with different ratios

The PEI:PSS solutions with different ratios were prepared as described in section 2.2.3 and the inverted OSC fabrication process was described in section 2.2.2. Fig. 5.1 (a) and (b) illustrate the schematic device structure and the energy diagrams for flat band conditions at the ITO/PEI:PSS/active layer junction with the PEI:PSS interfacial layer, respectively.

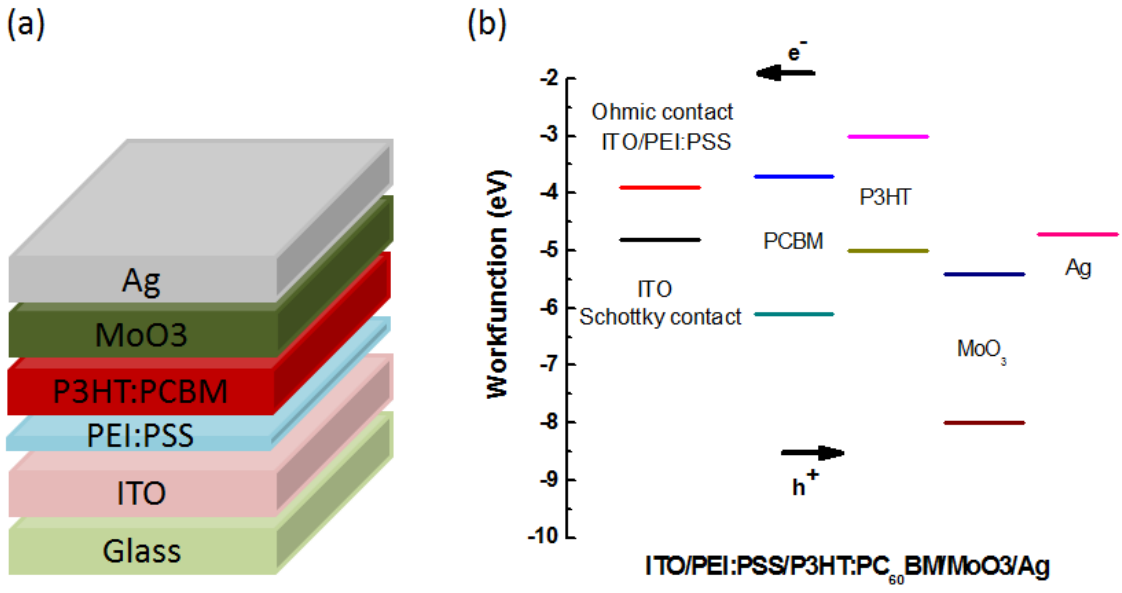

Figure 5.1 (a) The device structure of the inverted P3HT:$PC_{61}BM$ solar cell; (b) energy diagrams for flat band conditions with and without the PEI:PSS interfacial layer.

5.2.1 XPS measurement

When PEI:PSS aqueous solutions are deposited on ITO films, the positively charged amines (protonated amines) of PEI:PSS interact strongly with the negatively charged terminal oxygen ions of the ITO surface, thus the existence of protonated

amines is the key factor to affect the work-function of the cathode and hence the device performance [5.11, 5.20, 5.21]. The XPS measurements were carried out to analyze the surfaces of the cathode configurations of bare-ITO, ITO/PEI and ITO/PEI:PSS with different ratios (PEI:PSS=1:0.1, 1:0.3, 1:0.5, 1:0.8 and 1:1). Fig. 5.2 (a) and (b) show the survey and high-resolution XPS spectra of these cathode configurations. It is clearly shown that the N 1s peaks exhibit at the binding energy of 399.5 eV and 401 eV, which are corresponding to the nitrogen atom in neutral amines and protonated amines [5.22-5.24], respectively. The $[N^+]/[N]$ ratio of each cathode has been quantitatively analyzed (shown in Fig. 5.2 (c)) since the intensity of the electrostatic dipole on the cathode surface is mainly determined by the concentration of protonated amines [5.11]. It can be seen that all the ITO/PEI:PSS films have higher $[N^+]/[N]$ ratios compared with ITO/PEI. The $[N^+]/[N]$ increases firstly with the PSS content, reaching to the maximum when the PEI:PSS ratio is 1:0.8, and then decreases with further increase of the PSS content. Due to the increased $[N^+]/[N]$ ratio, the binding energy of the N 1s peaks shifts to the higher value. However, there is a kink which occurs in the $[N^+]/[N]$ ratio when the PEI:PSS is 1:0.5. A higher $[N^+]/[N]$ ratio means that it is more easily for the protonated amines in the ITO/PEI:PSS cathode to be distributed on ITO surface, which can induce larger work-function to decrease.

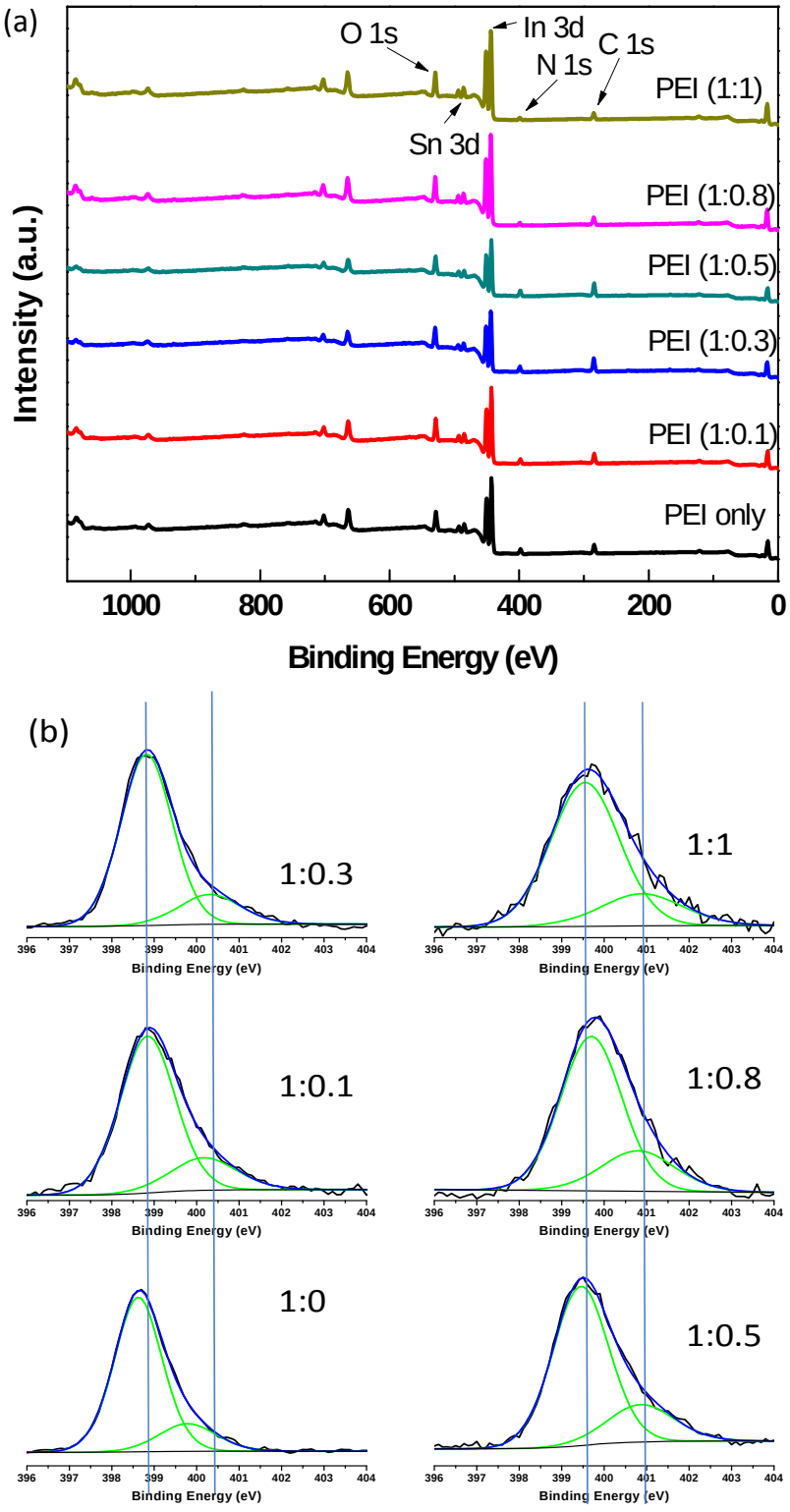
(a)
O 1s
In 3d
C 1s
N 1s
Sn 3d
PEI (1:1)
PEI (1:0.8)
PEI (1:0.5)
PEI (1:0.3)
PEI (1:0.1)
PEI only
Intensity (a.u.)
1000
800
600
400
200
0
Binding Energy (eV)
(b)
1:0.3
1:1
1:0.1
1:0.8
1:0
1:0.5
396 397 398 399 400 401 402 403 404
Binding Energy (eV)

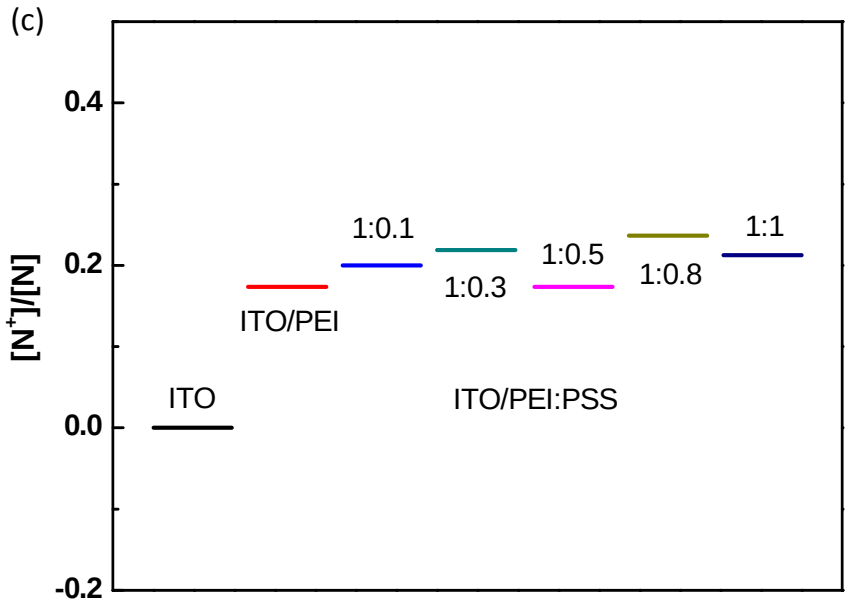

Figure 5.2 (a) Survey XPS spectra and (b) high-resolution XPS spectra of N 1s on the ITO/PEI and ITO/PEI:PSS with different ratios; (c) protonated amine/amine ratios of the ITO/PEI and ITO/PEI:PSS with different ratios.

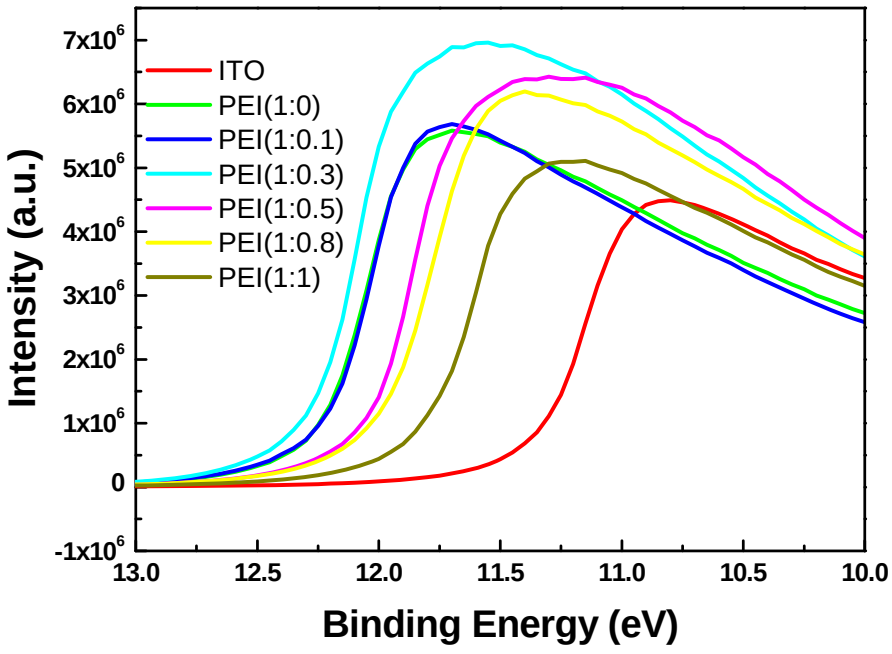

Figure 5.3 UPS spectra of the ITO cathods coated with PEI and PEI:PSS with different ratios.

5.2.2 Optical and morphological properties

The optical and morphological properties of each electrode have also been investigated. The transmittances of the ITO/PEI:PSS electrodes are almost identical to the bare ITO electrode (Fig. 5.4). The surface roughness of the ITO/PEI:PSS electrodes has little change as compared to the bare ITO, as characterized by AFM (Fig. 5.5). Therefore, the influences of optical and morphological to the cell performance can be excluded. The reduced ITO work-function is mainly caused by forming the interfacial dipoles at the ITO surface rather than changing the ITO optical and morphological properties.

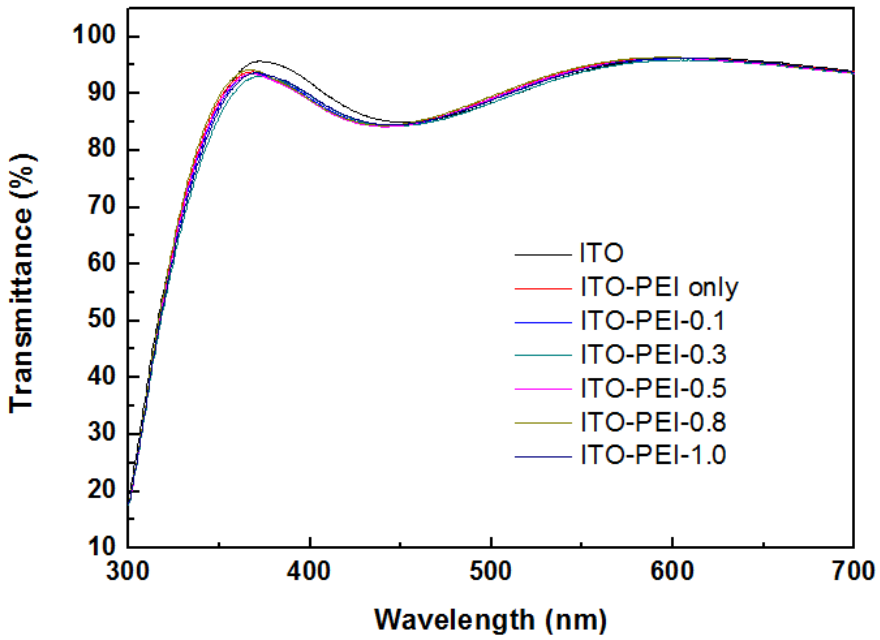

Figure 5.4 Tranmittance spectra of the ITO/PEI and ITO/PEI:PSS with different ratios.

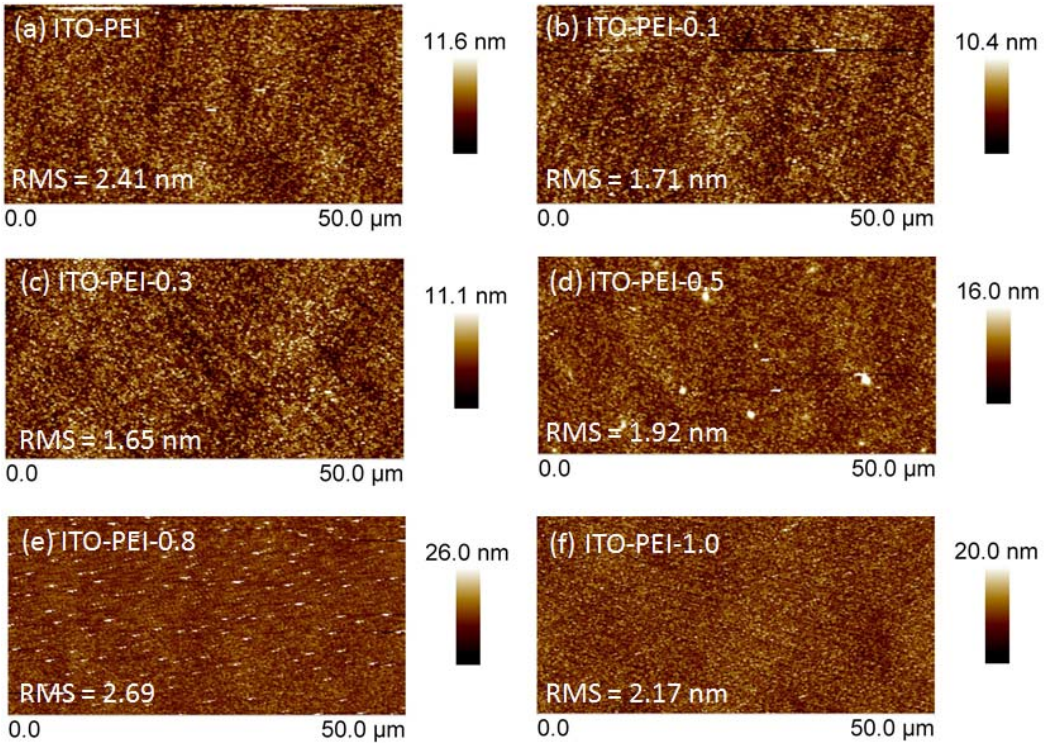

Figure 5.5 AFM images of the ITO/PEI surface and ITO/PEI:PSS surfaces with different ratios.

5.2.3 Device performance based on PEI:PSS interfacial layers

To explore the impacts of PEI:PSS as the interfacial layer on PSC device performance, a series of inverted PSCs with PEI:PSS coated ITO as the cathodes were fabricated. For comparison, the PSC devices using bare ITO, and ITO/ZnO as the cathodes were also fabricated at the same time. The cells' performance of open circuit voltage (V_{oc}), short circuit current (J_{sc}), fill factor (FF) and PCE, and their series (R_s) and shunt resistance (R_{sh}) are summarized in Table 5.1. It can be seen from Table 5.1 that the PEI-based cell shows a low J_{sc} (8.62 mA/cm^2) and PCE (3.01 %) which are lower than the ZnO-based cell (9.46 mA/cm^2, 3.12 %). However, with the incorporation of PSS into PEI, the J_{sc} increases significantly to 10.27 - 10.36 mA/cm^2 (when PSS/PEI $\geq$ 0.3). Even when PEI:PSS=1:0.1, the J_{sc} (9.99 mA/cm^2) is still

higher than the PEI- and ZnO-based cells. As a consequence, all the PEI:PSS based cells show much increased PCE (3.40 - 3.68 %) as compared to the PEI based cell (3.01 %), and the PCEs are also higher than the ZnO-based cell (3.12 %). The highest PCE of 3.68 % was obtained from the cell when PEI:PSS=1:0.3. It was thought that the strong ionic interaction between PEI and PSS helps the thin films forming 3D network. The conjugated PSS chain will help to improve the electron transport and extraction between cathode and active layer.

It is also noticed that the PEI:PSS-based cells have considerably decreased R_s (8.6 - 9.2 Ω/cm^2) and increased R_{sh} (720 - 1500 Ω/cm^2) as compared to the PEI-based cell (R_s =10.6 Ω/cm^2 , R_{sh} 546 Ω/cm^2). The increased J_{sc} and decreased R_s in the PEI:PSS based cells indicate that improved electron extraction is achieved through incorporation of PSS into the PEI in the interfacial layer.

Incident photon-to-current conversion efficiency (IPCE) spectra are shown in Fig. 5.6 (b). The IPCE at the wavelength of 550 nm is about 70 - 73 % for devices comprising of PEI:PSS interfacial layers, with the maximum IPCE (73 %) obtained for PEI:PSS=1:1. While the PEI-only device has an IPCE value of only 59 % at the wavelength of 550 nm.

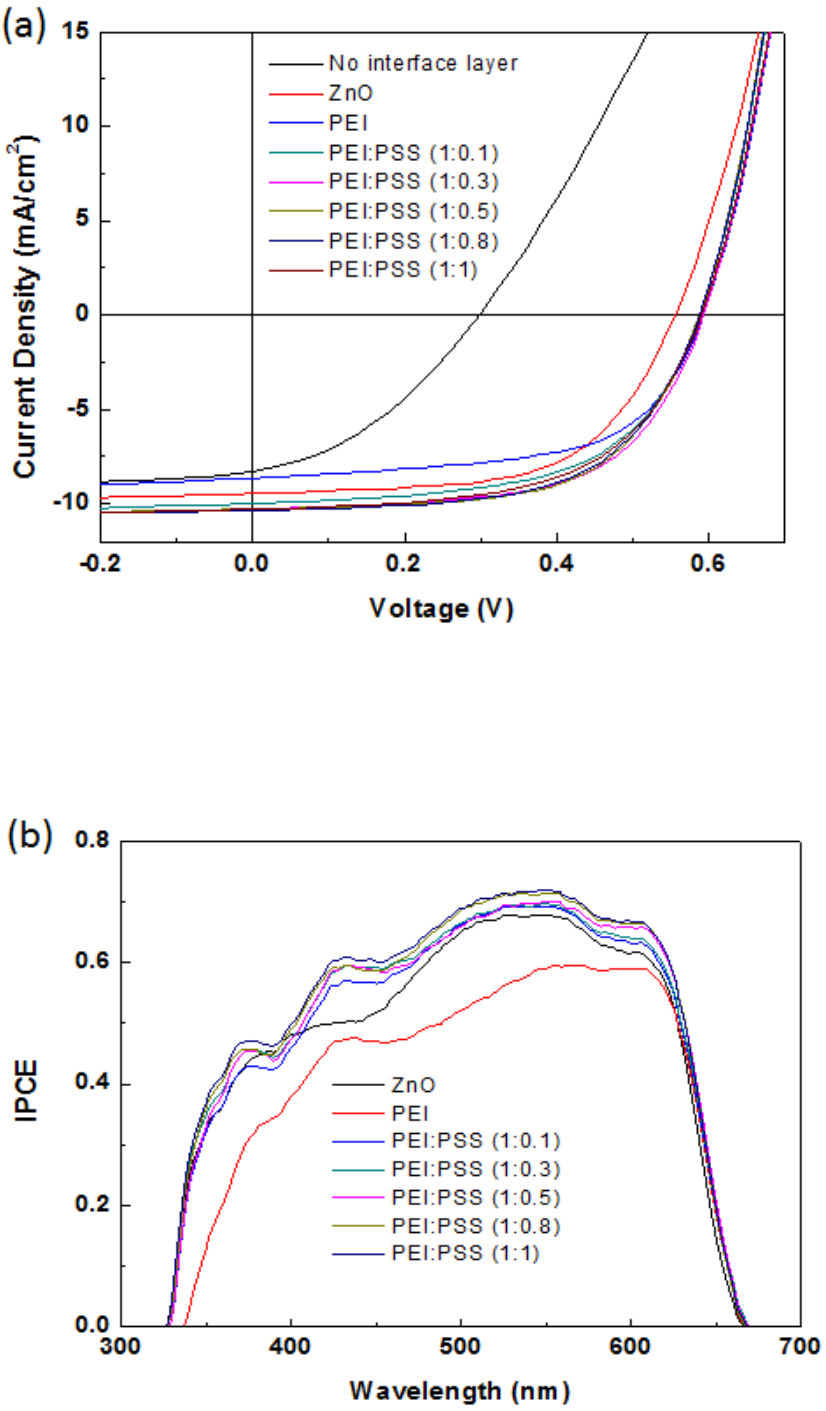

Figure 5.6 (a) *J* – *V* characterisctics of inverted P3HT:$PC_{61}BM$ solar cells incorporating no interfaical layer, ZnO layer and PEI:PSS films with different ratios; (b) IPCE spectra of inverted P3HT:$PC_{61}BM$ solar cells.

Table 5.1 Characteristics of PEI and PEI:PSS solutions with different ratios and the device photovoltaic performance parameters of inverted P3HT:$PC_{61}BM$ solar cells without interfacial layer, and incorporating with ZnO, PEI and PEI:PSS films with different ratios as the electron transport layer. ΔWF indicates the decreased work function value of ITO surface after coating with PEI:PSS with different ratios.

condition	ΔWF (eV)	pH	J_{sc} (mA/cm^2)	V_{oc} (V)	FF	η (%)	R_s (Ω/cm^2)	R_{sh} (Ω/cm^2)
No interface layer	0	N.A.	8.29	0.30	0.37	0.92	25	73
ZnO	N.A.	N.A.	9.46	0.56	0.59	3.12	9.7	900
PEI	0.86	10.26	8.62	0.592	0.59	3.01	10.6	546
PEI:PSS (1:0.1)	0.85	10.46	9.99	0.588	0.58	3.40	8.9	818
PEI:PSS (1:0.3)	0.89	10.74	10.30	0.595	0.60	3.68	8.6	720
PEI:PSS (1:0.5)	0.67	10.94	10.27	0.592	0.60	3.64	8.7	1058
PEI:PSS (1:0.8)	0.65	11.10	10.36	0.587	0.59	3.59	8.7	1500
PEI:PSS (1:1)	0.44	10.99	10.28	0.590	0.58	3.52	9.2	1059

5.3 Performance of devices based on TiO_x/PEI:PSS bilayer

In order to further investigate the versatility of this polyelectrolyte complex, we incorporated PEI:PSS onto metal oxide surface to enhance the efficiency of the cell by lowering the work-function of metal oxide and reduce trap-assisted recombination. As we know, the metal oxides based cathode buffer layers have many defect sites which usually act as recombination centers. When combining with other organic layer, the oxide surface was passivated to reduce the recombination.

The $J - V$ characteristics of inverted solar cells with TiO_x interlayer and TiO_x/PEI:PSS interlayer under AM. 1.5G irradiation at 100 mWcm^{-2} are shown in Fig. 5.7. The corresponding electrical parameters are summarized in Table 5.2. The device with only TiO_x interlayer has to undergo a light soaking to make the TiO_x layer well-functioning. It can be seen from Fig. 5.7 that the the $J - V$ curve of TiO_x-based cell

before light soaking has a kink, and the kink is removed after light soaking for 10 min, with PCE of 2.9 % obtained (J_{sc}=9.97 mA/cm^2, V_{oc}=0.55 V, and FF=0.53). This PCE is still lower compared to PEI:PSS-based devices (Table 5.1). However, the TiO_x/PEI:PSS-based cell, with the combination of TiO_x and PEI:PSS layers, not only eliminates the S shape in the $J - V$ curve (no light soaking needed), but also enhances the PCE to 3.9 % which is higher than the TiO_x-based cell (2.9 %) and PEI:PSS based cell (3.68 %). The PCE increase is from the increased V_{oc} and FF. Comparing the TiO_x/PEI:PSS-based cell to TiO_x-based cell, V_{oc} increases from 0.55 to 0.60 V, FF increased from 0.53 to 0.66, while the J_{sc} decreases from 9.97 to 9.89 mA/cm^2. R_s decreases from 13.1 Ω/cm^2 to 7.8 Ω/cm^2 and R_{sh} increases from 1059 Ω/cm^2 to 2223 Ω/cm^2. The increase of V_{oc} could be explained by work-function decrease by the PEI:PSS treatment, which could increase the work-function difference between cathode and anode. The decreased R_s, increased R_{sh} and enhanced FF could be explained by the surface passivation of TiO_x surface with PEI:PSS and reduced trap-assisted recombination.

Table 5.2 Device photovoltaic performance parameters of inverted P3HT:$PC_{61}BM$ solar cells incorporating TiO_x and TiO_x/PEI:PSS films as the electron transport layer.

condition	J_{sc} (mA/cm^2)	V_{oc} (V)	FF	η (%)	R_s (Ω/cm^2)	R_{sh} (Ω/cm^2)
TiO_x before light soaking	9.45	0.56	0.29	1.53	87.3	121.5
TiO_x after 5 min light soaking	9.97	0.55	0.53	2.90	13.1	1059
TiO_x/PEI:PSS (1:0.3)	9.89	0.60	0.66	3.91	7.8	2223

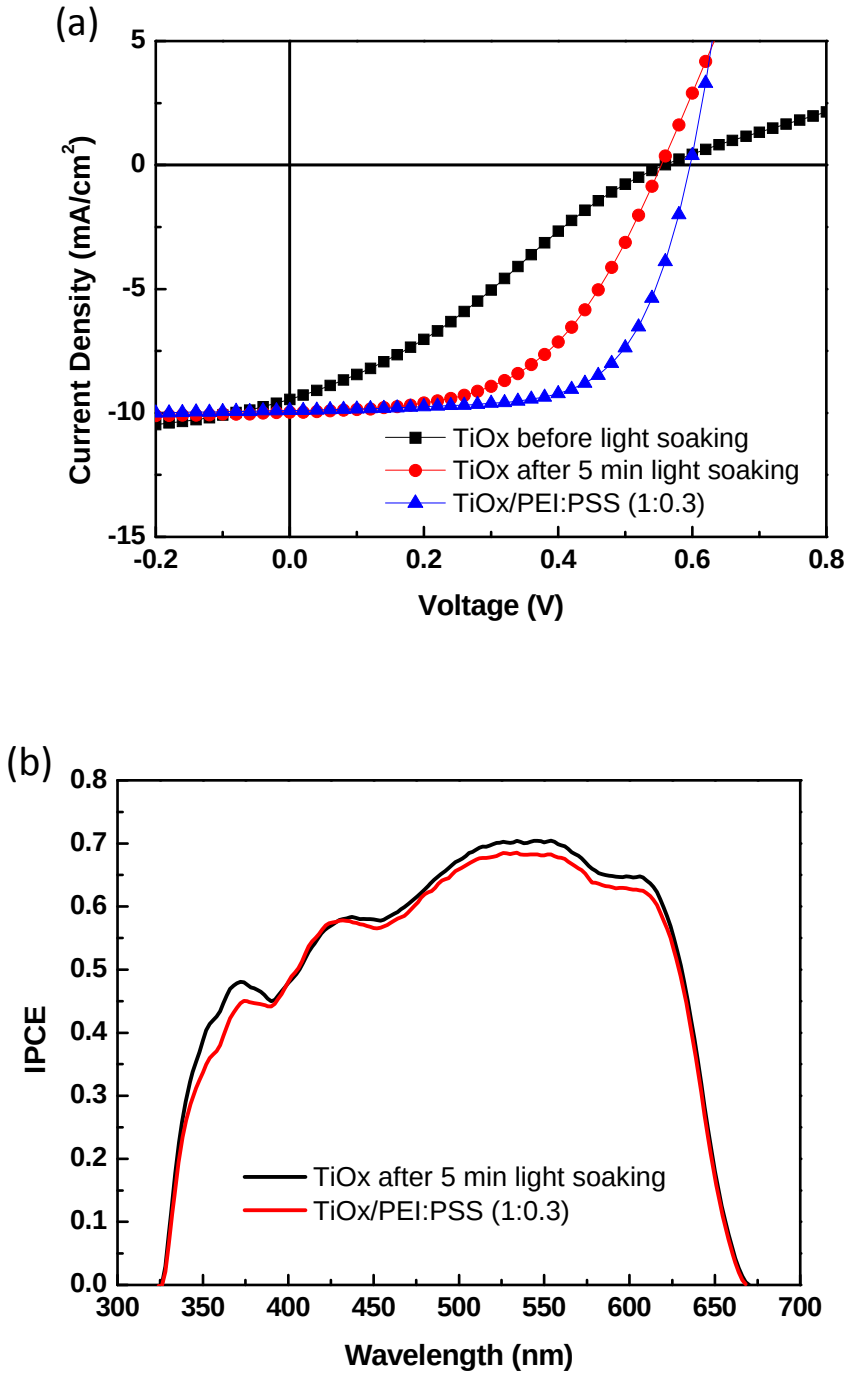

Figure 5.7 (a) *J – V* characterisctics of inverted P3HT:$PC_{61}BM$ solar cells with TiO_x interface layer before and after light soaking and with TiO_x/PEI:PSS interface layer; (b) IPCE spectra of inverted P3HT:$PC_{61}BM$ solar cells.

5.4 Device Stability

The stability of P3HT:$PC_{61}BM$ solar cells using PEI:PSS interfacial layers has also been investigated. The normalized PCEs as a function of storage time of the cells (unencapsulated) in a nitrogen filled glovebox are shown in Fig. 5.8. The PCE of ZnO-based cell has the faster degradation, with only 62 % remaining after 180 days. The PCEs of PEI-, and PEI:PSS-based cells have similarly the slowest degrading trend indicating much improved stability. The PCEs remains at approximately 94% of the origin values after 180 days for the PEI:PSS(1:0.3)-based cell. For the cells based on TiO_x and TiO_x/PEI:PSS(1:0.3), the PCEs remains at approximately 93% and 90%, respectively, both exhibit better stability than ZnO-based cell. This result shows that unencapsulated inverted solar cells based on the PEI:PSS films exhibit much better stability than ZnO films, indicating a better stability of the ITO/PEI/interfaces.

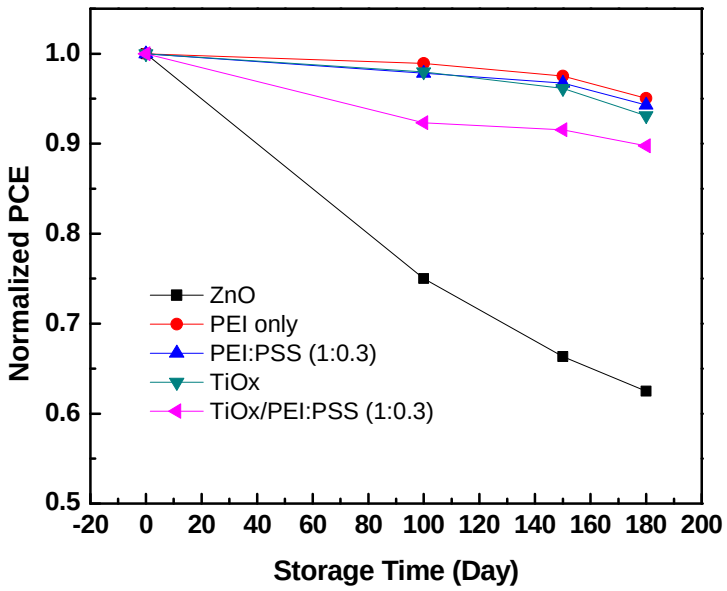

Figure 5.8 Stability of inverted P3HT:$PC_{61}BM$ solar cells with ZnO, PEI, PEI:PSS (with different ratios),TiO_x after light soaking and with TiO_x/PEI:PSS interface layers.

5.5 Performance of devices based on PCDTBT:$PC_{71}BM$

The TiO_x/PEI:PSS system was also applied to PCDTBT/$PC_{71}BM$-based inverted PSCs to test its feasibility in more general material systems. Fig. 5.9 (a) shows J – V characteristics of inverted solar cell based on PCDTBT/$PC_{71}BM$ incorporating with ZnO, TiO_x, PEI, PEI:PSS(1:0.3), and TiO_x/PEI:PSS(1:0.3) as the interfacial layer, respectively. The device parameters are summarized in Table 5.3. A PCE of 5.02 % for the device with PEI:PSS(1:0.3) on ITO was obtained which is higher than the PCEs of cells based on interlayers of ZnO, TiO_x and PEI, respectively. The PCE enhancement is mainly due to the increase in J_{sc}. By using TiO_x/PEI:PSS(1:0.3) interlayer, the PCE is further increased to 5.34 % due to the further enhancement of V_{oc} and FF.

Table 5.3 Device photovoltaic performance parameters of inverted PCDTBT:$PC_{71}BM$ solar cells incorporating ZnO, TiO_x, PEI, PEI:PSS(1:0.3) and TiO_x/PEI:PSS(1:0.3) films as the electron transport layer.

condition	J_{sc} (mA/cm^2)	V_{oc} (V)	FF	η (%)	R_s (Ω/cm^2)	R_{sh} (Ω/cm^2)
ZnO	9.22	0.86	0.60	4.75	9.7	720
TiO_x	9.62	0.87	0.58	4.85	19.1	900
PEI	8.83	0.83	0.53	3.88	13.1	562
PEI:PSS (1:0.3)	10.19	0.88	0.56	5.02	9.3	640
TiO_x/PEI:PSS (1:0.3)	9.73	0.90	0.61	5.34	8.1	973

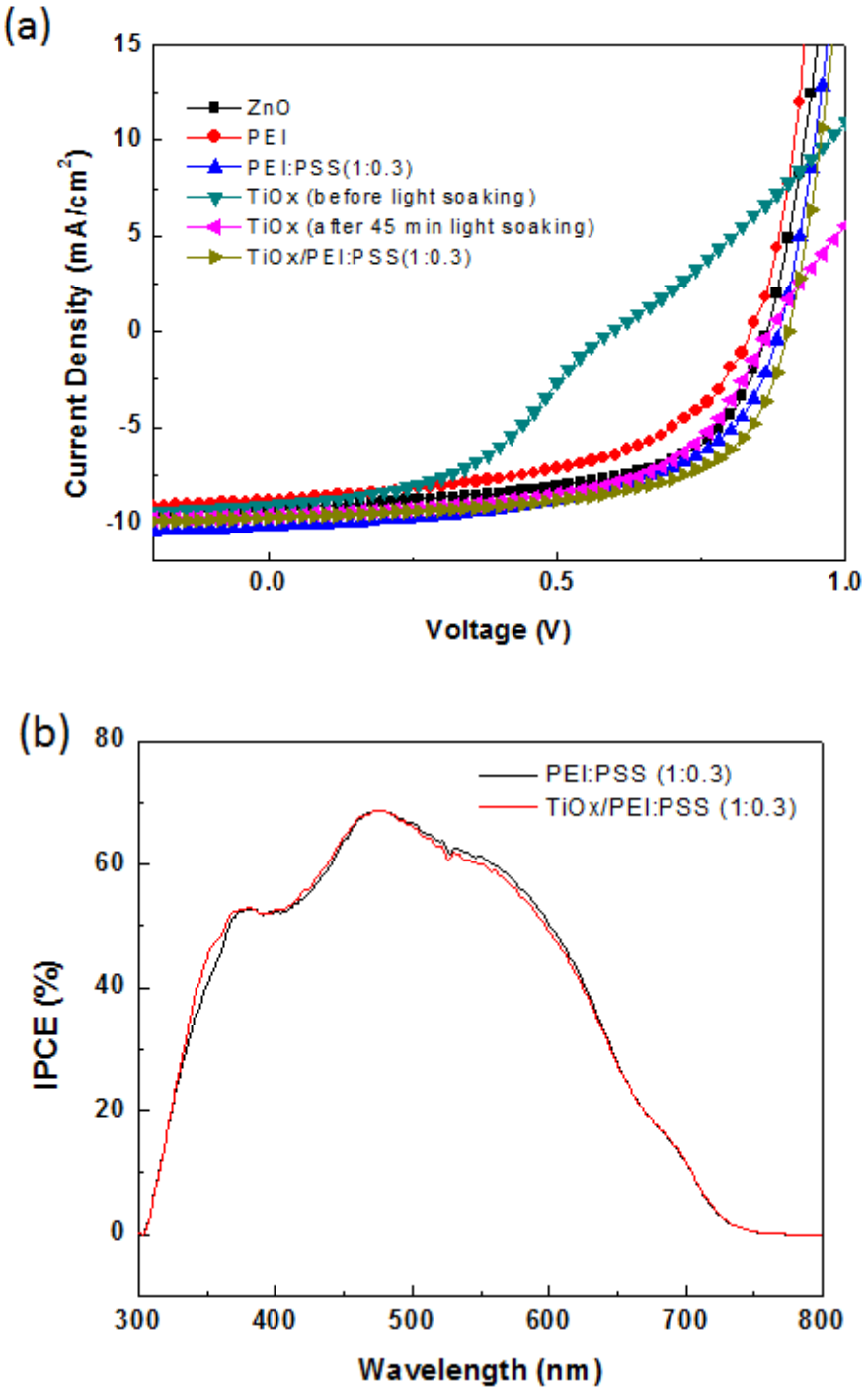

Figure 5.9 (a) *J* – *V* characterisctics of inverted PCDTBT:$PC_{71}BM$ solar cells with ZnO, PEI, PEI:PSS(1;0.3) interface layers, TiO_x interface layer before and after light soaking and with TiO_x/PEI:PSS (1:0.3) interface layer; (b) IPCE spectra of inverted PCDTBT:$PC_{71}BM$ solar cells with PEI:PSS(1:0.3) and TiO_x/PEI:PSS (1:0.3) interface layers.

5.6 Summary

In this chapter, high-efficiency inverted organic solar cells incorporating PEI:PSS films with different ratios as the cathode interfacial layer have been successfully demonstrated. Highest PCE of 3.68 % for P3HT:$PC_{61}BM$ devices was obtained at PEI:PSS ratio of 1:0.3. When the TiO_x layer modified by PEI:PSS(1:0.3), a high PCE of 3.9 % was obtained for P3HT:$PC_{61}BM$ device. In addition, PCEs of 5.02 % and 5.34 % were also obtained from the PCDTBT:$PC_{71}BM$ cells by incorporating into the PEI:PSS(1:0.3) and TiO_x/PEI:PSS(1:0.3) layers, respectively. The XPS and UPS analysis indicate that the work-function of ITO has a significant decrease after coating with PEI:PSS films. The reduced work-function results from the electrostatic interfacial dipoles formed by the protonated amines. Compared with the cells based on metal oxide and PEI-only interfacial layers, the cells based on PEI:PSS layers can obtain higher J_{sc} and V_{oc}, thus higher PCE. Meanwhile, the cells based on PEI:PSS interfacial layers have better air stability compared with the cells based on ZnO layers. The reduced work-function also eliminates the electron barrier caused by TiO_x layer which avoids the post-UV treatment and thus reduces the photo-induced degradation.

References

[5.1] S. K. Hau, H.-L.Yip, N. S. Baek, J. Zou, K. O'Malley and A. K.-Y.Jen, Applied Physics Letters 92, 253301 (2008).

[5.2] L. M. Chen, Z. Hong, G. Li, and Y. Yang, Advanced Materials 21, 1434 – 1449 (2009).

[5.3] Z. Xu, L. M. Chen, G.W. Yang, C.H. Huang, J. Hou, Y. Wu, G. Li, C. S. Hsu and Y. Yang, Advanced Functional Materials 19, 1227 – 1234 (2009).

[5.4] Z. Liang, Q. Zhang, O. Wiranwetchayan, J. Xi, Z. Yang, K. Park, C. Li and G. Cao, Advanced Functional Materials 22, 2194 – 2201 (2012).

[5.5] Y. Sun, J. H. Seo, C. J. Takacs, J. Seifter and A. J. Heeger, Advanced Materials 23, 1679 – 1683 (2011).

[5.6] Z. Lin, C. Jiang, C. Zhu and J. Zhang, ACS Applied Materirals and Interfaces 5, 713 – 718 (2013).

[5.7] H. Sun, J. Weickert, H. C. Hesse and L. Schmidt-Mende, Solar Energy Materials and Solar Cells 95, 3450 – 3454 (2011).

[5.8] Y. Zhou, H. Cheun, W. J. Potscavage, Jr, C. Fuentes-Hernandez, S. –J. Kim and B. Kippelen, Journal of Materials Chemistry 20, 6189 – 6194 (2010).

[5.9] Z. He, C. Zhong, S. Su, M. Xu, H. Wu and Y. Cao, Nature Photonics 6, 591 – 595 (2012).

[5.10] F. L. Zhang, F. Sedar and O. Inganäs, Advanced Materials 19, 1835 - 1838 (2007).

[5.11] H. Kang, S. Hong, J. Lee and K. Lee, Advanced Materials 24, 3005 – 3009 (2012).

[5.12] J. Liu, S. Shao, B. Meng, G. Fang, Z. Xie, Applied Physics Letters 100, 213906 (2012).

[5.13] A. Gadisa, Y. Liu, E. T. Samulski and R. Lopez, Applied Physics Letters 100, 253903 (2012).

[5.14] Y.-M. Chang, W.-F. Sua and L. Wang, Macromolecular Rapid Communications 29, 1303 – 1308 (2008).

[5.15] H. Choi, H. Cho, S. Song, H. Suh, S. Park and J. Y. Kim, Physical Chemistry Chemical Physics 12, 15309 – 15314 (2010).

[5.16] H. Choi, J. S. Park, E. Jeong, G.-H. Kim, B. R. Lee, S. O. Kim, M. H. Song, H. Y. Woo and J. Y. Kim, Advanced Materials 23, 2759 – 2763 (2011).

[5.17] A. Manor, E. A. Katz, T. Tromholt and F. C. Krebs, Advanced Energy Materials 1, 836 – 843 (2011).

[5.18] C. He, C. Zhong, H. Wu, R. Yang, W. Yang, F. Huang, G. Bazan and Y. Cao, Journal of Materials Chemistry 20, 2617 – 2622 (2010).

[5.19] J. H. Seo and T.-Q. Nguyen, Journal of the American Chemistry Society 130, 10042 – 10043 (2008).

[5.20] F. Yamauchi, K. Kato, H. Iwata, Langmuir 21, 8360 – 8367 (2005).

[5.21] C. Peng, Y. Thio and R. Gerhardt, Journal of Physical Chemistry C 14, 9685 – 9692 (2010).

[5.22] R. Schlapak, D. Armitage, N. Saucedo-Zeni, G. Latini, H. J. Gruber, P. Mesquida, Y. Samotskaya, M. Hohage, F. Cacialli and S. Howorka, Langmuir 23, 8916 – 8924 (2007).

[5.23] Y. Chen, E. T. Kang, K. G. Neoh, S. L. Lim, Z. H. Ma and K. L. Tan, Colloid and Polymer Science 279, 73 – 76 (2001).

[5.24] E. Metwalli, D. Haines, O. Becker, S. Conzone and C. G. Pantano, Journal of Colloid and Interface Science 298, 825 – 831 (2006).

Chapter 6

Conclusions and outlook

6.1 Summary of results

In this thesis, three types of cathode interfacial layers, ALD-grown, solution processed metal oxides (ZnO and TiO_x) and polyelectrolyte (PEI:PSS), have been studied for inverted OSCs.

ALD-grown ZnO and TiO_x films are dense, stable and robust with the capability of conformal coating on nanostructural surfaces, showing promising interfacial layers for OSCs. In Chapter 3, the low temperature ALD deposited metal-oxide thin films as the electron selective interlayer were conformally coated on the well-ordered periodic nano-groove structures to form the periodically nanostructured ITO-cathode/active-layer interfaces. By using ALD coating, it was found that the ITO patterns were maintained upon adding the metal oxide layer, thus avoiding the "flattening effect" which usually happens when spin coating PEDOT on the ITO patterns. It was also found that the thickness of the interfacial layer between the ITO surface and active layer was even and precisely controlled, thus eliminating the influence of the thickness variation of the interfacial layer. As a result, the device performance especially the photocurrent has been significantly increased by using the patterned ITO electrodes combined with ALD deposited metal oxide interlayer for the cells. Compared to the planar ITO cathode, the nano-patterned ITO cathode with only 30-nm-height nano-grooves led to a considerable improvement in short-circuit current

which increased by 10.8% (from 10.21 to 11.31 mA/cm^2) for P3HT:PCBM based OSCs with ZnO interlayer, and 23.11% (from 9.52 to 11.72 mA/cm^2) for OSCs with TiO_2 interlayer. The performance improvement is believed due to the enhanced charge collections and light absorption arising from the light trapping and also morphology improvement in the active layer.

In Chapter 4, the solution-processed metal oxides (ZnO and TiO_x) as cathode interfacial layer were developed, since the long-time consumption and expensive ALD deposition process is not desirable for the cost-effective fabrication process for OSCs. Firstly, effects of different post-treatments (thermal, humidity, and vacuum) of aqueous solution processed ZnO buffer layer were investigated on the device performance of inverted OSCs in terms of surface structure and properties. It was found that the thermal and vacuum post-treatments not only reduce the film surface defect sites but also increase the film crystallinity compared to the reference film. Based on P3HT:PC_{61}BM system, the devices with the ZnO buffer layer underwent thermal and vacuum post-treatments were found to exhibit the higher average PCE 3.58% and 3.51%, and the higher J_{sc}, 10.29 mA/cm^2 and 9.92 mA/cm^2, respectively. Secondly, the device photo-stability of devices based on ZnO, TiO_x interlayers, and ZnO/TiO_x, TiO_x/ZnO bilayers has also been studied, since photo-induced degradation is a big obstacle for the commercialization of OSCs. Due to the shunts generation and degeneration in ZnO layer, a significant degradation of V_{oc} and FF has been observed by periodic measurements of the device $J - V$ curves with 20 min illumination. Due to the high work-function of ITO/TiO_x layer, a UV-induced band binding occurs in TiO_x layer surface to reduce this schottky barrier, which causes a harmful photo-oxidation in the organic active layers. It was found that devices based on TiO_x/ZnO bilayer

obtained better device performance, and devices based on ZnO/TiO_x bilayer contained better photo-stability.

In Chapter 5, polyelectrolyte complex, PEI:PSS, as the cathode interfacial layer was used for highly efficient inverted OSCs. It was found that the PEI:PSS cathode interfacial layer can induce an ohmic contact with the fullerene active layer and increase the built-in fields through significant reduction of the work-function of ITO. Using the blend of P3HT and $PC_{61}BM$ as the active layer, OSC devices incorporating PEI:PSS as the cathode interfacial layer show much increased PCE than the devices with ZnO or PEI-only interfacial layer. The combination of PEI:PSS with TiO_x bilayer polyelectrolyte exhibited excellent performance by reducing the energy barrier for electron injection and transport and reducing the trap-assisted recombination. The S-shape in the $J - V$ curves of devices based on TiO_x layers has been eliminated due to the reduced electron injection barrier. Meanwhile, it was found that device air stability based on PEI:PSS interfacial layer was better than devices based on ZnO layer. From the solution processability, air stability, and device performance, the polyelectrolyte, PEI:PSS, should be the best choice for interlayer in inverted solar cells.

6.2 Recommendations for future work

Three types of cathode interfacial layers have been studied and their properties and effects on device performance have been clearly demonstrated. However, there are still some issues need further study. Based on my understanding acquired from the research projects, the following new ideas are proposed.

(1) To investigate effects of different periods and depths of patterned ITO nanostructure on OSC device performance. The period and depth of patterned ITO nanostructure studied in this work is 500 nm and 30 nm (maximum depth), respectively. It was found that this 500 nm period determined the light absorption enhancement range around 500 nm in solar spectra. As a result, we can try different pattern periods to optimize the light absorption to further enhance the J_{sc}. Meanwhile, due to the wet chemical etching technique we used in this work, the maximum depth can be achieved is only 30 nm and the pattern depth is difficult to be controlled. In the future work, we could use RIE dry etching to obtain larger depth and the deeper pattern can be better controlled, so the device performance can be further optimized.

(2) To further increase the conducting property of PEI:PSS film to replace ITO film. Many new transport and conducting materials have been proposed and studied to replace ITO, such as PEDOT:PSS, graphene and metal meshes, since ITO is expensive and brittle. We have found that adding PPS into PEI solution could change the solution conductivity and thus the film conductivity. In the next step, we could further increase the film conductivity to replace ITO film to fabricate ITO-free OSC device. This fabrication method will more fit the roll-to-roll and cost-effective fabrication process.

(3) Since roll-to-roll and cost-effective fabrication process is always what we wanted, the all solution-processed OSC device is desired. In this work, the hole selective layer (MoO_3) and anode (Ag) were all deposited by vacuum thermal evaporation. However, this deposition processed is not desirable for the roll-to-roll fabrication process. In the future work, firstly, we would use PEDOT:PSS as the hole selective layer instead of MoO_3, so the spray coating or die slot coating method can be applied. Secondly, we can utilize screen printing technique to fabricate the Ag

anode. As a result, all solution processed OSC device can be obtained and the flexible substrate can be used.